Purdue University
Purdue e-Pubs

Open Access Dissertations | Theses and Dissertations

Fall 2013

A Novel Fluid Structure Interaction and Thermal Model to Predict the Cylinder Block / Valve Plate Interface Performance in Swash Plate Type Axial Piston Machines

Marco Zecchi
Purdue University

Follow this and additional works at: https://docs.lib.purdue.edu/open_access_dissertations

Part of the Mechanical Engineering Commons

Recommended Citation
Zecchi, Marco, "A Novel Fluid Structure Interaction and Thermal Model to Predict the Cylinder Block / Valve Plate Interface Performance in Swash Plate Type Axial Piston Machines" (2013). *Open Access Dissertations*. 9.
https://docs.lib.purdue.edu/open_access_dissertations/9

This document has been made available through Purdue e-Pubs, a service of the Purdue University Libraries. Please contact epubs@purdue.edu for additional information.

Graduate School ETD Form 9
(Revised 12/07)

PURDUE UNIVERSITY
GRADUATE SCHOOL
Thesis/Dissertation Acceptance

This is to certify that the thesis/dissertation prepared

By Marco Zecchi

Entitled

A Novel Fluid Structure Interaction and Thermal Model to Predict The Cylinder Block / Valve Plate Interface Performance In Swash Plate Type Axial Piston Machines

For the degree of Doctor of Philosophy

Is approved by the final examining committee:

Monika Ivantysynova
Chair

John H. Lumkes Jr.

Farshid Sadeghi

Andrea Vacca

To the best of my knowledge and as understood by the student in the *Research Integrity and Copyright Disclaimer (Graduate School Form 20)*, this thesis/dissertation adheres to the provisions of Purdue University's "Policy on Integrity in Research" and the use of copyrighted material.

Approved by Major Professor(s): Monika Ivantysynova

Approved by: Bernard Engel 11/27/2013
Head of the Graduate Program Date

A NOVEL FLUID STRUCTURE INTERACTION AND THERMAL MODEL TO PREDICT THE CYLINDER BLOCK / VALVE PLATE INTERFACE PERFORMANCE IN SWASH PLATE TYPE AXIAL PISTON MACHINES

A Dissertation

Submitted to the Faculty

of

Purdue University

by

Marco Zecchi

In Partial Fulfillment of the

Requirements for the Degree

of

Doctor of Philosophy

December 2013

Purdue University

West Lafayette, Indiana

TABLE OF CONTENTS

Page

LIST OF TABLES v

LIST OF FIGURES vi

SYMBOLS xii

ABBREVIATIONS xv

ABSTRACT xvi

1 Introduction 1

1.1 Background 1

1.2 State of the art 4

1.3 Aims 10

1.4 Original contributions of this work 10

2 The cylinder block / valve plate interface 14

2.1 Axial piston machine kinematics 17

2.2 Dynamic load condition of the cylinder block 18

2.2.1 Loads directly applied to the cylinder block 19

2.2.2 Loads associated with the piston/slipper assembly 22

2.2.3 The reaction in the spline joint 26

2.2.4 Loads from the pressure field in the fluid film 29

2.3 Principle of operation and associated physical phenomena 31

2.4 Fluid film geometry 35

2.5 The non-isothermal fluid flow in the clearance 39

2.5.1 The Reynolds equation for the cylinder block valve plate interface 40

2.6 The energy equation 41

2.7 Power losses 42

Page

3 The fluid structure interaction and thermal model 44
3.1 Model overview 44
3.2 Model's workflow 46
4 Solution of the non-isothermal fluid flow 51
4.1 Grid features and generation 51
4.1.1 Discretization of the Reynolds equation 55
4.1.2 Boundary conditions 59
4.2 Solution of the Reynolds equation and the fluid structure interaction problem 61
4.2.1 The Preconditioned bi-Conjugate Gradient stabilized method for the solution of sparse linear systems 64
4.2.2 Treatment of sub-ambient pressure regions 68
4.3 Discretization of the Energy equation 69
4.3.1 Boundary conditions 72
4.4 Solution of the energy equation 75
5 The heat transfer problem 76
5.1 Boundary conditions 77
5.1.1 Calculation of the heat fluxes towards the solid parts 78
5.1.2 Estimation of the convection coefficients 78
5.2 Typical settings of the thermal boundary conditions 84
5.3 Finite element discretization of the heat transfer equation 86
5.4 The linear tetrahedron 89
5.4.1 The temperature-gradient interpolation matrix 91
5.4.2 Surface integrals 93
5.5 Finite element formulation of the thermal problem with the tetrahedron element 94
5.6 Solution scheme 95
6 Calculation of the elastic deformation of the solid parts 97
6.1 Linear elastic deformation analysis and solution 97

Page

6.2 Finite element formulation of the linear elastic problem with the tetrahedron element 101

6.3 Boundary conditions 103

6.3.1 Deformation due to temperature loads 103

6.3.2 Deformation due to pressure loads 104

6.4 Influence method for pressure deformation 106

6.5 Interpolation between fluid and structure grids 109

6.6 Correction of the film thickness geometry with the elastic deformations 110

6.7 Additional consideration about the calculation of the elastic deformation of the valve plate and end case assembly 114

6.7.1 Solid contact problem between valve plate and end case . . . 116

6.7.2 Linear model approach for the pressure and thermal deformation analysis of the valve plate and end case assembly 119

7 Measurements of the surface temperature of the valve plate during operation 122

7.1 Surface temperature measurements as indicator of fluid film thickness 123

7.2 Description of the test stand and measurement procedure 125

8 Simulation model predictions and comparison with measurements 131

8.1 Comparison between model prediction and measurements 131

8.2 Simulation results for a selected operating condition 140

8.3 A study of the impact of micro surface shaping on the performance of the cylinder block / valve plate interface 144

9 Conclusions and outlook 150

A Derivation of the specific for of the Reynolds equation used in this work . 153

B Determination of the mathematical model of the hydraulic fluid used for the measurements and simulations presented in this thesis 158

B.1 Development of the density equation 158

B.2 Development of the isothermal bulk modulus equation 161

B.3 Development of the viscosity equation 162

LIST OF REFERENCES 166

VITA 171

LIST OF TABLES

Table Page

4.1 Computation time in [ms] required by the solvers of Fig. 4.9 on different grid sizes. The processor was an Intel i7 870@2.93 GHz. 68

6.1 Mechanical and thermodynamic properties of the materials defined in the model. *The properties of bronze were changed to maximize the fidelity of the linear model. 120

7.1 Summary and specification of all the components in Fig. 7.3. 130

8.1 Average and maximum percentage error between measured and predicted temperature as function of operating pressure at 2000 rpm. The maximum and average error were calculated for the 21 working thermocouples in the valve plate. 132

8.2 Average and maximum percentage error between measured and predicted temperature as function of operating pressure at 2800 rpm. The maximum and average error were calculated for the 21 working thermocouples in the valve plate. 132

B.1 Measured variation of density as a function of pressure for three different temperatures 159

B.2 Constants in the Eq. B.1 that maximize the fit with the measured data. 161

B.3 Measured variation of dynamic viscosity as a function of pressure for five different temperatures 163

LIST OF FIGURES

Figure Page

1.1 Measured overall efficiency of variable displacement axial piston motors at 2000 rpm and 200 bar (from Baker and Ivantysynova (2009)) 2

1.2 Sectioned view of the rotating kit of a swash plate type axial piston machine 3

2.1 Typical geometrical features of the cylinder block valve plate interface. 14

2.2 Example of kidney opening with hydrostatic grooves. 15

2.3 Typical design of the spherical valve plate. 16

2.4 Axial piston machine kinematic. 17

2.5 Loads directly applied to the cylinder block. 19

2.6 Instantaneous displacement chamber pressure for a 130 cc unit, at 3000 rpm, maximum displacement angle and 400 bar differential pressrure. . 20

2.7 Calculation of force and moment associated with the pressurized fluid in the displacement chamber 21

2.8 Example of F_{Bz}, M_{Bx} and M_{By} over one shaft revolution. $\Delta p = 200\text{bar}, n = 2000\text{rpm}, \beta = 100\%$ 23

2.9 External loads acting on the piston/slipper assembly. 24

2.10 Representation of the loads transferred to the cylinder block by the piston / slipper assembly for a 130 cc unit, at 3000 rpm, 400 bar differential pressure and 50% displacement angle. 25

2.11 Representation of F_{SKy} for two different pistons on the high pressure region of the machine. The reaction of the shaft on the radial load is also represented as F_{SR}. 27

2.12 Representation of the additional moment introduced by the shaft reaction on the cylinder block as a function of the crowning point position with respect to the ideal location. Calculated for a 130 cc unit at 1000 rpm, 400 bar and maximum displacement angle. 28

2.13 Pressure load calculation with the spherical design. 30

2.14 Total external loads on the cylinder block, for a 130cc unit operating at 2000 rpm, under a differential pressure of 200 bar and 50% displacement. 32

Figure Page

2.15 Ideal situation of non-deformable solid parts. The clearance geometry is defined by the relative position of the cylinder block with respect to the valve plate. 36

2.16 Clearance geometry definition accounting for arbitrary shapes of the cylinder block and valve plate sealing surfaces. 38

3.1 Overview of the fluid structure interaction and thermal model of the cylinder block / valve plate interface. 45

3.2 Workflow of the simulation model for the cylinder block and valve plate interface 48

4.1 Structured grid used to solve for the fluid flow. 52

4.2 Grids generation for cylinder block and valve plate surfaces. The yellow elements represent fluid and the grey elements are part of openings, ports, or grooves. The blue boundary lines define the actual shape of the cylinder block and valve plate sealing surfaces. 54

4.3 (a) pressure field calculated through the solution of the Reynolds equation on a computation grid of 60×360 elements; (b) pressure field interpolated from (a) on the grid used for the calculation of the pressure loads on the cylinder block. 55

4.4 Detail of the control volume used to discretize the Reynolds equation in cylindrical coordinates. 56

4.5 Boundary conditions applied to solve the Reynolds equations at shaft angle $\varphi = 0$. 60

4.6 Control volume surrounded by part of the high pressure port, where the pressure is imposed at the value p_{HP}. 60

4.7 Convergence behavior for the solution of the fluid structure interaction problem. 63

4.8 Typical sparse pattern for the matrix $\mathbf{A}$ from the discretization of the Reynolds equation on the grid of Fig. 4.3. 64

4.9 Convergence behavior for different solution methods for a grid of $m \times n = 160 \times 1440$ elements (the non zero entries in $\mathbf{A}$ were 139924. The film thickness and the associated pressure field are also represented. 67

4.10 Three dimensional elements used to discretize the Energy equation. . . 70

4.11 Lubricating film (scaled 1000 times in z direction) and different surfaces where boundary conditions are required to solve the Energy equation. . 73

Figure Page

4.12 Example of inflow and outflow boundaries in the solution of the Energy equation. 74

5.1 Fluid domain used to estimate the convection coefficient. 80

5.2 Example of calculated convection coefficient and variation of the average value among the surface as a function of pump flow. 83

5.3 Example of calculated convection coefficient for 130 l/min pump flow and variation of average convection coefficient upon the surface as a function of the pump flow. 83

5.4 Thermal boundary condition applied to the cylinder block body. 84

5.5 Thermal boundary condition applied to the valve plate and end case assembly. 85

5.6 Tetrahedron element, local numbering and definition of the natural coordinate 90

6.1 Pressure loads on cylinder block, valve plate and end case bodies. . . . 106

6.2 Example of influence matrices (a) for one of the faces used to discretize the cylinder block's surface bounding the lubricating interface and (b) for one of the displacement chamber. 108

6.3 Interpolations required to transfer pressure and elastic deformation fields from fluid to structure and vice versa. 111

6.4 "Cells to cells" and "nodes to cells" interpolation schemes. 111

6.5 Example of temperature field in the cylinder block and valve; the solid parts are warped with the thermal deflections with a scale of 1000:1. The relative deformations of the two surfaces in contact with the lubricant are shown on the right. 113

6.6 Thermal deflection of the valve plate and end case assembly. 114

6.7 The contour represents a reasonable temperature field in the bi-metal valve plate and end case during operation. The two bodies are warped with the associated thermal deflection, with a scale of 1000:1. A gap of 50 μm is present when the valve plate is not loaded with any pressure. 115

6.8 Pressure loads on the valve plate and end case assembly considering the thermal deflection of the parts. 117

6.9 Representation of the mesh of the valve plate end case assembly warped with the thermal deflection. 118

Figure Page

6.10 Contour representing the displacement in z direction of the valve plate and end case assembly. The solution was found for a differential pressure of 200 bar. 119

6.11 Valve plate surface deformation, comparison between linear model and non-linear solid contact analysis for $\Delta p = 200$ bar. 120

7.1 Position of the thermocouples on the valve plate mounted on the 130cc unit used for the measurements (view from the bottom of the valve plate). 126

7.2 Picture of the valve plate and case that were used for the measurements. The position of the thermocuples is also indicated. 126

7.3 Schematic of the test stand developed to take steady state temperature measurements on a 130cc axial piston unit. 127

8.1 Comparison between measured and predicted surface temperature measurement of the valve plate @ 2000 rpm, 50 bar and 50% displacement. 134

8.2 Cross sections in the $y-z$ and $x-z$ plane, illustrating the predicted fluid film thickness between cylinder block and valve plate, @ 2000 rpm, 50 bar and 50%. The solid parts were warped with the elastic deformations due to pressure and temperature (the scaling factor is 1000:1 in z direction). 134

8.3 Comparison between measured and predicted surface temperature measurement of the valve plate @ 2000 rpm, 200 bar and 50% displacement. 135

8.4 Cross sections in the $y-z$ and $x-z$ plane, illustrating the predicted fluid film thickness between cylinder block and valve plate, @ 2000 rpm, 200 bar and 50%. The solid parts were warped with the elastic deformations due to pressure and temperature (the scaling factor is 1000:1 in z direction). 135

8.5 Comparison between measured and predicted surface temperature measurement of the valve plate @ 2000 rpm, 400 bar and 50% displacement. 136

8.6 Cross sections in the $y-z$ and $x-z$ plane, illustrating the predicted fluid film thickness between cylinder block and valve plate, @ 2000 rpm, 400 bar and 50%. The solid parts were warped with the elastic deformations due to pressure and temperature (the scaling factor is 1000:1 in z direction). 136

8.7 Comparison between measured and predicted surface temperature measurement of the valve plate @ 2800 rpm, 50 bar and 50% displacement. 137

8.8 Cross sections in the $y-z$ and $x-z$ plane, illustrating the predicted fluid film thickness between cylinder block and valve plate, @ 2800 rpm, 50 bar and 50%. The solid parts were warped with the elastic deformations due to pressure and temperature (the scaling factor is 1000:1 in z direction). 137

Figure Page

8.9 Comparison between measured and predicted surface temperature measurement of the valve plate @ 2800 rpm, 200 bar and 50% displacement. 138

8.10 Cross sections in the $y-z$ and $x-z$ plane, illustrating the predicted fluid film thickness between cylinder block and valve plate, @ 2800 rpm, 200 bar and 50%. The solid parts were warped with the elastic deformations due to pressure and temperature (the scaling factor is 1000:1 in z direction). 138

8.11 Comparison between measured and predicted surface temperature measurement of the valve plate @ 2800 rpm, 400 bar and 50% displacement. 139

8.12 Cross sections in the $y-z$ and $x-z$ plane, illustrating the predicted fluid film thickness between cylinder block and valve plate, @ 2800 rpm, 400 bar and 50%. The solid parts were warped with the elastic deformations due to pressure and temperature (the scaling factor is 1000:1 in z direction). 139

8.13 External loads on the cylinder block over one shaft revolution @ $n =$ 2000rpm, $\Delta p = 200$ bar and $\beta = 50\%$. 140

8.14 Cylinder block position and film thickness over one shaft revolution @ $n = 2000$rpm, $\Delta p = 200$ bar and $\beta = 50\%$. 141

8.15 Predicted fluid film thickness (scaled 1000:1 in z direction) and pressure field for six angular positions @ 2000 rpm, $\Delta p = 400$ bar and 50% displacement. The valve plate body is also represented and warped with scale 1000:1 in z direction with the combination of pressure and thermal loads. 142

8.16 Elastic deformations of cylinder block and valve plate surface warped with scale 1000:1 in z direction. 143

8.17 Predicted temperature field in the cylinder block and valve plate. The two bodies were warped with the associated thermal deflection in all the directions with a scale of 1000:1. 143

8.18 Predicted power loss over one shaft revolution. 145

8.19 Predicted power loss over one shaft revolution. 146

8.20 Friction, leakage and total power losses in the cylinder block / valve plate interface for standard and waved valve plate surface predicted by the present simulation model. Standard valve plate design and micro wave pattern with 15 peaks and 1μm amplitude are represented. 147

8.21 Pressure field and film thickness for the standard design @ 1000 rpm, 100 bar and 100% displacement. (The lubricating film is magnified 1000 times in z direction 148

Figure Page

8.22 Pressure field and film thickness for the 1μ amplitude waved valve plate @ 1000 rpm, 100 bar and 100% displacement. (The lubricating film is magnified 1000 times in z direction) 149

A.1 Sketch of a lubricating gap defined by two surfaces of arbitrary shape. The reference plane $z = 0$ used to derive the Reynolds equation is also represented. 155

B.1 (a) variation of density as a function of temperature at the reference pressure; (b) variation of density as a function of pressure at reference temperature. 159

B.2 (a) variation of density as a function of pressure at $T = 75°C$; (b) variation of density as a function of pressure at $T = 120°C$. 160

B.3 Variation of bulk modulus as a function of temperature for different constant pressures. 162

B.4 Variation of dynamic viscosity as a function of pressure at 25°C and 100°C. 164

B.5 Variation of bulk modulus as a function of temperature for different constant pressures. 164

SYMBOLS

t	time
φ	shaft angular position
ω	angular velocity
β	swash plate angle
R_b	pitch radius
R_B	outer radius cylinder block
R_s	spherical radius
s_K	piston position
v_K	piston velocity
a_K	piston acceleration
d_K	piston diameter
H_K	piston stroke
V_i	geometric displacement
ϕ_K	Circumferential position in the unwrapped piston reference system
p	pressure
T	temperature
ν	kinematic viscosity, Poisson's ratio
μ	dynamic viscosity
λ	thermal conductivity
c_p	heat capacity at constant pressure
Φ_d	viscous dissipation
ρ	fluid density
h	film thickness, convection coefficient

$\dot{h}$	squeeze motion
$\boldsymbol{V}$	fluid velocity
$\boldsymbol{F}$	force
$\boldsymbol{M}$	moment
$\boldsymbol{u}$	body displacement
Q	leakage flow
q	heat flux
k	turbulent kinetic energy
T_i	turbulence intensity
ϵ	dissipation rate of the turbulent kinetic energy, strain
$\boldsymbol{\nabla}$	gradient operator
$\boldsymbol{\nabla}\cdot$	divergence operator
P	element centroid
S	source
b	known term
a	algebraic equation coefficient
Γ	diffusion coefficient
$\mathbf{A}$	sparse matrices
κ	condition number
e	solution error
(ν)	inner loop iteration
(k)	outer loop iteration
W_i	weighting factor
$\mathbf{N}$	shape functions matrix
$\mathbf{C}$	constitutive matrix
$\mathbf{k}$	element stiffness matrix
$\mathbf{K}$	global stiffness matrix
$\mathbf{B}$	temperature-gradient or strain-displacement matrix
E	elastic modulus

σ	stress
Π	total potential energy
U	strain energy
V	applied load potential energy
L	natural coordinate
J	Jacobian
$\boldsymbol{q}$	convection and applied heat element thermal load
$\boldsymbol{Q}$	convection and applied heat total thermal load
$\boldsymbol{f}$	element nodal load
IM	influence matrix
m, n, q	fluid grid dimension, radial, circumferential and axial
α	generic angle, relaxation coefficient, coefficient of thermal expansion
$\boldsymbol{n}$	normal vector
$\boldsymbol{r}$	position vector, residual
$\delta\mathscr{A}$	area of a cell face
$\delta\mathscr{V}$	volume of a cell
$\delta r, \delta\vartheta, \delta z$	radial, circumferential and axial cell dimensions
$\mathscr{S}$	sealing surface
$\mathcal{S}$	generic surface
(x, y, z)	Cartesian reference system
(u, v, w)	velocity or displacement components
(r, ϑ, z)	Cylindrical reference system
$\boldsymbol{i}, \boldsymbol{j}, \boldsymbol{k}$	x, y and z versors
P_1, P_2, P_3	reference points for the cylinder block position

ABBREVIATIONS

DC	Displacement Chamber
LP	Low Pressure
HP	High Pressure
K	Piston
G	Slipper
T	Cylinder bore
B	Block
CB	Cylinder Block
VP	Valve Plate
R	Resultant
SR	Spline reaction
f	Fluid
ob	Outer bearing
sl	Sealing land
em	Electric motor
w, e, s, n, b, t	west, east, south, north, bottom, top
Δ	variation

ABSTRACT

Zecchi, Marco Ph.D., Purdue University, December 2013. A novel fluid structure interaction and thermal model to predict the cylinder block / valve plate interface performance in swash plate type axial piston machines . Major Professor: Ivantysynova, Monika.

The cylinder block / valve plate interface represents one of the most critical design element in the rotating kit of axial piston machines. The thin film of lubricant between cylinder block and valve plate has to fulfill simultaneously a bearing and a sealing function under dynamic load conditions; on the other hand, it represents an important source of power losses due to viscous friction and leakage flow.

An accurate prediction of the time changing characteristics of the interface, in terms of fluid film thickness, dynamic pressure field, load carrying ability and energy dissipation is necessary to generate more efficient and reliable designs. However, the complexity of the physical phenomena involved in the interface's operation made the trial end error practice the main design methodology in the last fifty years. The aim of this work is to deepen the understanding of the main physical phenomena affecting the cylinder block / valve plate interface performance. For this purpose, a unique fully coupled multi-body dynamics model has been proposed to capture the complex fluid-structure interaction phenomena affecting the non-isothermal fluid film conditions. The model is able of determining the fluid film thickness as a function of the interface's load condition, accounting for the squeeze film effect due to the cylinder block's micro-motion and the change in fluid film thickness due to the elastic deformations of the solid parts, caused by the fluid film pressure and by the thermal strains. In addition, the impact of micro-surface shaping introduced by design or resulting from wear process can be investigated and combined with the modification of the clearance due to the normal machine operation.

The model was validated by comparing the predicted surface temperature of the valve plate with measurements for two different machines, a 100 cc and a 130 cc units of commercial production. In the first case the measurements were available in literature, in the second case an specific test stands was developed as part of the experimental study of the present work. The model has also been applied to the study of the impact of micro surface shaping on the performance of the cylinder block / valve plate interface.

1. INTRODUCTION

1.1 Background

Hydrostatic pumps and motors are positive displacement machines which operate forcing fluid into or out a volume by changing in different ways their geometric configuration over one shaft revolution. There are many different types of positive displacement machines in the market, characterized by the different ways in which the volumetric displacement is achieved, with consequent advantages and disadvantages.

Axial piston machines are among the most widely used types, due to their high operating pressure, variable displacement operation, superior efficiency, compactness and long life. Current advanced developments in the fluid power systems technology, such as displacement controlled actuation and hydrostatic hybrid transmissions, use variable displacement axial piston units directly as control element. The units are therefore forced to operate over a much wider range of operating conditions compared to pressure compensated and load sensing pumps, in terms of speed, displacement and differential pressure. The new applications expect the axial piston unit to maintain a very high efficiency under extremely varying operating conditions, introducing a significant challenge for the designer. Figure 1.1 illustrates the measured overall efficiency of variable displacement axial piston motors at 2000 rpm and 200 bar. Two observations can be made: first, all the designs are characterized by a very high efficiency at maximum displacement; second, all the designs share a common trend, experiencing a reduction of efficiency at lower displacement angles. The total efficiency reduction is related to volumetric and mechanical energetic dissipations, which progressively outweighs the machine output power as the load decreases. The reduction of efficiency is sensibly lower with the bent axis design, especially for high bend angle. However, the bent axis units are expansive and the design required to

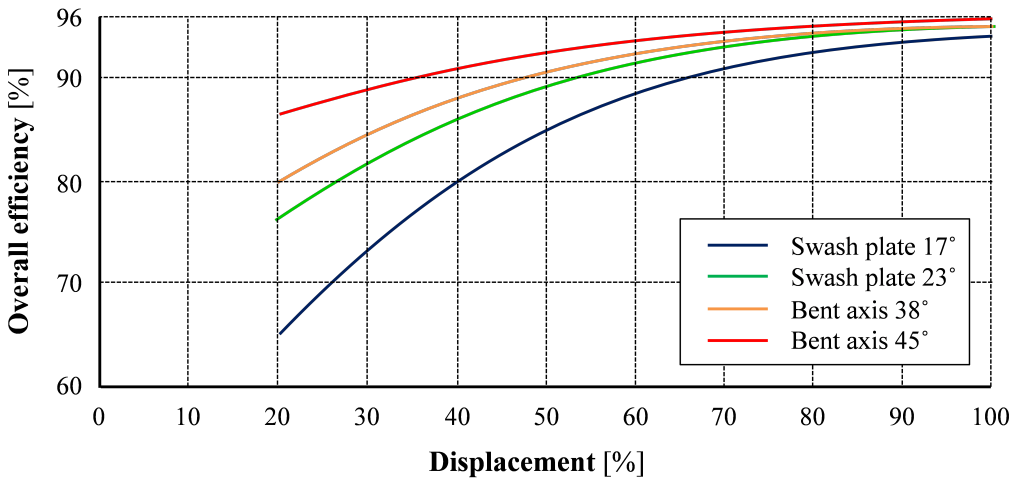

Fig. 1.1. Measured overall efficiency of variable displacement axial piston motors at 2000 rpm and 200 bar (from Baker and Ivantysynova (2009))

achieve the variable displacement capability is complex; moreover, bent axis machines experience shorter life time because of the high loads on the bearings. The swash plate design is instead less complicated, cheaper and has longer lifetime due to the different principle of operation (see Ivantysyn and Ivantysynova, 2001), but the efficiency is much more penalized when the unit operates at partial flow.

The major contribution to the axial piston machine's energy dissipation derives from the rotating kit design and characteristics. A sectioned view of a swash plate type axial piston machine's rotating kit is represented in Fig. 1.2; the three main lubricating interfaces between parts in relative motion are highlighted. The lubricating interfaces represent a key design element, because they have to fulfil simultaneously a bearing and a sealing function: the film of lubricant is fundamental to properly support the high external loads, avoiding metal to metal contact, but the clearance between the parts is subjected to leakages from high to low pressure regions and also to viscous dissipation associated with the fluid flow. Most of the times the lubricating interfaces are the major source of power losses, therefore a deep understanding of the their principle of operation can lead to improved designs, which can raise the

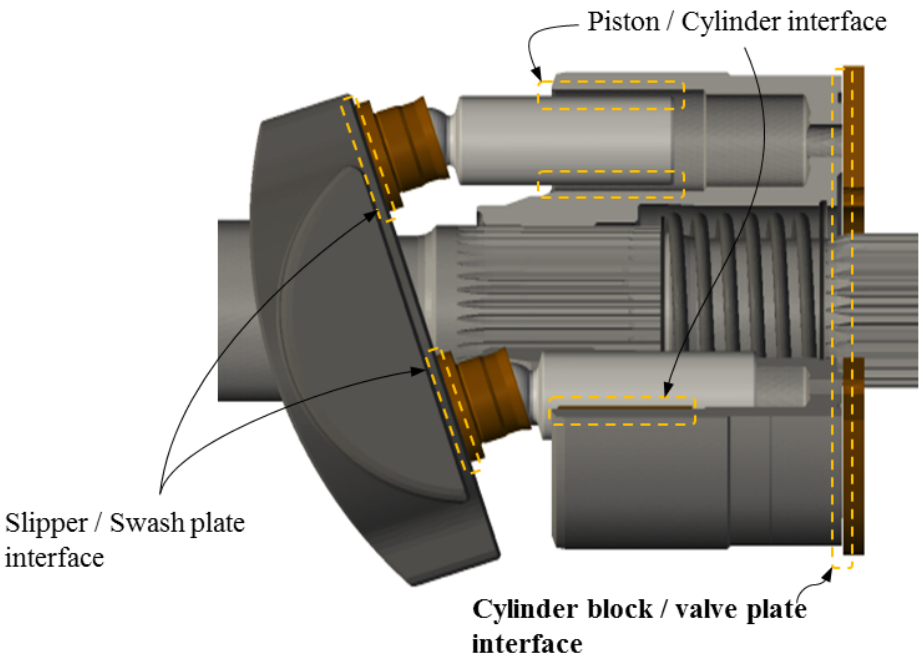

Fig. 1.2. Sectioned view of the rotating kit of a swash plate type axial piston machine

overall axial piston machine efficiency in particular at partial load conditions. This would be extremely appealing on swash plate type machines because it could bring the efficiency curve closer to the bent axis ones, maintaining all the advantages of their simple and effective design.

The cylinder block valve plate interface is present in both the types of axial piston machines and it may contribute significantly to the overall power losses. The principle of operation is similar to a hydrodynamic thrust bearing: the cylinder block rotates relatively to the valve plate, adjusting its position in order to meet the external load condition by changing the pressure field in the fluid film.

The shape of the clearance over time changes not only due the relative inclination of two parts but also due to the so called micro-motion, i.e. an axial motion of the cylinder block of the order of magnitude of a few millimeter per second, which contributes to an additional squeeze film effect. The performance of the interface

however, is affected by a variety of phenomena associated with the normal operation of the machine. All the parts in the rotating kit are subjected to high pressure loads and consequently they deform elastically to an extent which is of the same order of magnitude of the film thickness itself. Furthermore, the energy dissipated due to viscous friction in the fluid flow is transferred to the solid parts, changing their temperature distribution. The steady state temperature distribution in the solid parts influences the fluid film in two ways. First, being the fluid film in the order of magnitude of a few μm the non-isothermal fluid flow in the fluid film is strongly affected by the surface temperature of the solid parts; second, the thermal deflections associated with the heating of the solids are responsible of a further change in the fluid film shape. There are also additional modifications of the fluid film shape which can be due to wear of the solid parts' surfaces or they can be introduced by design, to ensure a stable and optimal lubricating condition.

Many researchers investigated the behavior of the cylinder block / valve plate interface in swash plate axial piston machines; nevertheless, a clear understanding of the interface's behavior has not been reached yet. Furthermore, none of the research attempts conducted so far have ever considered the complex coupling of all the described physical effects in a unique numerical analysis. The aim of this thesis is therefore to address the fundamental need to improve the understanding of the physical phenomena influencing the cylinder block / valve plate interface's performance in axial piston machines. The final goal is the development of a comprehensive model including the required numerical solvers which can predict the formation of the fluid film between cylinder block and valve plate of any kind of piston machine.

1.2 State of the art

The cylinder block / valve plate interface has been subject of many studies in the last 40 years. The research activities can be divided into experimental investigation and development of simulation models of different nature and complexity.

Yamaguchi et al. (1990) studied experimentally the impact of different valve plates on the leakage through the cylinder block / valve plate interface. Kim and Jung (2003) and Kim et al. (2005) focused on the measurement of the film thickness between cylinder block and valve plate for different design: standard flat design, spherical design and additional hydrodynamic bearing pads. An inductive sensor was mounted on the outer region of the cylinder block and the signal was recorder over one shaft revolution. A similar approach was followed by Bergada et al. (2011), the authors mounted three inductive sensors on the valve plate surface coupled with an aluminum disc on the cylinder block's outer surface and measured the film thickness over the three selected point as a function of the angular shaft position. In all these cases though, what was measured was just the relative position of the cylinder block with respect to the valve plate and the film thickness was derived from this information. Not surprisingly, Bergada et al. (2011) found in some situations negative values of the derived film thickness and concluded that deformations effects have to be present and that the actual micro characteristic of the surfaces of cylinder block and valve plate has to be taken into account.

Hong and Lee (2008) studied experimentally the effect CrZrN and TiN plasma coatings on the cylinder block and valve plate plate sliding surfaces, demonstrating that the friction coefficients and the rate of wear sharply decreased thanks to the use of such coatings. This work though, was limited just to low speed or stating condition of the unit, where the hydrodynamic effects can not sustain the loads and mixed lubricating conditions are more likely to appear.

Experimental investigations were directed also towards the thermal behavior of the cylinder block valve plate interface. Olems (2000) concentrated his study on the measurement of the internal temperature field in the cylinder block body. Another work by Jouini and Ivantysynova (2008) presented temperature measurements of the valve plate surface for a swash plate type unit under different operating conditions. Surface temperature measurements are a good indicator of the film thickness because they are very much connected to it through the amount of energy dissipated by

viscous friction; in addition, they are easier to perform and are not subjected to any complication due to the machine dynamic. In both these works the experimental observations were compared to the prediction of a non-isothermal fluid flow model, coupled with a simplified solution of the heat transfer problem in the cylinder block and valve plate. The authors were able to match the main trend but the model's predictions suggested to improve the accuracy and to broaden the physical domains included in the models. Temperature measurements on the rotating kit were carried out also by Kazama et al. (2011); the authors investigated the temperature variation in some fixed point of the cylinder block, valve plate and swash plate as a function of different pressures, speed and oil type. The limited number of thermocuples used did not allow the authors to draw any conclusion about the film thickness, but just general considerations about the thermal behavior of the rotating kit.

For what concerns the modeling of the cylinder block valve plate interface, the overall research activity can be divided into analytical and numerical models.
Sartchenko (1950) described the various forces acting on the cylinder block without going into detail on the nature of those at the interface with the valve plate. Franco (1961) derived the sealing land hydrostatic pressure's radial variation for points away from the valve port ends but he did not account for the pressure field between the two ports of the valve plate. Additional studies, focusing on the analytic prediction of the pressure field based on the principle of the cylinder block's force balance were carried out by Shute and Turnbull (1964), Hibbert et al. (1971), Taylor and Lin (1984), Yamaguchi (1986), Yamaguchi et al. (1990), Yamaguchi (1987), Matsumoto and Ikeya (1991b), Matsumoto and Ikeya (1991a), Manring (2000), Ivantysyn and Ivantysynova (2001). In all these models the cylinder block equilibrium was determined in static conditions with major simplifications in the solution of the Reynolds equation[1]. Moreover, the Reynolds equation was not coupled with the cylinder block's external loads condition and therefore all these models were not able to determine the film thickness

[1]The Reynolds equation is the fundamental equation governing the behavior of laminar flow in narrow fluid films, developed by Reynolds and described in his famous 78 pages long paper, dated 1886 (see Reynolds, 1886).

as a function of the operating conditions: just rough considerations could be made about the behavior of the interface, through a qualitative comparison of the loads with the simplified pressure field that was possible to calculate analytically.

For this reason, the growing need in computational tool to aid the design process, led the researchers towards the development of more advanced numerical models. In these models the Reynolds equation was solved without major simplifications and in some model it was coupled with the Energy equation, to account for the non-isothermal fluid flow in the clearance. The real breakthrough with the numerical model though, was not just the greater accuracy that could be achieved, but rather the possibility of coupling the governing equation of the fluid flow with the external loads condition of the solid parts. Fang and Shirakashi (1995) computed the position of the piston within the cylinder of a swash plate machine considering its force balance and the computation of secondary piston motion, allowing fluid film thickness variations and squeeze film effect to be accounted for the first time within the fluid flow model. The first authors that introduced this innovative approach in the modeling of the cylinder block / valve plate interface were Wieczorek and Ivantysynova (2002): they linked the rigid body dynamics of the cylinder block to the fluid flow through the cylinder block's squeeze term in the Reynolds equation. The Reynolds equation was solved iteratively, by changing the squeeze term until the external loads condition was met; the time integration of the squeeze term yield to the determination the film thickness. The method introduced by Wieczorek and Ivantysynova is based on the observation that the solid parts are free to adjust their position in order to balance the external loads through the hydrodynamic pressure reaction in the lubricant. Nevertheless, also this more advanced model has soon revealed to be poor, especially relatively to the cylinder block valve plate interface. The model was never able of predicting a stable film thickness between cylinder block and valve plate, even in situations were it was certain (from experimental observations) that the interface was working properly. Clearly the model was still too simplified regarding the main physical phenomena involved in the lubrication mechanism.

The first author who tried to incorporate both elastic deformation of the solids and the viscosity-pressure characteristics of the lubricant was Ertel (1939), analyzing the inlet region of lubricated non-conformal machine elements. During the sixties various procedures for solving the complex elastohydrodynamic lubrication problem were reported. Downson and Higginson (1959) described an iterative procedure that solved the elastohydrodynamic problem for line contacts. Then, Houpert and Hamrock (1986) developed an approach that enabled solutions to elastohydrodynamically lubricated rectangular conjunctions with no load limitations. Furthermore, in the seventies the theoretical elastohydrodynamic studies switched from rectangular to elliptical conjunctions. Additional developments in the field considered the thermal problem, analyzing the effects of temperature on the hydrodynamic lubrication process and of the heat transfer mechanisms, as in Zhu and Wen (1984), Sadeghi and Dow (1987) and Kim and Sadeghi (1992). During the last years, the elastohydrodynamic analysis has been applied to different scientific areas, recognizing that the elastohydrodynamic effect is a physical phenomenon not only related to specific tribological contacts, but that addresses, in other forms, further technical applications. In fact, the local surface elastic deformation of mechanical parts subjected to high operating pressures strongly influences the behavior and ultimately the efficiency of machines that are designed to operate with an extremely low film thickness.

The coupling of finite element analysis with the solution of the elastohydrodynamic lubrication problem represents another important field of research for the scopes of this work. Taylor and O'Callaghan (1972) were among the first ones to propose a numerical solution for EHL contacts using finite element analysis. Goenka (1984) conducted a study using FEM of journal bearings lubrication regime; more recently, advanced adaptive numerical methods based on finite element analysis for EHL contact problems have been proposed by Goodyer (2001) and Lu, H. et al. (2005).

The first attempt to include elastohydrodynamic effects in the cylinder block / valve plate interface modeling was by Huang and Ivantysynova (2003): the elastic deformation of the cylinder block due to pressure loads was introduced through a

coupling of the preexisting model by Wieczorek and Ivantysynova (2002) and the commercial code ANSYS by means of an off-line computation method based on the superimposition principle. The new model was able of predicting a stable fluid film and confirmed that the modeling approach was going in the right direction. However, the model of Huang had still many limitations. The Reynolds equation allowed just for the cylinder block to be inclined or deformed, and it could not capture the variation of viscosity along the film; the Energy equation was solved and the temperature in the lubricant could be determined, but the convective effect of leakage was not properly accounted. Furthermore even though the energy dissipated in the fluid flow could be determined, the thermal analysis was not extended to the solid parts.
Other authors started to investigate the impact of the elastic deformation due to pressure loads on the behavior of the cylinder block / valve plate interface: Achten and Schellekens (2006) and Achten and Vael (2010) tried to study the impact of the hydrostatic deformations of cylinder block and valve plate on the leakages and torque losses of the interface, but the FEM analysis were not coupled with the governing equations of the fluid flow and just qualitative considerations could be made. Nevertheless, Achten confirmed the importance of these deformations effects on the interface's performance.

Jouini and Ivantysynova (2008) further developed the model by Huang and Ivantysynova (2003), by adding an heat transfer module, which was able to calculate the steady state temperature field in the cylinder block and valve plate bodies taking into consideration heat fluxes due to energy dissipation in the fluid flow. The discretization approach followed by Jouini and Ivantysynova (2008) did not allow the solid parts to be modeled in a very precise way, and it had shown difficulties in the coupling with the pre-existing non-isothermal elastohydrodynamic model of Huang and Ivantysynova (2003). In addition, even though the temperature fields in the solid parts were calculated, the associated deflection were neglected. Jouini and Ivantysynova compared their simulation results with surface temperature measurements conducted on a 100cc swash plate type axial piston pump. The simulation results captured the

main trend, but the authors concluded that a more precise model was still necessary before this method could be introduced into practical computational pump design.

1.3 Aims

The aim of this work is to improve the fundamental understanding the cylinder block / valve plate interface's operation and to discover the physical phenomena which affect its performance. The biggest unknown of the problem is the fluid film thickness and more importantly how the fluid film changes as the operating condition vary. This objective is met through the formulation of a model where different domains are combined into a unique simulation environment; the ultimate goal is to predict the fluid film thickness under steady state operation of the machine by imposing the dynamic balance of the cylinder block. The non-isothermal fluid flow in the clearance is coupled with the interaction between fluid film and solid part in terms of elasto-hydrodynamic deformations, transient squeeze and conjugate heat transfer effects. The further modifications to the fluid film determined by micro shaping of the surfaces is also considered in the model in order to allow the study of modifications introduced "by design" or associated with wear taking place during the start-up phase. Furthermore, the model is able to account for the impact of different material properties and combinations. In parallel to the model development an important experimental activity has been carried out to validate the theoretical approach and to further consolidate the understanding of the physics.

1.4 Original contributions of this work

The multiphysics simulation model was fully developed with the C++ programming language, in order to couple together all the main physical phenomena affecting the interface's performance in the most efficient and flexible way. The present model represents the most advanced simulation environment for the cylinder block / valve

plate interface ever published and it broadened the knowledge of this complex and fundamental interface thanks to the following specific contributions:

- A generic expression of the Reynolds equation was derived in this work in order to account for both the cylinder block and valve plate surfaces in contact with the lubricant to be arbitrarily inclined or deformed; in addition, the approach presented by Dowson (1962) has been followed to account for changes in viscosity along the film. The new formulation allows for elasto-hydrodynamic and thermal effects on the fluid film to be properly modeled; moreover, the impact of micro surface shaping or wear phenomena can be studied with no limitation.

- The lubricating film's geometry is automatically meshed using directly the CAD drawings: the level of accuracy in the discretized representation of the sealing surfaces is extremely high. The Reynolds and the Energy equations are discretized on the fluid grid through a rigorous implementation of the finite volume method. The new discretization methodology accounts also for the convective effects of leakages in the Energy equation that was neglected in the past.

- A fast and robust linear system solver was introduced for the solution of the fluid flow, allowing the solution residuals to be lower and the computation time to be at least five time faster than the past works. This effort was made to address the need of a very efficient fluid flow solver required to face the fluid structure interaction problem.

- The elastic deformation analysis was extended to all the solid parts that have an impact on the cylinder block / valve plate interface, namely cylinder block, valve plate and end case assembly. For this purpose a finite element solver based on linear tetrahedral elements was developed and coupled directly with the main fluid flow solver. The new finite element elastic deformation model can analyze any kind of part geometry and allows different materials to be combined. The elastic deformation analysis is based on the superimposition method introduced for the first time by Huang and Ivantysynova (2003) for the cylinder block /

valve plate interface, but it does not rely on any external software and is fully automatic.

- The fluid structure interaction problem is solved in the interface through a partitioned fluid structure interaction approach. The convergence between pressure field and elastic deformation is rigorously achieved by means of a dynamic under-relaxation iterative technique.

- The additional transient squeeze effect determined by rate of change of the elasto-hydrodynamic deformations of the solid part was included in the solution of the fluid flow. Moreover it was found that this effect contributes to an important hydrodynamic effect and it is of primary important in the prediction of the load carrying ability of the cylinder block / valve plate interface.

- The heat transfer analysis is extended to all the cylinder block, valve plate and end case bodies; the heat fluxes derived from the accurate solution of the fluid flow in the fluid film are used as a boundary condition on the surrounding surfaces, to determine the steady state temperature of the parts. A CFD methodology was introduced to determine the convection coefficients associated with the other surfaces of the cylinder block, valve plate and end case that exchange heat with the oil in the machine casing or in the displacement chambers, suction and delivery ports.

- For the first time, the thermal deflection resulting from the heating of the cylinder block, valve plate and end case bodies during the machine operations are calculated and used to further correct the film thickness prediction.

- In this work it was found that for a successful coupling with the fluid flow model, the thermal strains of the parts have to be considered just as relative changes rather than overall deformations affecting the clearance geometry.

- In order to fully exploit the developed finite element solver, the heat transfer problem was solved through the finite element formulation, extending the finite

element analysis into the thermoelastic domain. In this way, the elastic deformation due to pressure, the steady state temperature in the solid parts and their associated thermal deflections are calculated with a unique finite element solver, fully integrated in the simulation model.

2. THE CYLINDER BLOCK / VALVE PLATE INTERFACE

The cylinder block / valve plate interface is defined by the fluid film separating the bottom surface of the cylinder block and the top surface of the valve plate; the thickness of the fluid is in the order of magnitude of a few micro-meters. Due to the relative rotation of the cylinder block with respect to the valve plate, the shape of the interface changes continuously over one shaft revolution. Figure 2.1 shows an example of the surface's geometry for the cylinder block and valve plate and the resulting shape of the lubricating interface between them. The region where the

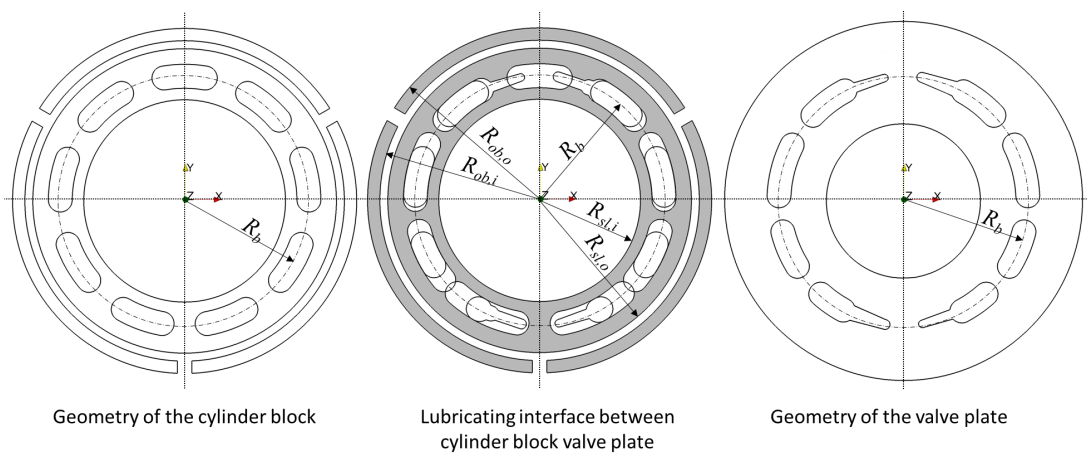

Fig. 2.1. Typical geometrical features of the cylinder block valve plate interface.

sealing takes place is called sealing land and is a disc-shape region defined by the two radii $R_{sl,i}$ and $R_{sl,o}$, containing the cylinder block and the valve plate openings. The cylinder block openings are also called kidney opening, from the typical shape represented in Fig. 2.1; in some designs the cylinder block openings can have a more complicated geometry because additional grooves are machined, usually around the region with smaller curvature (see Fig. 2.2). The openings on the valve plate may

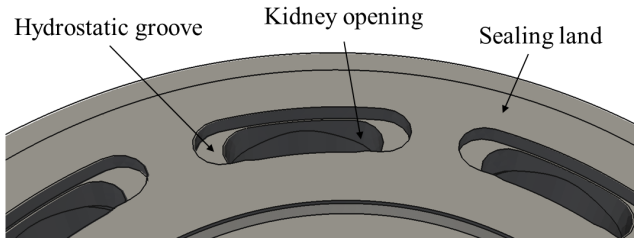

Fig. 2.2. Example of kidney opening with hydrostatic grooves.

have very different shapes, but they are always confined between the inner and outer radius of the kidney opening of the cylinder block, having the same pitch radius R_b. Additional grooves may be present (see Fig. 2.1) to limit pressure spikes and cavitation problems in the displacement chamber, by ensuring a smooth variation in the connection between the displacement chamber and the suction or delivery port.

An additional region, usually called hydrodynamic bearing or outer bearing, can be present and is separated from the sealing land by a circumferential groove, which is at the same pressure of the machine's casing and collects the leakage flow. In Fig. 2.1 the outer bearing is defined by the two radii $R_{ob,i}$ and $R_{ob,o}$. The hydrodynamic bearing may increase the stability of the interface especially at high speed and low load conditions, when to the effect of the centrifugal loads transferred from the piston / slipper assembly can tip the cylinder block away from the valve plate. The hydrodynamic bearing adds additional friction (most of the time not necessary) and for this reason in some design it is shifted of some tens of microns with respect to the sealing land, in order to generate a ticker film in the peripheral region.

Usually it is either the cylinder block or the valve plate surface that determines the actual extent of the sealing land and eventually of the hydrodynamic bearing, if present. In the case illustrated of Fig. 2.1 both sealing land and hydrodynamic bearing were defined by the cylinder block's geometry. However, in some designs the lubricating the interface may be defined by the combination of the geometric features of both the parts.

A common variation to the standard flat design of the two cylinder block and valve plate surfaces is the spherical design of the interface, represented in Fig. 2.3. The

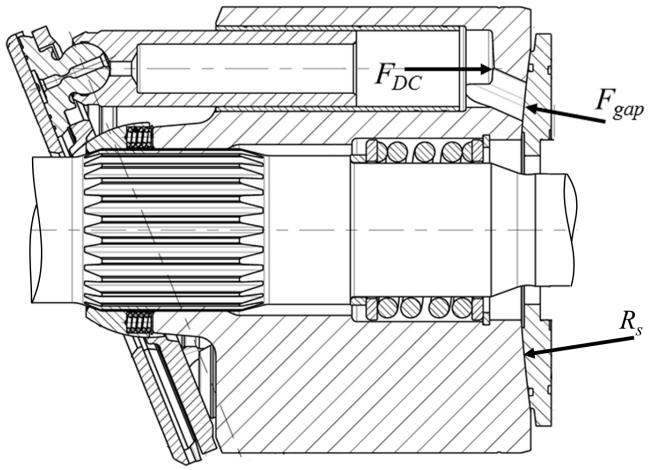

Fig. 2.3. Typical design of the spherical valve plate.

basic idea of this design is to limit the losses associated with the viscous dissipation by reducing the pitch diameter of the kidney ports with respect to the pitch diameter of the cylinder bores in the cylinder block. In this way, for the same cylinder block size, the sliding surface is reduced and consequently the oil in the lubricating interface is subjected to a lower circumferential velocity. As described by Ivantysyn and Ivantysynova (2001), the drawback of this solution is the increased value of the tilting moment acting on the cylinder block, due to the two different lines of action of the resultant axial forces, the force F_{gap} determined by the pressure in the gap and the force F_{DC} determined by the pressure in the displacement chambers. To overcome this problem the spherical design of the sealing surfaces of cylinder block and valve plate was introduced; if properly designed, the spherical valve plate can theoretically reduce the average tilting moment of the cylinder block to zero.

2.1 Axial piston machine kinematics

Figure 2.4 illustrates a section of the rotating kit of an axial piston machine, with the reference system used to define the machine's kinematics. Swash plate type axial

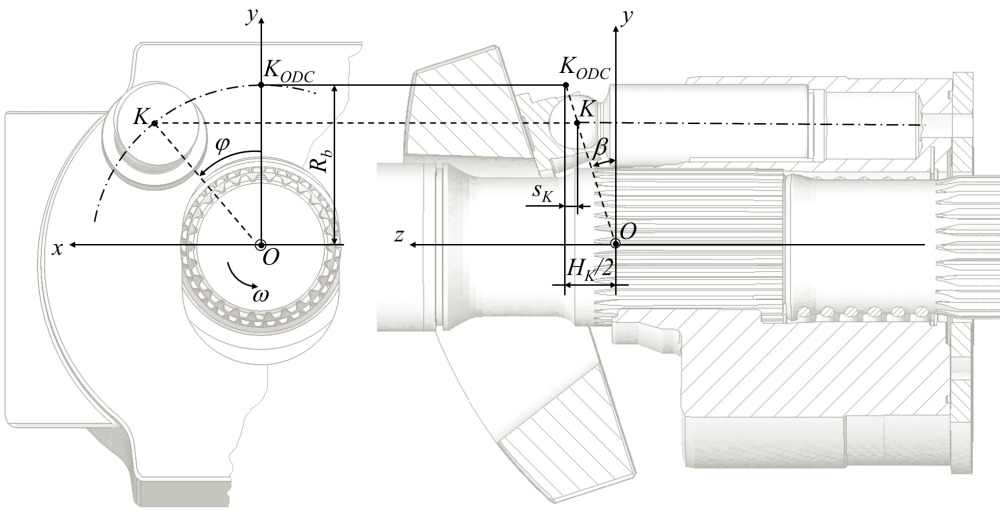

Fig. 2.4. Axial piston machine kinematic.

piston machines can operate in two ways: pumping or motoring mode. In the first case the shaft is driven by an external power source and torque is transferred to the cylinder block through a spline coupling. The cylinder block rotates with the shaft with an angular speed ω, while the valve plate and swash plate remain stationary. Each piston reciprocates axially with different velocity, depending on the angle of the swash plate, β. Thanks to this motion, fluid is drawn at low pressure from the inlet port and discharged at the outlet port while the displacement volume decreases. In case of motoring mode, high pressure fluid enters the machine at the inlet port generating high forces on each piston and consequently available torque on the shaft. Axial piston machines are usually variable displacement, so that the flow can be controlled without changing the shaft speed, just by adjusting the inclination angle of swash plate: larger swash plate angle corresponds to a larger stroke of the pistons, therefore to a higher displacement and delivered flow rate.

The outer dead center ODC is the angular position φ where the piston is at its outer position from the displacement chamber; the outer dead center in Fig. 2.4 corresponds to a shaft angular position $\varphi = 0$. The inner dead center is instead the angular position where the piston is at its inner position to the bottom of the displacement chamber and occurs for $\varphi = \pi$. In the book by Ivantysyn and Ivantysynova (2001) the piston position s_K is identified by the point K (center of the ball joint) and it is expressed relatively to the outer dead center, where $K = K_{ODC}$:

$$s_K(\varphi, \beta) = -R_b \tan\beta(1 - \cos\varphi) \tag{2.1}$$

In Eq. 2.1 R_b is the pitch radius, and β is the angular position of the swash plate. The piston position is always negative according with the direction of the z axis in Fig. 2.4. The total stroke of the piston is indicated with H_K and it can be expressed as follows:

$$H_K = 2R_b \tan\beta \tag{2.2}$$

Based on the maximum piston stroke, the piston velocity, v_K, and the piston acceleration, a_K, can be derived as indicated in Eq. 2.3 and 2.4

$$v_K = \frac{ds_K}{dt} = -\frac{H_K}{2}\omega \sin\vartheta \tag{2.3}$$

$$a_K = \frac{dv_K}{dt} = -\frac{H_K}{2}\omega^2 \cos\vartheta \tag{2.4}$$

Therefore, for a given design of the machine, the piston's sliding velocity and acceleration are a function of the angular position and angular velocity of the shaft.

2.2 Dynamic load condition of the cylinder block

The cylinder block is subjected to a series of external loads which can be divided into two groups. The first containing loads directly applied to the cylinder block body and the second the loads associated with the piston/slipper assemblies which are then transferred to the cylinder block body through the lubricating interfaces between pistons and cylinders.

2.2.1 Loads directly applied to the cylinder block

Figure 2.5 illustrates the loads directly applied to the cylinder block as well as the reference system that will be used to derive the mathematical formulation of the associated dynamic load condition. The z axis coincides with the shaft axis, pointing away from the valve plate. The origin O is determined by the intersection of the z axis with a plane through the centers of the ball joints between pistons and slippers, which is parallel to the swash plate sliding surface. The x axis is parallel to the the swash plate rotation axis and by convention it points towards the high pressure side of the machine. The y axis is determined such that the reference system (x, y, z) has a clockwise rotation.

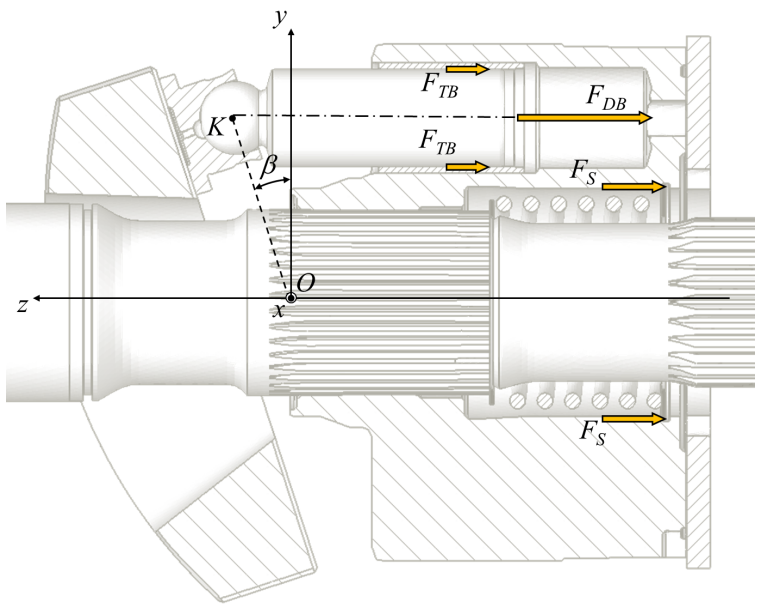

Fig. 2.5. Loads directly applied to the cylinder block.

The main load on the cylinder block is represented by the forces F_{DB}, determined by the pressurized fluid in each of the displacement chamber. The instantaneous pressure in the displacement chambers p_{DC} is calculated using a lumped parameters approach as described in Wieczorek and Ivantysynova (2002), Seeniraj (2009) and

Klop (2010). A typical instantaneous displacement pressure profile is depicted in Fig. 2.6

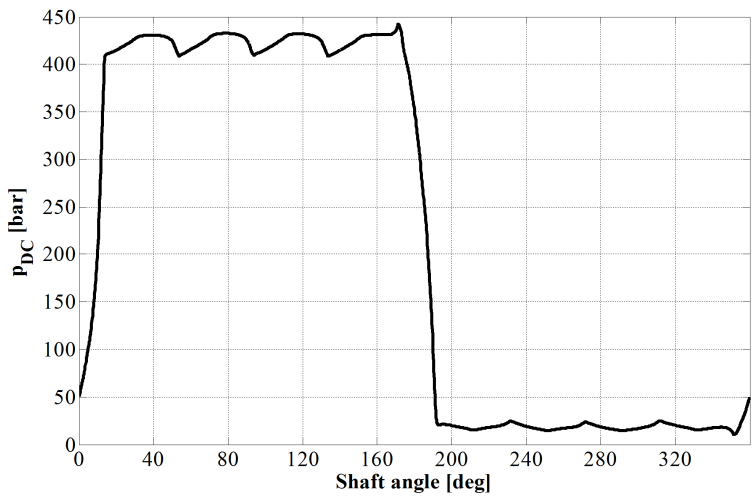

Fig. 2.6. Instantaneous displacement chamber pressure for a 130 cc unit, at 3000 rpm, maximum displacement angle and 400 bar differential pressrure.

The calculation of F_{DB} and its associated moment $\boldsymbol{M}_{DB} = (M_{DBx}, MB_{Dy})$ can be non trivial if the geometry of the displacement chamber is complicated. Figure 2.7 shows an example of a displacement chamber with complex shape characterized by an inclined kidney canal, which is typical in spherical designs. With reference to Fig. 2.7 F_{DB} and $\boldsymbol{M}_{DB}$ can be calculated for one displacement chamber as in Eq. 2.5.

$$\begin{cases} F_{DB} = \int\limits_{A_{DC}} dF_{DB} = \int\limits_{A_{DC}} d(pda)\boldsymbol{n} \cdot \boldsymbol{k} \\ \boldsymbol{M}_{DB} = \int\limits_{A_{DC}} d\boldsymbol{M}_{DB} = \int\limits_{A_{DC}} \boldsymbol{r} \times (pda)\boldsymbol{n} \end{cases} \tag{2.5}$$

In this work Eq. 2.5 is calculated numerically using a discretized geometry of the displacement chamber, which can be provided by any CAD software. The calculation is made by applying a reference pressure of 1 bar, for a shaft angular position $\varphi = 0$

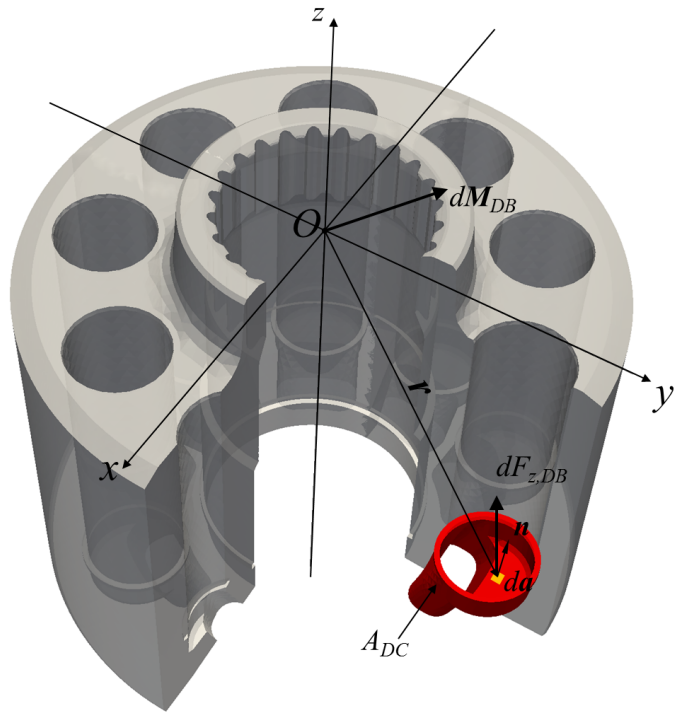

Fig. 2.7. Calculation of force and moment associated with the pressurized fluid in the displacement chamber

in Fig. 2.5 (in this situation the displacement chamber is centered around the y axis, as shown in Fig. 2.7). The reference force and moment are expressed by Eq. 2.6.

$$\begin{cases} F_{DB}^{0} \approx \sum_{i} da_i \boldsymbol{n_i} \cdot \boldsymbol{k} \\ \boldsymbol{M}_{DB}^{0} \approx \sum_{i} \boldsymbol{r}_i \times da_i \boldsymbol{n}_i \end{cases} \tag{2.6}$$

The loads on the block due to the pressurized fluid in one of the displacement chambers at shaft position φ and instantaneous pressure p_{DC} can be calculated as a function of F_{DB}^{0} and $\boldsymbol{M}_{DB}^{0}$, as indicated in Eq. 2.7.

$$\begin{cases} F_{DB} = p_{DC} F_{0,DB} \\ M_{DBx} = p_{DC} \left(M_{DBx}^{0} \cos\varphi + M_{DBy}^{0} \sin\varphi \right) \\ M_{DBy} = p_{DC} \left(-M_{DBx}^{0} \sin\varphi + M_{DBy}^{0} \cos\varphi \right) \end{cases} \tag{2.7}$$

The cylinder block is further pushed towards the valve plate by the action of a spring, which generates a constant axial thrust F_S. This force is necessary to ensure the stability of the cylinder block at low pressure and high speed operation: in this condition the centrifugal load on the piston/slipper assembly would otherwise force the cylinder block to tip away from the valve plate. Moreover, at high speed and low pressure operation also the viscous friction force due to the reciprocating motion of the pistons, F_{TB}, may become important in the balance of the block.

The total direct load on the cylinder block body can be expressed as indicated in Eq. 2.8.

$$\begin{cases} F_B = F_S + F_{TB} + \sum_{i=1}^{z} p_{DC_i} F_{0,DB} \\ M_{Bx} = \sum_{i=1}^{z} p_{DC_i} \left(M^0_{DBx} \cos\varphi_i + M^0_{DBy} \sin\varphi_i \right) \\ M_{By} = \sum_{i=1}^{z} p_{DC_i} \left(-M^0_{DBx} \sin\varphi_i + M^0_{DBy} \cos\varphi_i \right) \end{cases} \tag{2.8}$$

The summations in Eq. 2.8 account for the z displacement chambers in the machines. Figure 2.8 shows an example of calculated F_{Bz}, M_{Bx} and M_{By} over one shaft revolution, for 9 pistons unit, running at a speed of 2000 rpm, 200 bar of differential pressure and 50% displacement. The magnitude of the y-moment is the biggest because by convention the high pressure side is on the right of the y axis and the main component of the moment associated to F_{DB} is hence in the positive y direction. However, the x component of the moment generated by F_{DB} is not zero because the unit has an odd number of pistons and therefore the displacement chambers at high pressure are not exactly symmetric with respect to the x axis.

2.2.2 Loads associated with the piston/slipper assembly

The loads acting on the piston/slipper assembly are illustrated in Fig. 2.9. The piston is loaded on its bottom surface by the pressurized fluid, which determines an axial force F_{DK}. The magnitude of F_{DK} is very similar to F_{DB} but has opposite sign; moreover in the case of the standard design represented in Fig. 2.5 the line of action of F_{DK} coincides with the one of F_{DB}. The sum of F_{DK}, of the inertia force F_{mK}

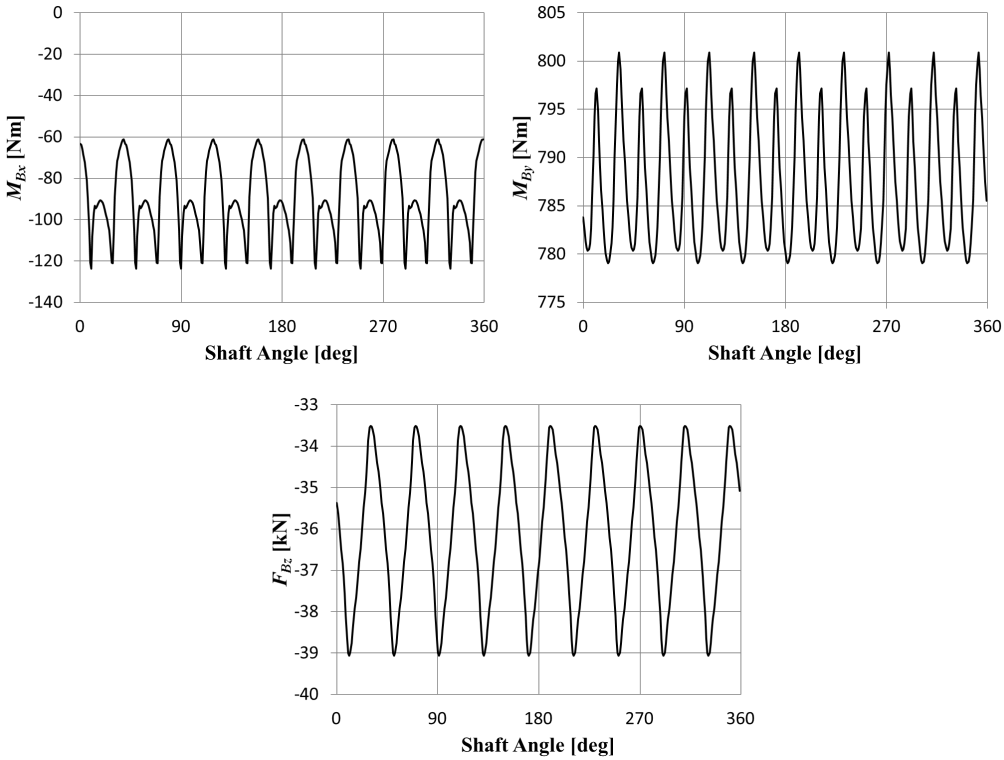

Fig. 2.8. Example of F_{Bz}, M_{Bx} and M_{By} over one shaft revolution. $\Delta p = 200\text{bar}, n = 2000\text{rpm}, \beta = 100\%$

on the piston/slipper assembly and the friction force $-F_{TK}$ determines the resultant axial load F_{AK}, which needs to be balanced by the reaction of the swash plate. Due to the swash plate inclination, the reaction force $\boldsymbol{F}_{SK}$ defines an angle β with the cylinder bore axis. As indicated in Ivantysyn and Ivantysynova (2001) the magnitude of $\boldsymbol{F}_{SK}$ can be expressed by Eq. 2.1.

$$F_{SK} = \frac{F_{AK}}{\cos\beta} = \frac{F_{DK} + F_{mK} - F_{TK}}{\cos\beta} \tag{2.9}$$

The centrifugal force $\boldsymbol{F}_{\omega K}$ on the piston slipper assembly acts on a plane normal to the shaft axis and therefore has two components defined by Eq. 2.10.

$$\begin{cases} F_{\omega Kx} = m_{KG} R_b \omega^2 \sin\varphi \\ F_{\omega Ky} = m_{KG} R_b \omega^2 \cos\varphi \end{cases} \tag{2.10}$$

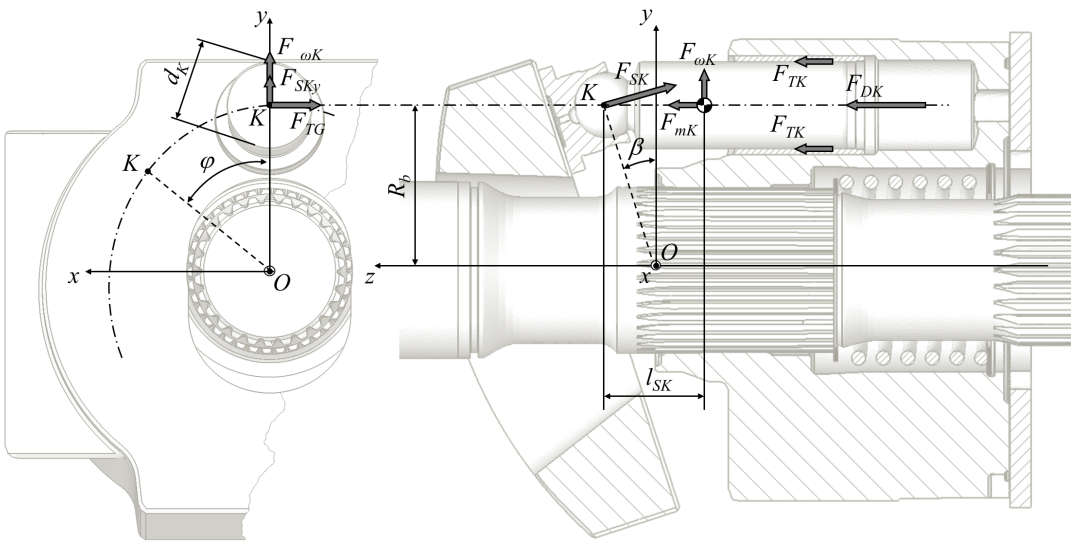

Fig. 2.9. External loads acting on the piston/slipper assembly.

In Eq. 2.10 m_{KG} is the mass of the piston/slipper assembly and ω is the angular velocity of the machine. As shown in Fig. 2.9, $\boldsymbol{F}_{\omega K}$ is applied in the center of mass of the piston slipper assembly, at a distance l_{SK} from the point K. The friction force $\boldsymbol{F}_{TG}$ produced in the sliding surface of the slipper during its relative motion with respect to the swash plate is assumed to be applied at point K; the components in the $x - y$ plane, are expressed by Eq. 2.11.

$$\begin{cases} F_{TGx} = -F_{TG}\cos\varphi \\ F_{TGy} = F_{TG}\sin\varphi \end{cases} \tag{2.11}$$

The set of described loads is applied to the piston / slipper assembly. During the operation of the machine these loads are balanced by the pressure field in the fluid film between piston and cylinder bore, which represents the actual load on the cylinder block. Therefore, in principle the loads transferred to the cylinder block by the piston / slipper assembly should be calculated by considering this pressure field. Nevertheless, since the equilibrium of the piston/slipper assembly must always be satisfied, the total load associated with the pressure field in the fluid film between piston and cylinders has to be equal and opposite to the resultant loads associated

with the external loads on the assembly. This resultant load is characterized by the two moments expressed by Eq. 2.12 and it represent the actual load on the cylinder block transferred by the piston / slipper assembly.

$$\begin{cases} M_{KBx} = -\sum_{i=1}^{z} F_{SKy} s_{Ki} + F_{\omega Ky}(s_{Ki} - l_{SK}) + F_{TGy} s_{Ki} \\ M_{KBy} = \sum_{i=1}^{z} F_{\omega Kx}(s_{Ki} - l_{SK}) + F_{TGx} s_{Ki} \end{cases} \tag{2.12}$$

In Eq. 2.12 F_{SKy} is the radial component of the swash plate's reaction. For standard designs, when the swash plate is inclined only around the x axis, just one component in y direction is present; however, some designs present a second small angle of inclination of the swash plate around the y axis. This design is known as cross-angle and in this case $\boldsymbol{F}_{SK}$ has a component also in x direction, which contributes to an additional y-moment on the cylinder block.

Figure 2.11 illustrates the loads transferred to the cylinder block by the piston / slipper assembly for a 130 cc unit, at 3000 rpm, maximum displacement angle and 400 bar differential pressure, where the friction force from the slipper was neglected. It is interesting to notice that the y-moment is Fig. 2.11 is zero. The friction force

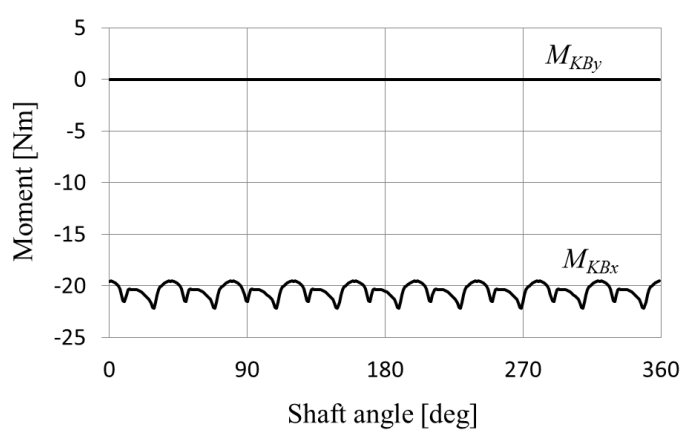

Fig. 2.10. Representation of the loads transferred to the cylinder block by the piston / slipper assembly for a 130 cc unit, at 3000 rpm, 400 bar differential pressure and 50% displacement angle.

transferred from the slipper was neglected and thus the y-moment of the centrifugal

force has to be zero. From Eq. 2.1 and 2.12, the expression of the moment associated with the centrifugal force is the following.

$$\begin{cases} M_{KB\omega_x} = -\sum_{i=1}^{z} m_{KG}\omega^2 R_b \cos\varphi_i \left(R_b \tan\beta(1-\cos\varphi_i) + l_{SK}\right) \\ M_{KB\omega_y} = -\sum_{i=1}^{z} m_{KG}\omega^2 R_b \sin\varphi_i \left(R_b \tan\beta(1-\cos\varphi_i) + l_{SK}\right) \end{cases} \tag{2.13}$$

In the case of the y component, the the sum in Eq. 2.13 is zero if

$$\begin{aligned} \sum_{i=0}^{z-1} \sin\varphi_i \left(1-\cos\varphi_i\right)) &= \sum_{i=0}^{z-1} \left(\sin\varphi_i - \frac{\sin 2\varphi_i}{2}\right) = \\ &= \sum_{i=0}^{z-1} \sin\varphi_i - \sum_{i=0}^{z-1} \frac{\sin 2\varphi_i}{2} = 0 \end{aligned} \tag{2.14}$$

Considering the first summation, by expanding and expressing φ_i as $2\pi i/z$

$$\begin{aligned} \sum_{i=0}^{z-1} \sin\varphi_i &= 0 + \sin\frac{2\pi}{n} + \sin\frac{4\pi}{n} + ... + \sin\frac{2\pi(n-2)}{n} + \sin\frac{2\pi(n-1)}{n} = \\ &= 0 + \sin\frac{2\pi}{n} + \sin\frac{4\pi}{n} + ... - \sin\frac{2\pi - 2\pi(n-2)}{n} - \sin\frac{2\pi - 2\pi(n-1)}{n} = \\ &= 0 + \sin\frac{2\pi}{n} + \sin\frac{4\pi}{n} + ... - \sin\frac{4\pi}{n} - \sin\frac{2\pi}{n} = 0 \end{aligned} \tag{2.15}$$

The exact same derivation can be carried out for the second term in Eq. 2.14, proving that the y-moment will always be zero[1].

With a similar approach it can be shown that the x moment in Eq. 2.13 is instead different from zero, which confirms that the centrifugal loads transferred from the piston / slipper assembly to the cylinder block can actually become problematic when the machine operates at very high speed.

2.2.3 The reaction in the spline joint

The loads on the piston / slipper assembly do not just generate a x-moment on the cylinder block: the pressure in the fluid film between piston and cylinders also determines a radial imbalance that has to be carried by the shaft. On the other

[1]Actually the derivation in Eq. 2.15 is rigorous only in the case of an odd number of pistons, but it can be shown that the same result will be found in the case of an even number of pistons.

hand, a reaction force on the cylinder block is generated in the spline joint with two components expressed as indicated in the following equation.

$$\begin{cases} F_{SRx} = -(F_{\omega Kx} + F_{TGx}) \\ F_{SRy} = -(F_{SKy} + F_{\omega Ky} + F_{TGy}) \end{cases} \tag{2.16}$$

Usually $F_{SRy} \gg F_{SRx}$ because F_{SKy} is much bigger than the other forces and $\boldsymbol{F_{SR}}$ turns out to be mainly in the y direction. Being F_{SKy} the major component, from Fig. 2.11 it is clear that the crowning point of the cylinder block on the spline joint should be located exactly where the point O is. In this way, the reaction force

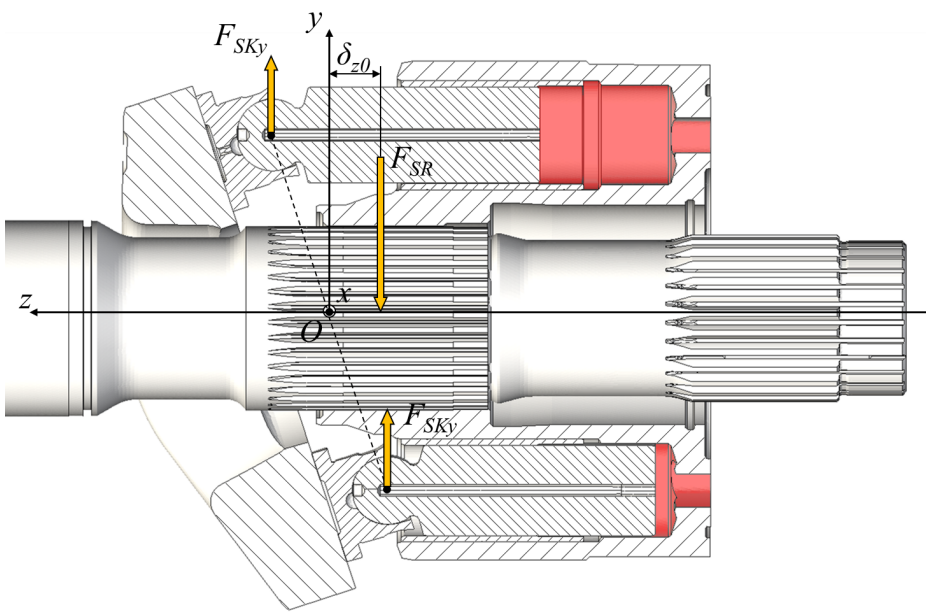

Fig. 2.11. Representation of F_{SKy} for two different pistons on the high pressure region of the machine. The reaction of the shaft on the radial load is also represented as F_{SR}.

F_{SR} would not contribute to any moment with respect to the point O; moreover the moments generated by the different F_{SKy} on the high pressure side would more or less compensate each other and the tipping moment on the cylinder block would be minimized. Nonetheless, in some designs the crowning point can differ from the ideal point O. Figure 2.11 represents indeed this situation, where the distance δ_{z_0} indicates

the offset between point O and the actual crowning point. In this case Eq. 2.12 has to be corrected to include the additional moment introduced by the reaction of the shaft:

$$\begin{cases} M_{KBx} = -\sum_{i=1}^{z} F_{SKy} z_{Ki} + F_{\omega Ky}(z_{Ki} - l_{SK}) + F_{TGy} z_{Ki} - \delta_{z_0} F_{SRy} \\ M_{KBy} = \sum_{i=1}^{z} F_{\omega Kx}(z_{Ki} - l_{SK}) + F_{TGx} z_{Ki} - \delta_{z_0} F_{SRx} \end{cases} \tag{2.17}$$

Especially at high pressure and high displacement the additional moment introduced by the shaft's reaction can become significant; Fig. 2.12 shows the variation of its average value over one shaft revolution for a 130 cc unit, at 1000 rpm, 400 bar of differential pressure and maximum displacement angle. As Fig. 2.12 shows, even small

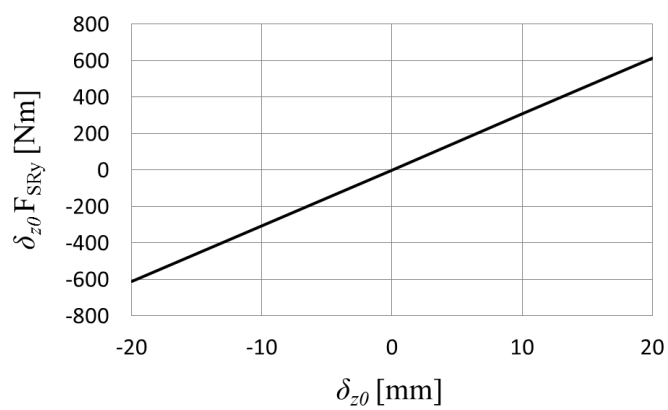

Fig. 2.12. Representation of the additional moment introduced by the shaft reaction on the cylinder block as a function of the crowning point position with respect to the ideal location. Calculated for a 130 cc unit at 1000 rpm, 400 bar and maximum displacement angle.

offsets in the position of the crowning point can generate tilting moments that may become hard to balance by the pressure field in the lubricating interface. Furthermore, the actual position of the crowning point may change with the operating condition due to the deformations of the shaft and it is quite difficult to figure out where exactly the reaction force $\boldsymbol{F_{SR}}$ will be located.

2.2.4 Loads from the pressure field in the fluid film

Likewise the external loads, the loads associated with the pressure field can be represented through a resultant axial force and two moments, in x and y directions, as indicated by Eq. 2.18.

$$\begin{cases} F_{fB} = \int\limits_{\mathscr{S}_{CB}} pda \\ M_{fx} = \int\limits_{\mathscr{S}_{CB}} pyda \\ M_{fy} = -\int\limits_{\mathscr{S}_{CB}} pxda \end{cases} \tag{2.18}$$

In Eq. 2.18 the integrals are calculated over the cylinder's block surface in contact with the fluid film; the reference system is the same of the one depicted in Fig. 2.5.

If the interface is characterized by a spherical design, the calculation of the pressure loads is more complicated. Figure 2.13 illustrates the situation with a cross section (b) and shows how to decompose the resulting pressure force $\boldsymbol{F}$ into the three components F_x, F_y and F_z. The pressure force $\boldsymbol{F}$ acts normal to the spherical surface of the cylinder block; with reference to Fig. 2.13(a) the components of $\boldsymbol{F}$ with respect to the reference system (x, y, z) are the following

$$\boldsymbol{F} = \boldsymbol{i}(F\sin\alpha)\sin\varphi + \boldsymbol{j}(F\sin\alpha)\cos\varphi + \boldsymbol{k}F\cos\alpha \tag{2.19}$$

For the calculation of the loads associated with the pressure in the fluid film, instead of using the expression in Eq. 2.19 and integrate over the spherical surface, it is convenient to consider the projection of the spherical surface into a plane normal to the z direction, $\mathscr{S}_{CBz}$, as indicated by Eq. 2.20

$$\begin{cases} F_{fB} = \int\limits_{\mathscr{S}_{CBz}} (pda) \\ M_{fx} = \int\limits_{\mathscr{S}_{CBz}} y(pda) + \int\limits_{\mathscr{S}_{CBz}} z(pda)\tan\alpha\cos\varphi \\ M_{fy} = -\int\limits_{\mathscr{S}_{CBz}} x(pda) - \int\limits_{\mathscr{S}_{CBz}} z(pda)\tan\alpha\sin\varphi \end{cases} \tag{2.20}$$

The resulting axial force is determined by F_z whereas the other two components generate additional moments in x and y directions, which are normally not present

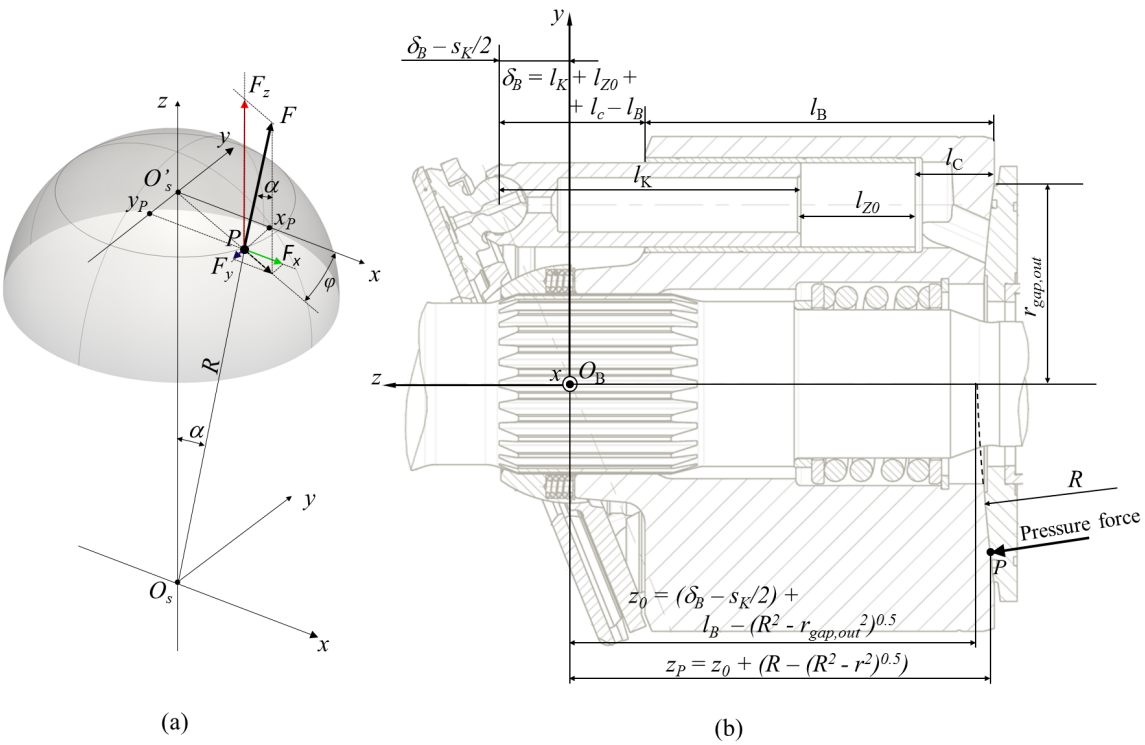

Fig. 2.13. Pressure load calculation with the spherical design.

in the standard design; the additional moments help to balance the tilting moment coming from the different lines of action of the external and fluid forces depicted in Fig. 2.3. The moment arm z in Eq. 2.20 is calculated as illustrated in Fig. 2.13(b).

2.3 Principle of operation and associated physical phenomena

The external loads on the cylinder block have been discussed in detail the previous section. The total external load on the cylinder block is expressed by Eq. 2.21.

$$\begin{cases} F_B = Fs + F_{TB} + \sum_{i=1}^{z} p_{DC_i} F_{0,DB} \\ M_{Bx} = \sum_{i=1}^{z} \left[p_{DC_i} \left(M^0_{DBx} \cos\varphi_i + M^0_{DBy} \sin\varphi_i \right) + \right. \\ \qquad \left. -F_{SKy} z_{Ki} - F_{\omega Ky}(z_{Ki} - l_{SK}) - F_{TGy} z_{Ki} + \delta_{z_0} F_{SRy} \right] \\ M_{By} = \sum_{i=1}^{z} \left[p_{DC_i} \left(-M^0_{DBx} \sin\varphi_i + M^0_{DBy} \cos\varphi_i \right) + F_{TGx} z_{Ki} \right] \end{cases} \tag{2.21}$$

Figure 2.14 illustrates the force and the two moments expressed through Eq. 2.21 for a 130cc unit, operating at a speed of 2000rpm, a differential pressure of 200 bar and 50% displacement. The external loads on the cylinder block are obviously a function of the operative conditions in terms of differential pressure, machine speed and swash plate angle but it is important to underline that even under steady state operation the load condition is a function of the shaft angle, due to the kinematic of the machine and the oscillating pressure in the displacement chambers.

For a reliable operation of the machine the external loads have to be balanced by the pressure field in the fluid film between cylinder block and valve plate; moreover, the cylinders block / valve plate interface has also to fulfill a sealing function. The design of the interface is therefore problematic, representing a trade-off among opposite requirements: the interface should provide a very thin lubricating film to limit the leakage flow; on the other hand this would dramatically increase the energy dissipated by viscous friction. Furthermore, to minimize possible conditions of mixed lubrication, with a consequent extensive wear of the solid parts, an adequate film of lubricant should always be present.

In the past decades the design of the interface have been carried out by combining good experience with a slow and expansive trial and error practice, because the mechanisms governing the pressure generation in the fluid film were mainly unknown. The goal of this section is to introduce and describe qualitatively the physical

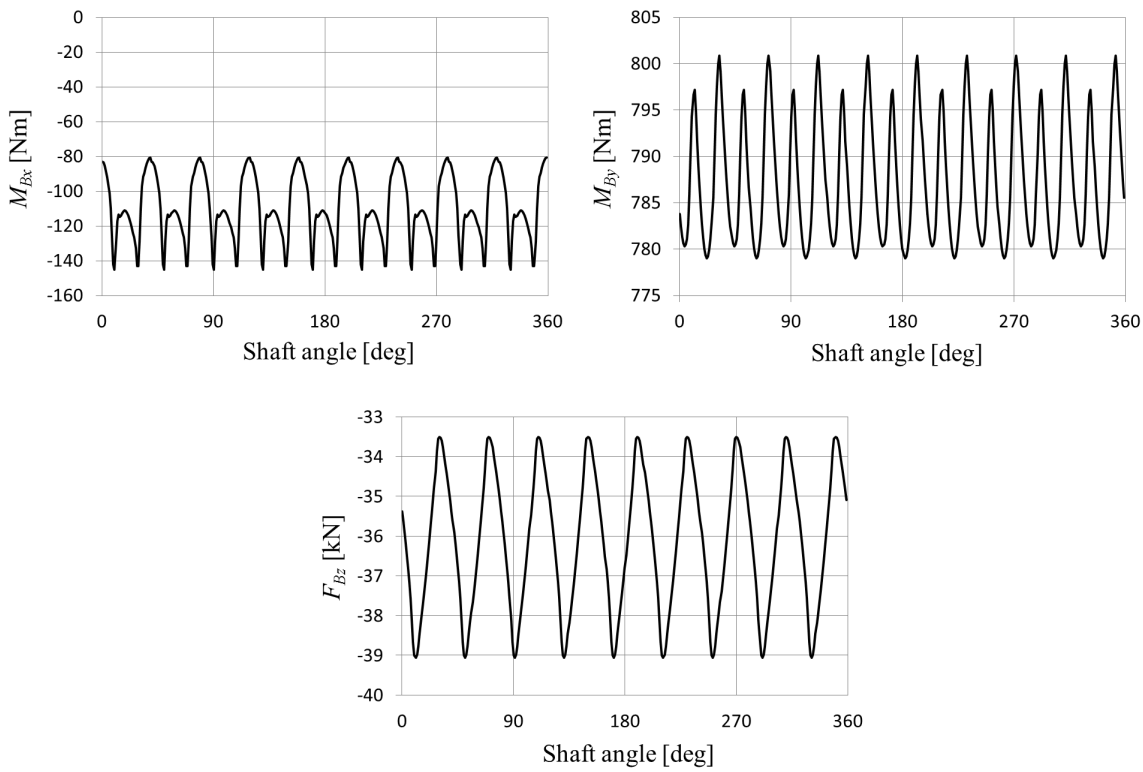

Fig. 2.14. Total external loads on the cylinder block, for a 130cc unit operating at 2000 rpm, under a differential pressure of 200 bar and 50% displacement.

phenomena that have been identified as crucial in the correct prediction of the load carrying ability of the interface and more in general in the determination of its overall performance.

The pressure field in the fluid film is governed by the Reynolds equation. As already anticipated, at this point the focus is on the physics behind the pressure generation in the fluid film rather than on the mathematical details of its expression, which will be discussed later (see Sec. 2.5.1 and Appendix A). In general the pressure field is characterized by a hydrostatic and a hydrodynamic component. The first is determined by the diffusion of pressure from the boundaries of the fluid film; the hydrostatic component is not sufficient to meet the oscillating nature of the external

loads on the cylinder block and the hydrodynamic component becomes therefore fundamental for a correct operation of the lubricating interface.

Hydrodynamic pressure components in the cylinder block / valve plate interface can be generated in a variety of different ways. The most intuitive is the combination of the cylinder block's rotation with its relative inclination with respect to the valve plate surface; this effect is called physical wedge (Hamrock et al. (2004)) and it represents one of the most effective ways to build up hydrodynamic pressure.

Indeed, the machine could not work if the cylinder block was not able to adjust its relative position with respect to the valve plate in order to meet the external load condition. This degree of freedom is usually guaranteed by the proper design of the spline joint between cylinder block and shaft, which not only transfers the driving torque from the shaft, but it also allows the cylinder block to translate in axial direction as well as rotate around the x and y axis with minimal resistance. Some machines do not utilize a spline, being the cylinder block and the shaft part of the same assembly (see Ivantysyn and Ivantysynova (2001)); in this case the required degrees of freedom to the cylinder block have to rely on the proper design of the shaft's bearing.

Another important phenomenon are the squeeze effects, which can be divided into translational and normal squeeze. The translational squeeze can be generated by any kind micro modification of one or both of the surfaces bounding the fluid film. In this case, hydrodynamic effects are present just because there is relative motion of the cylinder block with respect to the valve plate; no relative inclination of the parts is necessary. These modifications are represented by manufacturing imperfections, wear or elastic deformations of the solid parts associated with the normal operation of the machine.

The pressurized fluid in the machine generates two different types of deformations, known as elasto-hydrostatic and elasto-hydrodynamic. Elasto-hydrostatic deformations are associated with a pressure field that is pretty much "static" and therefore the result is a constant modification of the lubricating interface over time. This is the

case of the pressurized fluid in the displacement chambers or in the ports of the valve plate. With the exception of the rapid transition from low to high pressure port (and vice-versa) these surfaces are loaded with a pressure that is fairly constant in time, as illustrated in Fig. 2.6.

On the other hand the elasto-hydrodynamic deformation is a more complex phenomenon that results from a fluid-structure interaction between the hydrodynamic pressure component in the fluid film and the consequent local deformation of the solid parts. Elasto-hydrodynamic deformations take place where the fluid film is low; Hamrock et al. (2004) define a dimensionless film parameter as the ratio between the minimum film thickness and the combination of the rms surface finish of the two surfaces

$$\Lambda = \frac{h_{min}}{\sqrt{R_{q,a}^2 + R_{q,b}^2}} \tag{2.22}$$

Typically elasto-hydrodynamic lubrication occur when $3 < \Lambda < 10$, for higher value of the dimensionless film parameter there is not really a considerable interaction between pressure field and fluid film.

Elasto-hydrodynamic deformations are not only important because they may contribute to a naturally-induced translational squeeze effect; their dynamic character leads to a second very important effect which can be associated with the so called "normal squeeze". In general the normal squeeze effect identifies the action of squeezing the fluid film in the direction normal to its thickness. This effect is important for the cylinder block / valve plate interface and it is in part achieved through the axial micro-motion of the cylinder block, which adjust its position to meet the external load condition through a slight and oscillating motion characterized by velocities in the order of magnitude of a few millimeters per second. On the other hand, the rapid change in hydrodynamic deformation over time represents an additional normal squeeze component, named transient "EHD squeeze"; this effect was first time introduced in the modeling of the cylinder block valve plate interface in the present work. This research study discovered that the EHD squeeze plays an important role

in the prediction of the actual load carrying ability of the interface, especially when the interface operates extensively under elasto-hydrodynamic lubrication.

Elastic deformation of the parts are not limited to pressure loads though. The lubricating interfaces in axial piston machines are among the most important sources of mechanical loss due to the viscous friction in the fluid flow; the heat generated is partially carried off by the leakage, but in the most parts it contributes to the heating of the solid parts. The change in temperature in the fluid alters its properties and the change in temperature in the components of the rotating kit introduces temperature-induced strains which result in a further elastic deformation. The effect of thermal deflection of the solid parts on the prediction of the fluid film in the cylinder block / valve plate interface was investigated for the first time in this work and it was found that thermal deflections of the solid parts are of the same order of magnitude of the film thickness itself, affecting the the fluid film as much as pressure deformations.

The temperature of the solid parts can be assumed to be stationary because, after a transient phase, an equilibrium is reached between the energy dissipated in the fluid flow and the heat carried off by convection in the flow and diffusion through the solid parts. Temperature measurements carried out in this work and presented in chapter 7 have confirmed that the solid parts are characterized by a static temperature distribution under steady state conditions, the same conclusion was also found by other authors (see Olems, 2000; Jouini and Ivantysynova, 2008).

2.4 Fluid film geometry

In absence of any phenomena altering the shape of the solid parts, the geometry of the clearance is defined by the relative position of the cylinder block with respect to the valve plate. Figure 2.15 illustrates the clearance's geometry when the cylinder block is slightly rotated around the x axis, generating a thinner film region around point P_1. In the described condition the clearance's geometry can be expressed in any point P if the position of the cylinder block is known with respect to the valve plate

surface (plane $z = 0$) at the three control points P_1, P_2 and P_3, depicted in Fig. 2.15. With respect to the cylindrical reference system (r, ϑ, z) represented in Fig. 2.15 the

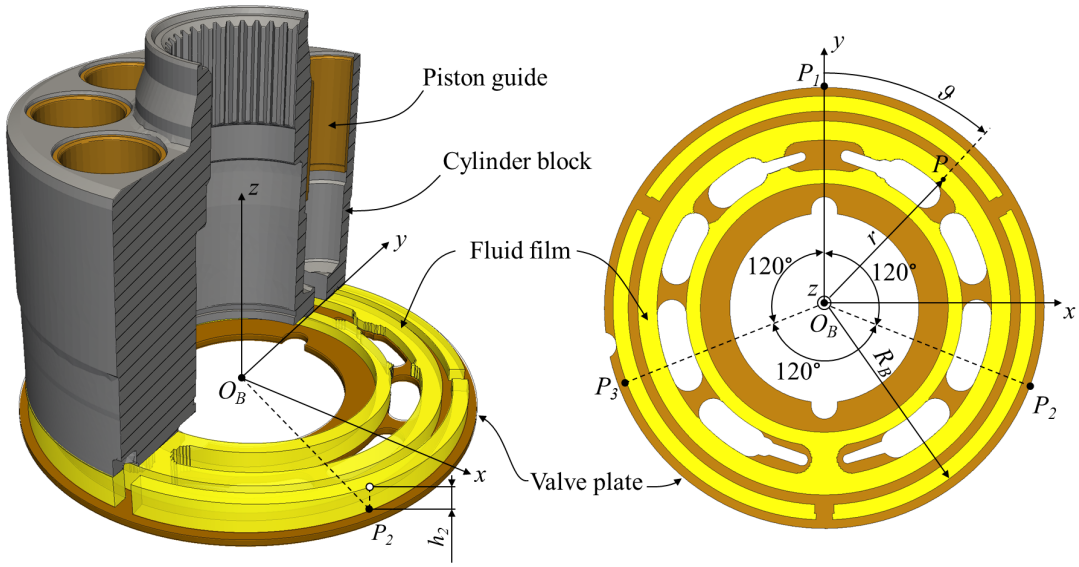

Fig. 2.15. Ideal situation of non-deformable solid parts. The clearance geometry is defined by the relative position of the cylinder block with respect to the valve plate.

clearance's geometry $h(r, \vartheta)$ is expressed by Eq. 2.23, as found by Wieczorek and Ivantysynova (2002).

$$h(r,\vartheta) = \frac{1}{\sqrt{3}R_B} r \sin\vartheta (h_{P_2} + h_{P_2}) + \frac{1}{3R_B} r \cos\vartheta (2h_{P_1} - h_{P_2} - h_{P_3}) + \\ + \frac{1}{3}(h_{P_1} + h_{P_2} + h_{P_3}) \tag{2.23}$$

Equation 2.23 is based on an ideal situation and it is not sufficient to describe the complex shape of the clearance during the normal operation of the machine; neither can be used to study the effect of any micro surface shaping introduced by design. When the elastic deformation of solid parts, or micro surface shaping are introduced, the boundary surfaces are no longer planes but surfaces characterized by a complex geometry. In this case the clearance geometry is calculated in three steps:

1. The solid parts are assumed to be non-deformable. In this condition the valve plate surface is described by the plane $z = 0$ in Fig. 2.15 and the cylinder block bottom surface by the plane through three points described by Eq. 2.23.

2. If present, micro-surface patterns are summed to the ideal position calculated in step 1.

3. For both the solid parts, the components in the fluid film thickness direction of the elasto-hydrodynamic and and thermal deformations are summed to the clearance geometry determined in step 2.

The cylinder block and the valve plate surfaces are therefore defined by their relative position with respect the reference plane $z = 0$, named h_{CB} and h_{VP} respectively, as shown in Eq.2.24.

$$\begin{cases} h_{CB}(r,\vartheta) = \dfrac{1}{\sqrt{3}R_B} r \sin\vartheta (h_{P_2} + h_{P_2}) + \dfrac{1}{3r_B} r \cos\vartheta (2h_{P_1} - h_{P_2} - h_{P_3}) + \\ \qquad + \dfrac{1}{3}(h_{P_1} + h_{P_2} + h_{P_3}) + \delta h_{CB}(r,\vartheta) \\ h_{VP}(r,\vartheta) = \delta h_{VP}(r,\vartheta) \end{cases} \tag{2.24}$$

The terms $\delta h_{CB}(r,\vartheta)$ and $\delta h_{VP}(r,\vartheta)$ in Eq. 2.24 incorporate the cylinder block and valve plate elastic deformations and thermal deflections components in the fluid film thickness direction and, if present, any micro surface shaping. Figure 2.16 shows $h_{CB}(r,\vartheta)$ and $h_{VP}(r,\vartheta)$ in a situation where the cylinder block inclination, fluid film thickness and solid body deformations are all clearly exaggerated, being otherwise impossible to be represented. The fluid film thickness in any point $h(r,\vartheta)$ is expressed by the difference of $h_{CB}(r,\vartheta)$ and $h_{VP}(r,\vartheta)$ as in Eq.2.25.

$$\begin{aligned} h(r,\vartheta) = & \frac{1}{\sqrt{3}R_B} r \sin\vartheta (h_{P_2} + h_{P_2}) + \frac{1}{3R_B} r \cos\vartheta (2h_{P_1} - h_{P_2} - h_{P_3}) + \\ & + \frac{1}{3}(h_{P_1} + h_{P_2} + h_{P_3}) + (\delta h_{CB}(r,\vartheta) - \delta h_{VP}(r,\vartheta)) \end{aligned} \tag{2.25}$$

In Eq. 2.25 the term $\delta h(r,\vartheta) = \delta h_{CB}(r,\vartheta) - \delta h_{VP}(r,\vartheta)$ expresses the correction which needs to be applied to the ideal clearance's geometry when any kind of modification of the cylinder block and valve plate sealing surfaces is present.

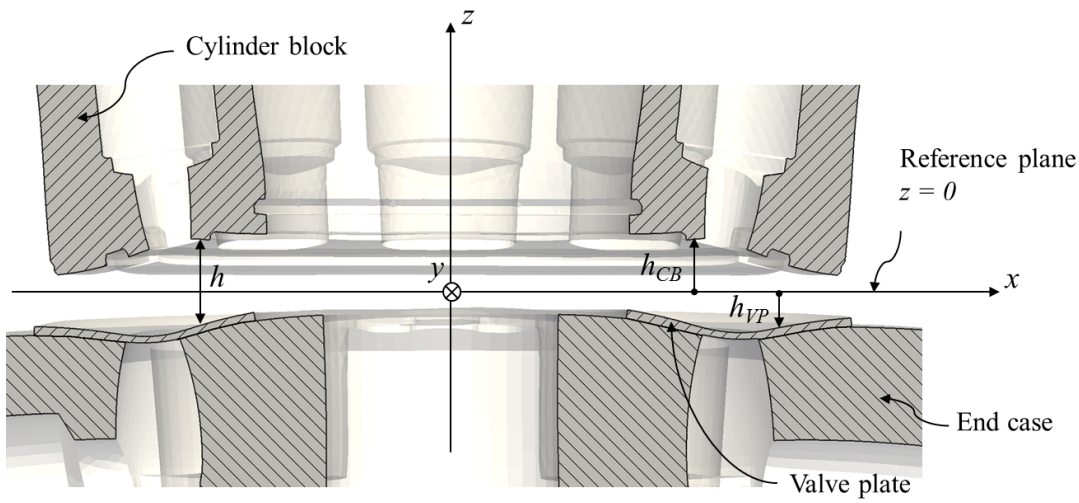

Fig. 2.16. Clearance geometry definition accounting for arbitrary shapes of the cylinder block and valve plate sealing surfaces.

The cylinder block's normal squeeze motion is defined by deriving with respect to time the clearance geometry defined by Eq. 2.25, as indicated in Eq.2.26.

$$\begin{aligned}\dot{h}(r,\vartheta) =& \frac{1}{\sqrt{3}R_B} r\sin\vartheta(\dot{h}_{P_2}+\dot{h}_{P_2}) + \frac{1}{3R_B} r\cos\vartheta(2\dot{h}_{P_1}-\dot{h}_{P_2}-\dot{h}_{P_3}) + \\ &+ \frac{1}{3}(\dot{h}_{P_1}+\dot{h}_{P_2}+\dot{h}_{P_3}) + \Big(\delta\dot{h}_{CB}(r,\vartheta) - \delta\dot{h}_{VP}(r,\vartheta)\Big)\end{aligned} \tag{2.26}$$

The three velocities $\dot{h}_{P_1}$, $\dot{h}_{P_2}$ and $\dot{h}_{P_3}$ represent the magnitude of the cylinder block's micro motion at the three control points P_1, P_2 and P_3 in Fig.2.15. In Eq. 2.26 the term $\delta\dot{h}(r,\vartheta) = \delta\dot{h}_{CB}(r,\vartheta) - \delta\dot{h}_{VP}(r,\vartheta)$ is the transient squeeze effect due to the elastic surface deformation, already introduced as EHD squeeze in the previous section.

In the case of spherical design, the definition of the clearance's geometry can still be expressed using Eq. 2.25, assuming the the film thickness is the defined in the direction normal to the spherical surface.

2.5 The non-isothermal fluid flow in the clearance

The clearance between cylinder block and valve plate is in the order of magnitude of at most a few tens of micro-meters and typical values of the kinematic viscosity of the working hydraulic fluid at atmospheric pressure vary from about 100 to 3 cSt for temperature ranging from 30 to 120 C. The maximum magnitude of the fluid flow velocity V can be estimated from the typical value of maximum unit speed and dimension: assuming 4000 rpm and 100 mm for the cylinder block diameter the value turns out being about 20 m/s. In this extreme conditions, the Reynolds number is given by Eq. 2.27 and it is safe to consider the flow to be laminar in all the range of operating conditions of the interface (most of the time the Reynolds number is indeed smaller than 10).

$$Re = \frac{Vh}{\nu} = \frac{20 \cdot (15 \cdot 10{-}6)}{3 \cdot 10^{-6}} \approx 100 \tag{2.27}$$

The governing equations of the non-isothermal fluid flow in the clearance are the Reynolds and the Energy equation. The first describes the pressure distribution and in this work it was derived specifically for the cylinder block / valve plate interface to account for elastic deformations on both the surfaces and eventual micro modifications to the surface introduced by design. The second equation determines the temperature distribution in the lubricant; furthermore it allows the heat fluxes heating the solid part to be estimated as a consequence of the energy dissipated in the fluid flow by viscous friction.

An accurate solution of the governing equation and ultimately the reliable prediction of the fluid film can be achieved only if the properties of the fluid are well characterized as a function of pressure and temperature. In this work the fluid properties were modeled through analytic correlations derived from measurements; Appendix B illustrates the derivation of the equation used to characterized the viscosity, density and bulk modulus of the fluid that has been used for the validation of the developed model.

2.5.1 The Reynolds equation for the cylinder block valve plate interface

The two main equations from which the Reynolds equation is derived are the Navier-Stokes and the continuity equation. The Navier-Stokes equation allows the fluid velocity to be defined in the clearance. This expression is then fed into the continuity equation which, integrated over the film thickness, yields to the Reynolds equation.

The previous works which attempted to determine the pressure field through the solution of the Reynolds equation either analytically (see Manring, 2000; Ivantysyn and Ivantysynova, 2001; Bergada et al., 2012) or numerically (see Wieczorek and Ivantysynova, 2002; Huang and Ivantysynova, 2003; Jouini and Ivantysynova, 2008; Ivantysynova and Baker, 2009) started from simplified forms of the equation, which did not allow all the possible alteration of the boundary surfaces to be captured. In this work a general form of the Reynolds equation was derived for the cylinder block / valve plate interface, accounting for arbitrary shape of both the surfaces defining the clearance and for the fluid properties to change across the film. Only in this way the described physical phenomena can be accounted in the proper way in the solution of the fluid flow. The derivation is documented in Appendix A; the final form of the Reynolds equation, A.13, is the following

$$\frac{1}{r}\frac{\partial}{\partial r}\left(-\frac{\rho h^3}{12\mu}r\frac{\partial p}{\partial r}\right)+\frac{1}{r}\frac{\partial}{\partial \vartheta}\left(-\frac{\rho h^3}{12\mu}\frac{1}{r}\frac{\partial p}{\partial \vartheta}\right)=\omega\left(\rho\frac{\partial h_{CB}}{\partial \theta}-\frac{1}{2}\frac{\partial\left(\rho h\right)}{\partial \theta}\right)-\rho\frac{\partial h}{\partial t} \quad (2.28)$$

The two terms on the left hand side model the hydrostatic pressure component through the diffusion of pressure from the boundaries of the fluid film; the diffusive coefficient is proportional to the ratio between of the cube of the fluid film thickness and the kinematic viscosity. The terms on the right hand side is the source in the Reynolds equation and they include the physical wedge, the translational squeeze and the normal squeeze component respectively.

To solve this equation the film thickness is described by two variables: h and h_{CB}, where $h = h_{CB} - h_{VP}$ is the algebraic difference between the cylinder block surface

position and valve plate surface position, being $z = 0$ the reference plane that defines the sign, as illustrated in Fig. 2.16.

2.6 The energy equation

The energy equation determines the temperature distribution in the lubricant and it is therefore fundamental to estimate the fluid properties and also the amount of heat that is dissipated from the fluid flow towards the solid parts.

For a steady-state fluid flow, the energy equation can be expressed in differential form as indicated in Eq. 2.29 (see Incropera et al. (2007)).

$$\boldsymbol{\nabla} \cdot \left(\rho \boldsymbol{V} T - \frac{\lambda}{c_p} \boldsymbol{\nabla} T \right) = \frac{\mu}{c_p} \Phi_d \tag{2.29}$$

Equation 2.29 has the typical form of the transport equation of a scalar, where the temperature in the lubricant is transferred through convection and diffusion processes. Moreover, in Eq. 2.29 there is also a source term, represented by the mechanical dissipation function Φ_d, expressing the heat power per unit volume generated by the viscous shear of the fluid trapped in the interface. The mechanical dissipation is derived from the assumption that the work needed to change the fluid element shape at constant volume is all irreversibly converted into heat. More precisely, the dissipation function is defined as the double inner product between the deviatoric stress tensor $\boldsymbol{\tau}$ and the gradient of the fluid velocity, as indicated in Eq. 2.30.

$$\Phi_d = \boldsymbol{\tau} : \boldsymbol{\nabla} \boldsymbol{V} \tag{2.30}$$

For a Newtonian fluid, in a cylindrical reference system, the dissipation function is defined by Eq. 2.31, as reported for example in Winter et al. (1980).

$$\begin{aligned} \Phi_d =& 2\mu \left[\left(\frac{\partial u}{\partial r} \right)^2 + \left(\frac{1}{r} \frac{\partial v}{\partial \vartheta} + \frac{u}{r} \right)^2 + \left(\frac{\partial w}{\partial z} \right)^2 + \right. \\ & \left. - \frac{1}{3} \left(\frac{1}{r} \frac{\partial (ru)}{\partial r} + \frac{1}{r} \frac{\partial v}{\partial \vartheta} + \frac{\partial w}{\partial z} \right)^2 \right] + \mu \left[r \frac{\partial}{\partial r} \left(\frac{\partial v}{\partial r} \right) + \frac{1}{r} \frac{\partial u}{\partial \vartheta} \right]^2 + \\ & + \mu \left[\frac{1}{r} \frac{\partial w}{\partial \vartheta} + \frac{\partial v}{\partial z} \right]^2 + \mu \left[\frac{\partial u}{\partial z} + \frac{\partial w}{\partial r} \right]^2 \end{aligned} \tag{2.31}$$

In Eq. 2.31 u, v and w are respectively the radial, circumferential and axial components of the fluid velocity $\boldsymbol{V}$. Recalling the assumptions made in section 2.5.1, Eq. 2.31 can be simplified into Eq. 2.32

$$\Phi_d = \left(\frac{\partial u}{\partial z}\right)^2 + \left(\frac{\partial v}{\partial z}\right)^2 + \frac{4}{3}\left(\frac{u}{r}\right)^2 + \left(\frac{v}{r}\right)^2 \tag{2.32}$$

Besides a better estimation of the lubricant properties, the knowledge of the temperature distribution also allows the heat fluxes towards the solid parts to be calculated through the Fourier law, Eq. 2.33.

$$q = -\lambda \left(\frac{\partial T}{\partial z}\right)_{\text{wall}} \tag{2.33}$$

Using Eq. 2.33 as a boundary condition, an heat transfer problem can be solved to determine the temperature field inside the cylinder block and valve plate bodies.

2.7 Power losses

The dissipation function expresses the amount of power per unit volume that is dissipated into heat in the fluid flow; thus the integration of Eq. 2.32 throughout the volume $\mathscr{V}$ of the clearance determines the total power that is dissipated in the fluid film

$$P_l = \int_{\mathscr{V}} \phi_d dv \tag{2.34}$$

It is important to underline that Eq. 2.34 includes also the power loss due to the leakage flow. In fact, when the fluid leaks into the case through the sealing land its mechanical energy accumulated in form of pressure is dissipated into heat.

The leakage flow Q_{sB} is calculated by integrating the oil velocity field over the lateral boundaries of the sealing land. In the cylindrical reference system illustrated in Fig. 2.15, with the expression of the velocities of the boundary surfaces in Eq. A.12, the velocity field of the oil in the clearance is described by Eq. 2.35.

$$\begin{cases} u = \dfrac{1}{2\mu}\dfrac{\partial p}{\partial r}\left[z^2 - z\left(h_{CB} + h_{VP}\right) + h_{CB}h_{VP}\right] \\ v = \dfrac{1}{2\mu}\dfrac{\partial p}{\partial \vartheta}\left[z^2 - z\left(h_{CB} + h_{VP}\right) + h_{CB}h_{VP}\right] + \omega r\left(\dfrac{z - h_{VP}}{h}\right) \end{cases} \tag{2.35}$$

In Eq. 2.35 u and v are respectively the radial and circumferential components of the velocity. In the case of the cylinder block / valve plate interface only the radial component of the oil velocity u (determined by the Poiseuille effect) contributes significantly to the leakage. The circumferential component v (due to the combined effect of Poiseuille and Couette effects) can eventually generate just cross port leakage, namely a minor flow of lubricant that leaks from the high to the low pressure ports. The power loss related to the leakage flow can calculated by multiplying the total leakage flow with the differential pressure Δp, as shown in Eq. 2.36.

$$P_{ls} = Q_{sB} \Delta p \tag{2.36}$$

The mechanical loss that is not related to leakage can be calculated as the difference of the total loss, Eq. 2.34 and the leakage loss, Eq. 2.36.

3. THE FLUID STRUCTURE INTERACTION AND THERMAL MODEL

In this chapter the fluid structure interaction and thermal model that has been developed in this work is described under two points of view. The first section describes how the physical phenomena introduced in section 2.3 are modeled and coupled together in the multi-domain simulation model. The second section is more technical and is focused on the workflow followed by the simulation model. All the details concerning the solution of the different problems introduced in this chapter are thoroughly explained in the next chapters. In particular the solution of the fluid flow and the fluid structure interaction are explained in chapter 4. The solution of the thermal problem through the finite element method is presented in chapter 5. The calculation of the thermal deflections and the elastic deformations due to pressure loads are covered in chapter 6.

3.1 Model overview

Figure 3.1 depicts an overview of the fluid structure interaction and thermal model of the cylinder block / valve plate interface that was developed in this work. Different problems are solved in the fluid and structure domains and the solutions are then coupled together thorough the definition of the common interface between them. In order to capture all the main physical phenomena affecting the lubricating interface performance, four modules were specifically developed.

The fluid flow module solves for the non-isothermal fluid flow in the interface through the finite volume method: Reynolds and Energy equations are solved in sequence and the main lubricant properties are updated accounting for the calculated pressure and temperature fields. In addition, the fluid flow module solves for the rigid

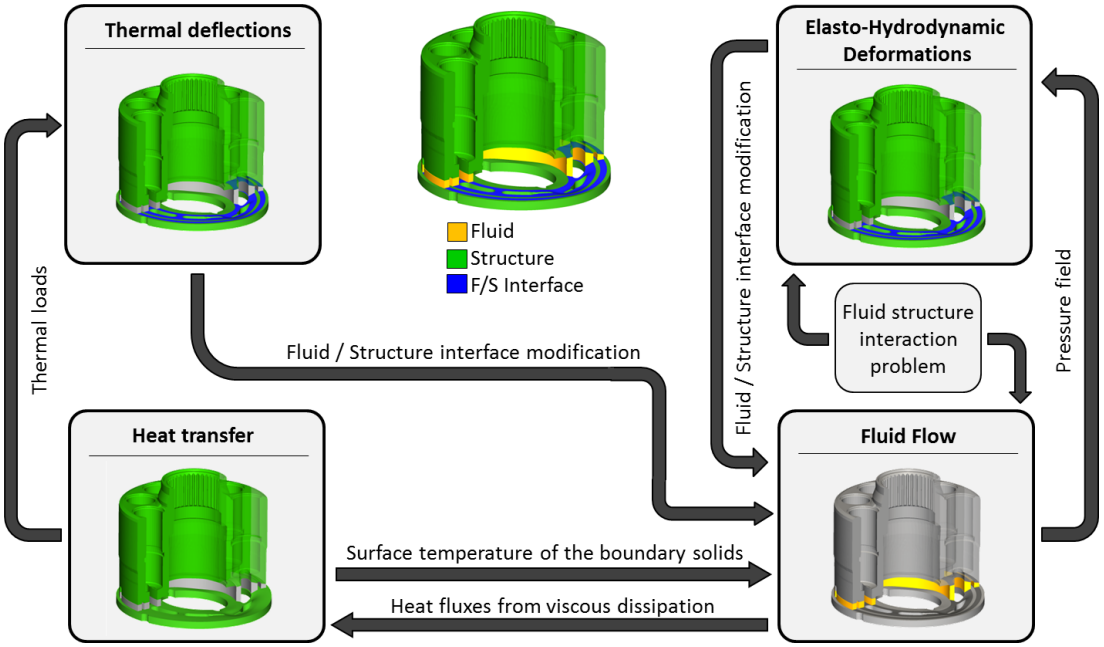

Fig. 3.1. Overview of the fluid structure interaction and thermal model of the cylinder block / valve plate interface.

body dynamic of the cylinder block body: the micro-motion of the cylinder block is iteratively changed until the resulting squeeze field in Eq. A.13 generates a pressure fields which balances the external loads expressed by Eq. 2.21. This approach was successfully applied to the cylinder block / valve plate interface by Wieczorek and Ivantysynova (2002) and the details can be found in the related publication.

Once the pressure field in the clearance is determined, the information is used to calculate the elastic deformation of both the solid parts, through the minimum potential energy formulation of the finite element method. The modification of the common interface between fluid and structure (represented in blue in Fig. 3.1) is fed back to the fluid flow module to update the prediction of the film thickness.

The fluid-structure interaction problem associated with the condition of elasto-hydrodynamic lubrication is solved through a so called partitioned approach (see Küttler and Wall, 2008), where the problems in the fluid and structure domains are

solved separately with dedicated solvers and then the solutions are coupled through an under-relaxed iterative algorithm.

On the other hand, the heat fluxes towards the cylinder block and valve plate bodies can be calculated when the temperature field in the lubricant is known, by means of Eq. 2.33. The heat transfer module uses these heat fluxes as boundary condition to solve for the temperature field in the solid parts. The governing equation is the steady-state, conductive form of the energy equation which is solved through the Galerkin formulation of the finite elements method. The calculated temperature fields in the solid bodies are used for two purposes. First, for both the solid parts temperature of the sealing surface is used to improve the boundary condition used to solve for the Energy equation in the fluid film; second, the internal temperature allows the thermal loads on the structure to be calculated. A finite element problem very similar to the one which governs the elastic deformation due to pressure can be defined using the thermal loads and the temperature-induced strain are thereby determined.

Usually the overall thermal deflections have an order of magnitude of several tens of microns, but just the relative changes in the sealing surfaces affect the common fluid/structure interface. These relative deformations are extracted and fed back to the fluid flow module for a further correction of the clearance geometry. The described thermal analysis is carried out just at the end of each revolution.

3.2 Model's workflow

The main purpose of the model proposed and analyzed in this work is to determine the film thickness between cylinder block and valve plate under steady state conditions. Due to the oscillating nature of the external loads (presented in section 2.2) the film thickness changes continuously over time; however, under steady state conditions, the film thickness will be a periodic function of time, repeating itself every shaft revolution.

The simulation model starts with a guessed lubricating film geometry and it goes through an iterative process where the film thickness is constantly corrected to meet the external load condition. The process ends when the predicted film thickness is periodic over one shaft revolution; in this condition the pressure field in the lubricant will be periodic as well and the temperature of the solid parts reaches a converged solution that does not change over time. Depending on the operating condition being simulated, usually about 5-10 simulated shaft revolutions are needed to reached the described situation.

Figure 3.2 illustrates the workflow of the process through a block diagram. Each revolution is discretized in time using a fixed step, which usually corresponds to the time required to rotate the shaft of one degree. At every time step the the Reynolds equation is solved using the current prediction of the film thickness and the pressure loads on the cylinder block (calculated with Eq. 2.18 or 2.20), are compared to the external loads (calculated with Eq. 2.21). At the first try there is always a loads imbalance (expressed by δF in Fig. 3.2) and the pressure field has to be adjusted in order to ensure the loads balance. This is done iteratively through a multidimensional root finding algorithm based on the Powell hybrid method (see Powell, 1970), which automatically changes the squeeze field $\partial \boldsymbol{h}/\partial t$ in the Reynolds equation until the force imbalance function is close to zero (usually 1N or less is used as tolerance threshold).

The fluid structure interaction problem is solved after the force balance loop. The solution approach is based on the non linear formulation of the Reynolds equation, in the sense that the the film thickness and the source in Eq. A.13 are considered a function of the pressure field. At every iteration in the non linear solution loop of the Reynolds equation, the elastic deformation of the solid parts are calculated with the current pressure solution and the film thickness is then corrected accordingly. In order to avoid divergence of the solution, the pressure field is under relaxed with a dynamic relaxation technique, in order to maximize the convergence speed. The convergence of the fluid structure interaction problem is measured through the normalized pressure residual: when the pressure has converged also the deformation fields $\delta \boldsymbol{h}^p_{CB}$ and $\delta \boldsymbol{h}^p_{VP}$

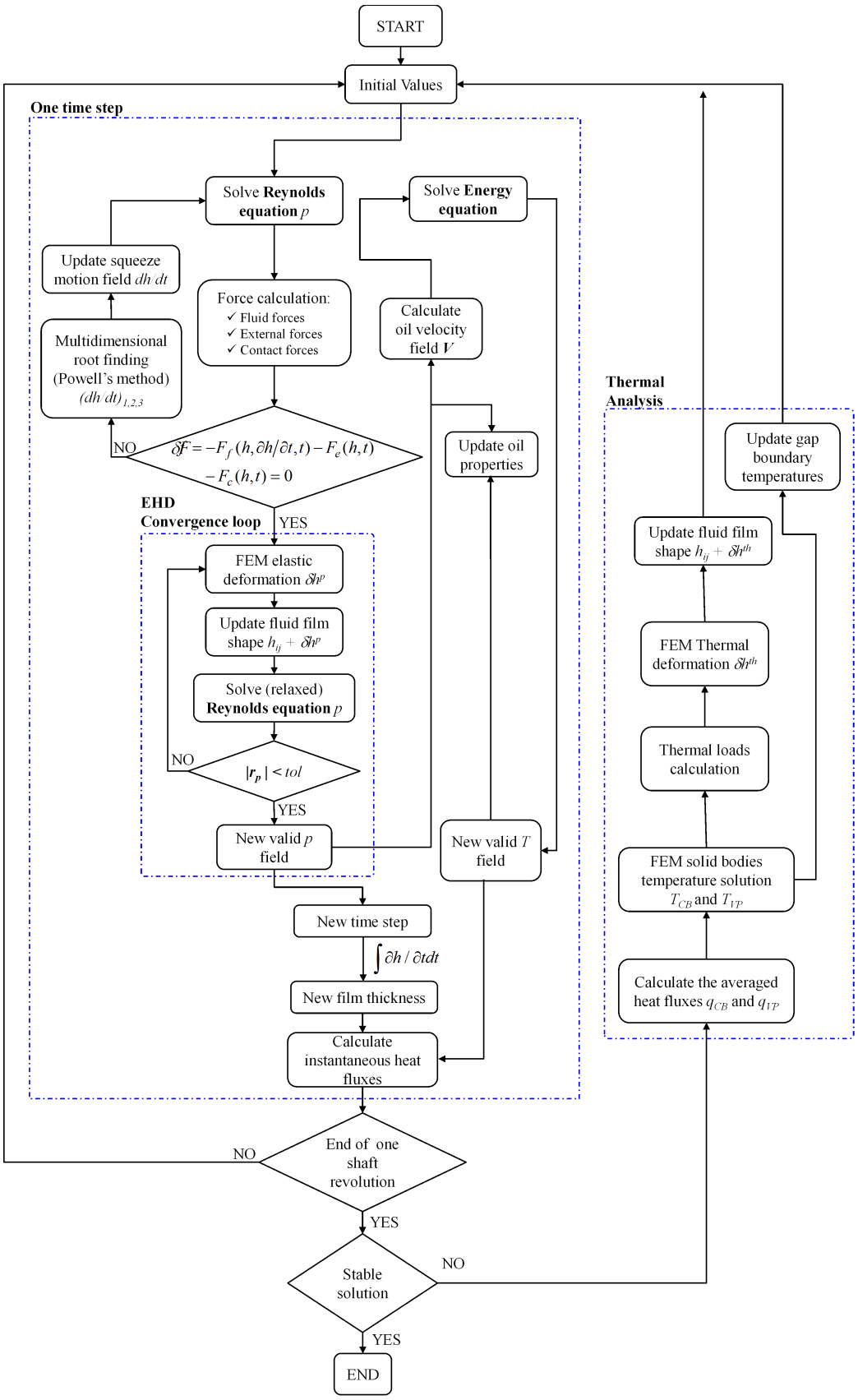

Fig. 3.2. Workflow of the simulation model for the cylinder block and valve plate interface

are assumed be converged, since they are directly associated with the pressure (the detailed description of this process is given in section 4.2)

At the end of the fluid structure interaction the pressure field will no longer balance exactly the external loads. Theoretically, the fluid structure interaction loop should be carried out at every iteration of the force balance loop; only in this way the final pressure field will meet the external load condition and it will be congruent with the deformation of the solid parts. However such kind of approach is not feasible because the simulation time increases exponentially, especially under low film thickness conditions. On the other hand, if the time step is reasonably small, the change in load condition from one time step to the other is small and the error introduced at the end of the fluid structure interaction loop should be rather small.

When a valid pressure field is determined the fluid velocity field is derived through Eq. A.5 and the Energy equation can be solved. The fluid properties are updated with the current pressure and temperature field and also the instantaneous heat fluxes to the solid parts are calculated through Eq. 2.33. The simulation process moves then to the next time step $k+1$; the current prediction of the film thickness is corrected by integrating in time the squeeze motion field as follows:

$$h^{(k+1)} = h^{(k)} + \int_{t=t^k}^{t=t^{k+1}} \frac{\partial h^{(k)}}{\partial t} d\tau \tag{3.1}$$

At the end of each revolution the thermal analysis is performed. The instantaneous heat fluxes towards the solid parts are averaged over one shaft revolution and applied as a boundary condition to solve for the temperature fields in the cylinder block, valve plate and end case assembly (all the details are explained in chapter 5). The thermal deflection are then derived from the thermal loads affecting the solid parts; the relative deformation of the surfaces in contact with the fluid, δh_{CB}^{th} and δh_{VP}^{th}, are extracted and used to further correct the film thickness prediction (details are in chapter 6); the two corrections δh_{CB}^{th} and δh_{VP}^{th} are constant throughout one shaft revolution. After the solution of the temperature fields in the solid parts the interface's surface temperatures are updated in order to solve the Energy equation more

precisely. The thermal problem is the one that requires to simulate many revolutions to reach a converged solution. The simulation ends when the thermal corrections (in terms of film thickness and surfaces temperature) no longer change the film thickness prediction from one revolution to the other.

4. SOLUTION OF THE NON-ISOTHERMAL FLUID FLOW

The non-isothermal fluid flow in the clearance is governed by the Reynolds and the Energy equation introduced in sections 2.5.1 and 2.6. This chapter explains in detail how these partial differential equations are solved in the simulation model, describing the computational grid generation, the discretization process and the solution scheme.

4.1 Grid features and generation

The cylinder block valve plate interface is characterized by a complex geometry due to the complex shape of the kidney and ports openings; moreover the computational domain changes continuously over one shaft revolution due to the relative motion of the cylinder block with respect to the valve plate. At a first glance, it would seem that an unstructured, non orthogonal grid is the best way of discretizing the clearance geometry, because in that way the complex shape would be described almost exactly. This is not just a nice property but also an important practical requirement for the model: the prediction of the lubricating interface performance is based upon the balance of the external forces acting on the cylinder block with the pressure field in the lubricant and therefore, if the sealing land area is poorly approximated, the film thickness prediction will be significantly affected by the error. Suppose that the area error in the sealing land discretization respect the exact shape is 5%. The axial force that the pressure in the gap has to generate is in the order of magnitude of tens of kN, therefore that little error in the discretization would lead to an error of $500 \div 1000$ N , which is close to the typical values of the spring force F_S illustrated in Fig. 2.5.

Nevertheless, precision is not the only requirement that the fluid grid has to fulfill. The way in which finite volume method is formulated makes it intrinsically more

effective on orthogonal grids, i.e. grids where the vectors connecting the elements centroid are orthogonal to the common face shared by the elements. If that is not the case (namely for non-orthogonal girds) the calculation of the gradient becomes problematic and the finite volume approach forces linear problem to become non-linear due to the introduction of the so called secondary gradient or non-orthogonal correction (see Jasak, 1996; Murthy, 2002). When a problem becomes non-linear a certain number of so called outer iterations are required to progressively improve the terms that depend on the solution and this slows down the overall solution process. Furthermore, an unstructured, non-orthogonal mesh would also make difficult to handle the mesh motion because it would require to re-generate a new mesh at each time step in the simulation to account for the changing in relative position between cylinder block and valve plate.

For this reasons in this work the choice leaned towards a structured, orthogonal grid for the solution of the fluid flow, represented in Fig. 4.1. Elements are organized in planar layers, composed of m rings of size n; the total number of layers is q. Each direction is identified by a counter i, j, k for the radial, circumferential and axial directions respectively. The grid shown in Fig. 4.1 is tridimensional and is used to

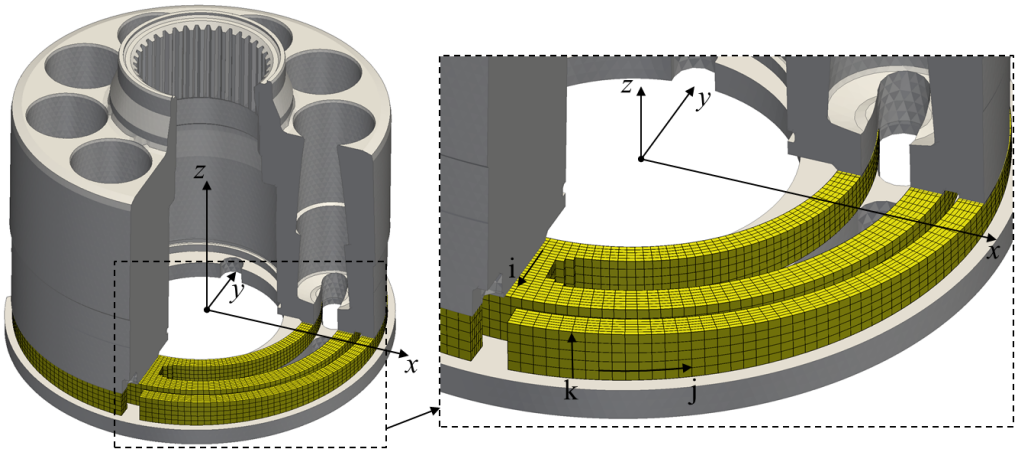

Fig. 4.1. Structured grid used to solve for the fluid flow.

solve for the Energy equation; the Reynolds equation is defined on a bi-dimensional domain and therefore just one layer of the grid is used for its solution.

The grid is automatically generated in the model. The grid generation algorithm starts creating two discs of elements of size mn, where the inner and outer diameters of the discs are the same of the inner and outer diameters of the actual sealing surface; moreover elements are organized in radials groups, in order to fit precisely the kidney openings and, if present, the outer hydrodynamic bearing.

In a second step the elements are divided into fluid and boundary types as illustrated in Fig. 4.2. The blue lines defining the cylinder block openings, outer bearing and valve plate ports are automatically generated in the model, from the CAD definition of the cylinder block and valve plate body (in `stl` format). The winding number algorithm (see Press et al., 2007) is used to identify whether or not a element centroid lies inside the fluid region. Every non-fluid region is properly labeled, to keep information about the associated boundary to be applied for the solution of the partial differential equations: every group of elements belonging to each cylinder block kidney opening are labeled from 1 to the number of pistons z in the machine, the groups of elements in the valve plate ports are divided into "high pressure port" elements (by default on the positive x direction in Fig. 4.2) and into "low pressure port", also the group of elements in the "case pressure" regions are properly labeled. The two grids represented in Fig. 4.2 are stored in the model so that for any shaft angular position the actual fluid region is obtained by superimposing the cylinder block's grid (properly rotated) to the valve plate grid (fixed): if two fluid elements are superimposed the results will be a fluid element, if at least one of the two elements is instead part of a boundary, the resulting element will be a boundary. This approach makes the mesh motion handling very simple and effective. The three dimensional grid represented in Fig. 4.1 is obtained just repeating in axial direction the two dimensional mesh of Fig. 4.2.

Looking at the zoomed regions in Fig. 4.2 it is evident that the complex shapes of the real geometries are not perfectly approximated by the grids. In order to make

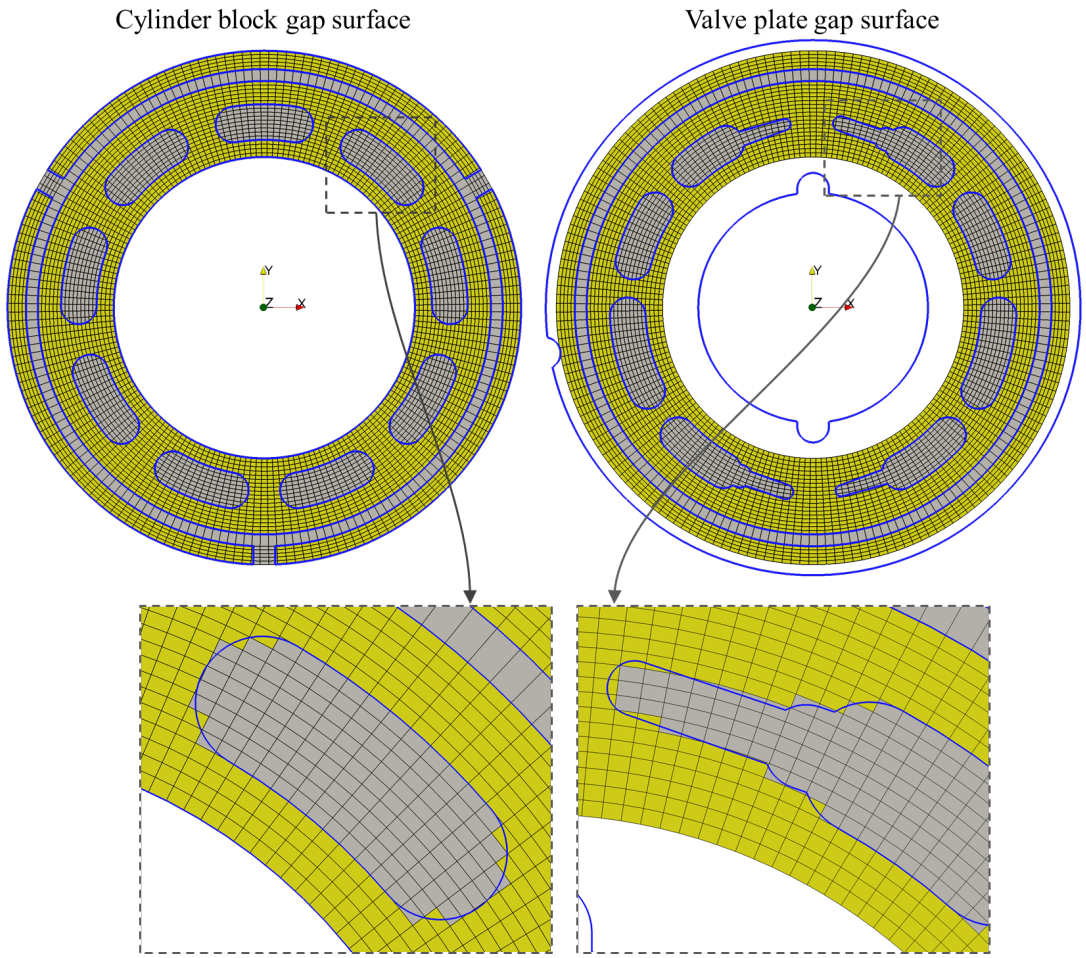

Fig. 4.2. Grids generation for cylinder block and valve plate surfaces. The yellow elements represent fluid and the grey elements are part of openings, ports, or grooves. The blue boundary lines define the actual shape of the cylinder block and valve plate sealing surfaces.

the picture clear the number of gird elements is remarkably lower compared to the actual number used for practical calculation (usual sizes are $m \times n \times q = 60 \times 360 \times 30$ for normal grids and $m \times n \times q = 120 \times 720 \times 60$ for fine grids), however even with finer grids the problem remains. This accuracy issue was solved by introducing an additional grid, that matches exactly the shape of the cylinder block's sealing land as illustrated in Fig. 4.3. On this additional grid no equation is solved: the pressure field is simply interpolated for the only purpose of pressure loads calculation. The additional grid is automatically generated in the model as well. The original quads

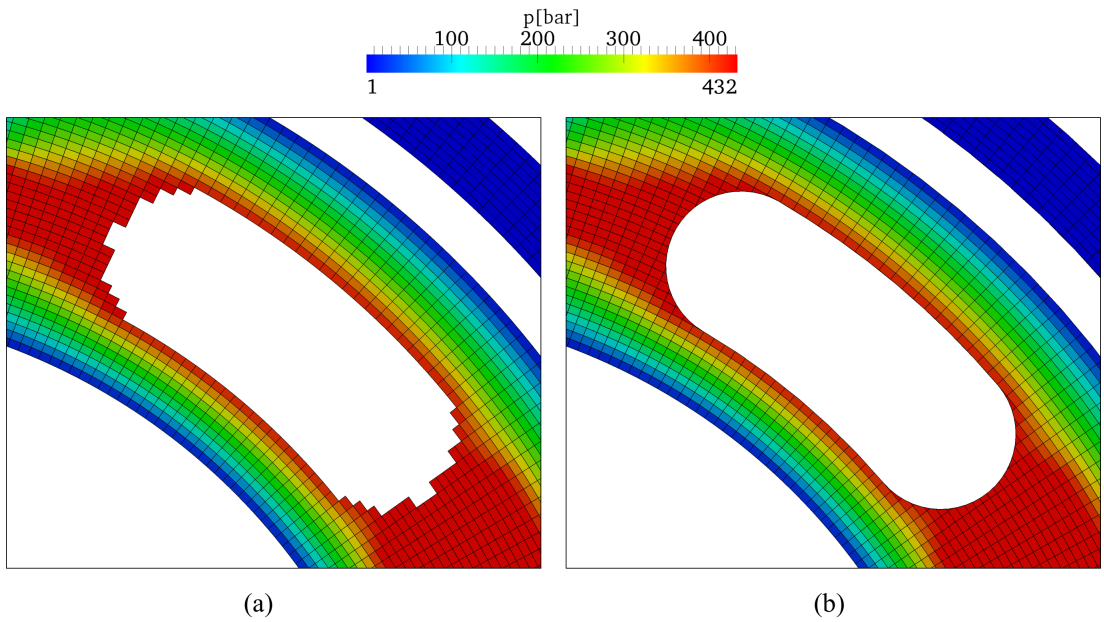

Fig. 4.3. (a) pressure field calculated through the solution of the Reynolds equation on a computation grid of 60 × 360 elements; (b) pressure field interpolated from (a) on the grid used for the calculation of the pressure loads on the cylinder block.

elements are clipped with the blue boundary lines of Fig. 4.2 using the algorithm described by Vatti (1992).

4.1.1 Discretization of the Reynolds equation

The Reynolds equation is a partial differential equation describing a diffusion process in two dimensions and it can be represented in compact form like in Eq. 4.1.

$$\boldsymbol{\nabla} \cdot (-\Gamma \boldsymbol{\nabla} p) = S \tag{4.1}$$

By comparing Eq. 4.5 with Eq. A.13, the diffusive coefficient λ is defined as

$$\Gamma = \frac{\rho h^3}{12\mu} \tag{4.2}$$

and the source term as

$$S = \omega \left(\rho \frac{\partial h_{CB}}{\partial \theta} - \frac{1}{2} \frac{\partial (\rho h)}{\partial \theta} \right) - \rho \frac{\partial h}{\partial t} \tag{4.3}$$

The integration of Eq. 4.1 over the control volume $\delta\mathscr{V}$ shown in Fig. 4.4 yields to Eq. 4.4.

$$\int_{\delta\mathscr{V}} \boldsymbol{\nabla} \cdot (-\Gamma \boldsymbol{\nabla} p)\, dv = \int_{\delta\mathscr{V}} S dv \tag{4.4}$$

Applying the divergence theorem Eq. 4.4 becomes

$$\int_{\delta\mathscr{A}} -\Gamma \boldsymbol{\nabla} p \cdot d\boldsymbol{a} = \int_{\delta\mathscr{V}} S dv \tag{4.5}$$

In Eq. 4.5 the integral of the left hand side is over the boundary surface $\delta\mathscr{A}$ of the control volume. Without any approximation, the integral on the left hand side can be substituted by the summation over the four faces w, e, s and n of the control volume represented in Fig. 4.4, as indicated in Eq. 4.5.

$$\sum_{i=1}^{4} -\Gamma_i \boldsymbol{\nabla} p_i \cdot \delta\mathscr{A}_i \boldsymbol{n} = \int_{\delta\mathscr{V}} S dv \tag{4.6}$$

The selection of an orthogonal mesh makes the calculation of the dot product in

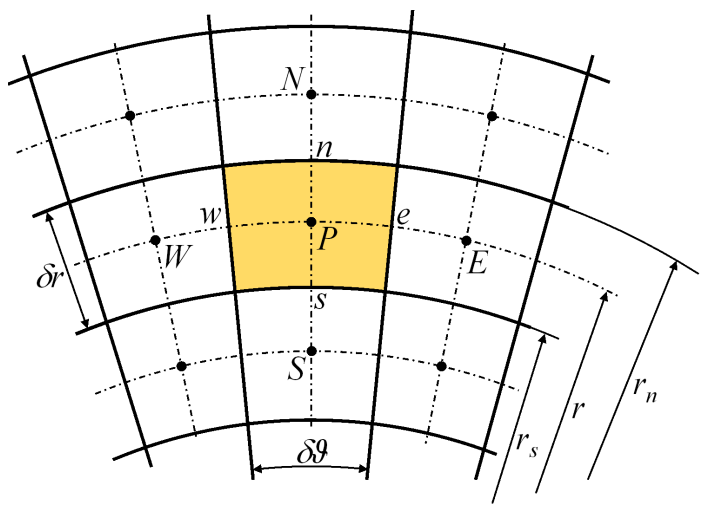

Fig. 4.4. Detail of the control volume used to discretize the Reynolds equation in cylindrical coordinates.

Eq. 4.6 easy, since the directions of the gradient's components are always normal to

the boundary faces of the control volume. Thus, Eq. 4.6 simplifies into the following equation.

$$\sum_{i=1}^{4} -\Gamma_i \nabla p_i \cdot \delta \mathscr{A}_i = \int_{\delta \mathscr{V}} S dv \tag{4.7}$$

Eq. 4.7 can be rewritten as in Eq. 4.8:

$$\frac{\rho_w h_w^3}{12\mu_w}\delta r \left(\frac{\partial p}{\partial \vartheta}\right)_w - \frac{\rho_e h_e^3}{12\mu_e}\delta r \left(\frac{\partial p}{\partial \vartheta}\right)_e + \frac{\rho_s h_s^3}{12\mu_s} r_s \delta\vartheta \left(\frac{\partial p}{\partial r}\right)_s + \\ - \frac{\rho_n h_n^3}{12\mu_n} r_n \delta\vartheta \left(\frac{\partial p}{\partial r}\right)_n = \int_{\delta \mathscr{V}} S dv \tag{4.8}$$

At this point the calculation of the gradients at the control volume's faces requires an approximation, because it needs to be derived just from the information of pressure at the cells centroid (labeled with capital letters in Fig. 4.4). Using the central difference scheme (CDS) Eq. 4.8 is modified as follow.

$$\frac{\rho_w h_w^3}{12\mu_w}\delta r \left(\frac{p_P - p_W}{r\delta\vartheta}\right) - \frac{\rho_e h_e^3}{12\mu_e}\delta r \left(\frac{p_E - p_P}{r\delta\vartheta}\right) + \frac{\rho_s h_s^3}{12\mu_s} r_s \delta\vartheta \left(\frac{p_P - p_S}{\delta r}\right) + \\ - \frac{\rho_n h_n^3}{12\mu_n} r_n \delta\vartheta \left(\frac{p_N - p_P}{\delta r}\right) = \int_{\delta \mathscr{V}} S dv \tag{4.9}$$

The source S is defined by Eq. 4.10.

$$S = \left[\omega \rho_P \left(\frac{h_{CB,E} - h_{CB,W}}{2\delta\vartheta} - \frac{1}{2}\frac{h_E - h_W}{2\delta\vartheta}\right) - \rho_P \frac{\partial h_P}{\partial t}\right] \tag{4.10}$$

The last term in Eq. 4.10, $\partial h_P / \partial t$, includes the squeeze introduced by the rigid motion of the cylinder block and the rate of change of fluid film due to the elasto-hydrodynamic deformation, as indicated in Eq. 2.26; this term is discretized with backward difference in time as follows.

$$\frac{\partial h_P}{\partial t} \approx \left[\frac{1}{\sqrt{3}R_B} r_P \sin\vartheta_P (\dot{h}_{P_2} + \dot{h}_{P_2}) + \frac{1}{3R_B} r_P \cos\vartheta_P (2\dot{h}_{P_1} - \dot{h}_{P_2} - \dot{h}_{P_3}) + \right. \\ \left. + \frac{1}{3}(\dot{h}_{P_1} + \dot{h}_{P_2} + \dot{h}_{P_3})\right] + \left[\frac{\delta h_{CB}^{t_i} - \delta h_{CB}^{t_{i-1}}}{\delta t} - \frac{\delta h_{VP}^{t_i} - \delta h_{VP}^{t_{i-1}}}{\delta t}\right] \tag{4.11}$$

The terms δh_{CB} and δh_{VP} in Eq. 4.11 are the elastic deformations of the cylinder block and valve plate.

Since the film thickness is a function of the pressure field by means of the bodies deformations, the source S depends on the solution variable p. In this case, as suggested by Patankar (1980), the source can be linearized into a constant part S_c and a variable part S_p that depends on the pressure, as in Eq. 4.12.

$$\int_{\delta\mathscr{V}} S dv \approx (S_c + S_P p_P)\, \delta\mathscr{V} = (S_c + S_P p_P) \left[\frac{\delta\vartheta}{2} \left(r_n^2 - r_s^2 \right) \right] \tag{4.12}$$

There are many ways of splitting S into S_c and S_p. If the dependence $S(p)$ is known analytically, the best approach would be to embed the derivative dS/dp into S_p. Unfortunately in this case the relation $S(p)$ is very complex because it depends on the elastic deformation of the solid parts and it is certainly not possible to define it analytically; the derivative could be approximated numerically but the computation overhead would be too big. On the other hand, to radically simplify the problem, S_p could be set to zero, assuming the source to be totally independent upon the pressure, i.e. $S = S_c$; even though this approach simplifies the discretization it may create problems later, during the solution process. The approach that worked best for this problem defines S_p through a fixed parameter γ as indicated in Eq. 4.13.

$$\begin{cases} S_c = S + \gamma\, |S|\, p_p \\ S_p = -\gamma\, |S| \end{cases} \tag{4.13}$$

In this way, the bigger is the magnitude of S, the bigger is the amount that is supposed to change with the pressure. Moreover, the solution dependent portion of the source is forced to be always negative, to ensure the Scarborough criterion to be satisfied (see Scarborough, 1958). A good value of γ which works well for this problem was found to be 10^{-7}.

The algebraic equation resulting from the finite volume discretization is derived by rearranging Eq. 4.9 and 4.12.

$$a_P p_P = a_W p_W + a_E p_E + a_S p_S + a_N p_N + b \tag{4.14}$$

The definition of the algebraic coefficients depends upon the position of each control volume. For a cell in the interior of the grid, like the one shown in Fig. 4.4, the algebraic coefficients are defined as in Eq. 4.15.

$$
\begin{aligned}
&a_W = \frac{\delta r \rho_w h_w^3}{12 r \delta\vartheta \mu_w}, \;\; a_E = \frac{\delta r \rho_e h_e^3}{12 r \delta\vartheta \mu_e}, \;\; a_S = \frac{r_s \delta\vartheta \rho_s h_s^3}{12 \delta r \mu_s}, \;\; a_N = \frac{r_n \delta\vartheta \rho_n h_n^3}{12 \delta r \mu_n}; \\
&a_P = a_W + a_E + a_S + a_N - S_p \left[\frac{\delta\vartheta}{2} \left(r_n^2 - r_s^2 \right) \right]; \\
&b = S_c \left[\frac{\delta\vartheta}{2} \left(r_n^2 - r_s^2 \right) \right] p_P + \frac{1-\alpha}{\alpha} a_P p_P
\end{aligned}
\tag{4.15}
$$

The additional term $a_P p_P (1-\alpha)/\alpha$ in Eq. 4.15 derives from the relaxation technique used in the iterative solution algorithm in the fluid structure interaction, see section 4.2

4.1.2 Boundary conditions

The solution of the Reynolds equation represents a full Dirichlet problem, where the pressure needs to be specified on all the boundaries. Fig. 4.5 illustrates the pressure values applied to the different boundaries.

Each displacement chamber region is set to the associated instantaneous pressure, even when the displacement chamber is superimposed to the valve plate ports. The valve plate ports regions are set to the high or low pressure values (red and blue line respectively in Fig. 4.5) related to the current shaft angle φ; the case region is set to the pressure value in the pump casing.

For what concerns the discretization process, if one or more faces of the control volume P is represented by a boundary, the definition of the algebraic coefficients changes respect Eq. 4.15. For example, if the control volume is surrounded by the

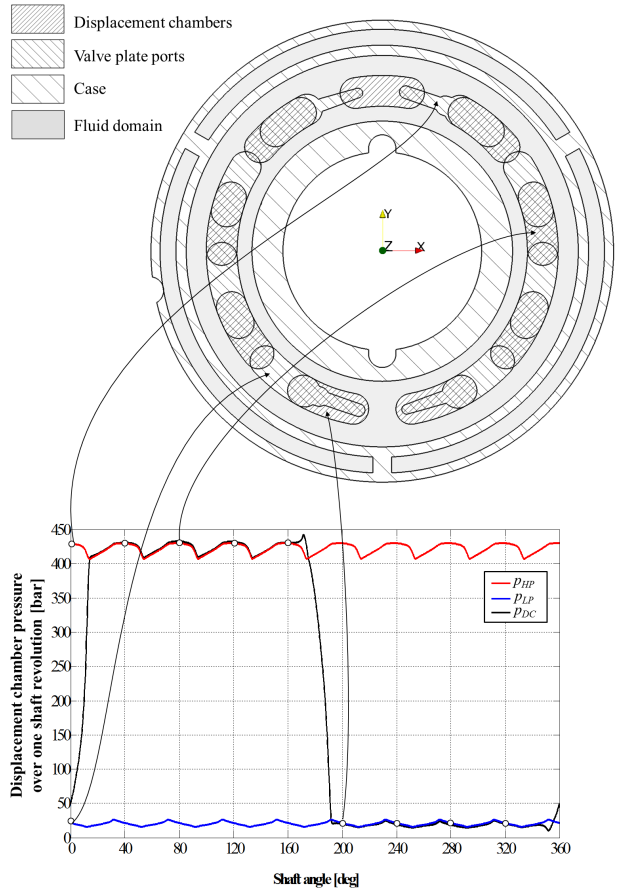

Fig. 4.5. Boundary conditions applied to solve the Reynolds equations at shaft angle $\varphi = 0$.

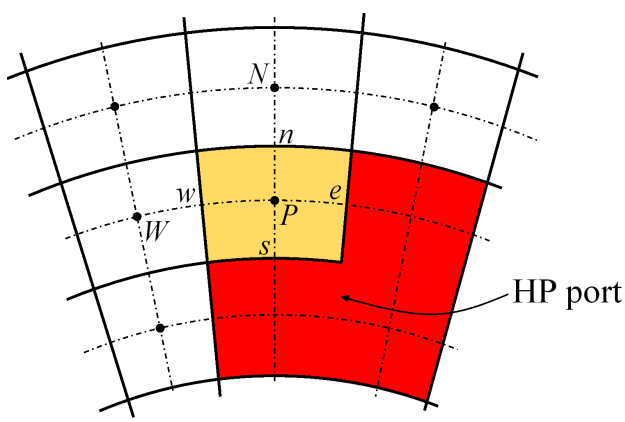

Fig. 4.6. Control volume surrounded by part of the high pressure port, where the pressure is imposed at the value p_{HP}.

high pressure port region, as illustrated in Fig. 4.6, the coefficients definition changes as follows.

$$
\begin{aligned}
&a_W = \frac{\delta r \rho_w h_w^3}{12 r \delta\vartheta \mu_w}, \;\; a_E = 0, \;\; a_S = 0, \;\; a_N = \frac{r_n \delta\vartheta \rho_n h_n^3}{12 \delta r \mu_n}; \\
&a_P = a_W + \frac{2\delta r \rho_w h_w^3}{12 r \delta\vartheta \mu_w} + \frac{2 r_s \delta\vartheta \rho_n h_n^3}{12 \delta r \mu_n} + a_N - S_p \left[\frac{\delta\vartheta}{2} \left(r_n^2 - r_s^2 \right) \right]; \\
&b = S_c \left[\frac{\delta\vartheta}{2} \left(r_n^2 - r_s^2 \right) \right] p_P + p_{HP} \left(\frac{2\delta r \rho_w h_w^3}{12 r \delta\vartheta \mu_w} + \frac{2 r_s \delta\vartheta \rho_n h_n^3}{12 \delta r \mu_n} \right) + \frac{1-\alpha}{\alpha} a_P p_P
\end{aligned}
\tag{4.16}
$$

4.2 Solution of the Reynolds equation and the fluid structure interaction problem

The elastic deformations of the solid parts make the Reynolds equation non linear because both the algebraic coefficients and the source term in Eq. 4.14 are function of the solution $\boldsymbol{p}$. The solution scheme in this situation is an iterative procedure, which starts with an initial guess of pressure $\boldsymbol{p}^{(0)}$ (usually the guesses comes from the solution of the fluid flow from the previous time step) and goes through a series of outer iterations as follows:

1. With the current approximation of pressure field at the iteration (k), $\boldsymbol{p}^{(k)}$, the elastic deformations of the solid parts due to pressure loads, $\delta \boldsymbol{h}_{CB}^{p}{}^{(k)}$ and $\delta \boldsymbol{h}_{VP}^{p}{}^{(k)}$ are calculated. The deformations elastic deformations are used to update the film thickness, through Eq. 2.25 and to update the EHD squeeze term as indicated in Eq. 4.11; it is important to underline that for the stability of the solution process the EHD squeeze is dynamically changed at each iteration. The viscosity field is updated using the current predictions of fluid pressure and temperature.

2. With the current approximation of the film thickness, $\boldsymbol{h}^{(k)}$, and viscosity, $\boldsymbol{\mu}^{(k)}$, the Reynolds equation can be discretized as described in the previous section;

3. By combining the algebraic Eq. 4.14 for all the control volumes in the computational domain, a linear system of the form of Eq. 4.17 is obtained.

$$\mathbf{A}^{(k)}\boldsymbol{p}^{(k+1)} = \boldsymbol{b}^{(k)} \tag{4.17}$$

   In Eq. 4.17 $\boldsymbol{p}^{(k+1)}$ is the solution vector of pressure in the cells centroid resulting from the current approximation for the known vector $\boldsymbol{b}^{(k)}$ (composed of the sources, boundaries and non-linearity terms) and $\mathbf{A}^{(k)}$ is the sparse, non-symmetric matrix of algebraic coefficients. The solution of the linear system in Eq. 4.17 involves a certain number of inner iterations, indicated with (ν), which are performed by an iterative solver, described in the next section.

Since the dependence between pressure and film thickness can be quite strong, an under-relaxation techniques is used in combination with the source term linearization. The relaxation coefficient α, which shows up in the expression of the source term in Eq. 4.15 and 4.16, is dynamically changed as a function of the residual behavior during the solution process.

An important issue shared by all the iterative methods is the estimation of convergence during the process. Formally, is the exact solution $\boldsymbol{p}$ is known, at the iteration (k) the error at the step k, $\boldsymbol{e}^{(k)}$ is defined as the difference between the exact solution and the current best approximation $\boldsymbol{p}^{(k)}$:

$$\boldsymbol{e}^{(k)} = \boldsymbol{p} - \boldsymbol{p}^{(k)} \tag{4.18}$$

Unfortunately, since the exact solution is unknown the error is not a practical measure of convergence; nevertheless Eq. 4.17 can be rewritten in a different way:

$$\mathbf{A}\boldsymbol{p} - \mathbf{A}\boldsymbol{p}^{(k)} = \mathbf{A}\boldsymbol{e}^{(k)} = \boldsymbol{b}^{(k)} - \mathbf{A}\boldsymbol{p}^{(k)} = \boldsymbol{r}^{(k)} \tag{4.19}$$

In Eq. 4.19 $\boldsymbol{r}$ is called residual and it represents the error transformed by $\mathbf{A}$ in the same space of $\boldsymbol{b}$; the residual is used as a measure of the convergence process. In order to have a measure that is independent on the scale of the problem, the normalized

residual is introduced; in this work the residual was normalized using the known term $\boldsymbol{b}$, as indicated in Eq. 4.20.

$$r_n^{(k)} = \frac{\|r^{(k)}\|_2}{\|b^{(k)}\|_2} = \frac{\sqrt{\left(\sum_i r_i^{(k)}\right)^2}}{\sqrt{\sum \left(b_i^{(k)}\right)^2}} \tag{4.20}$$

Figure 4.7 illustrates a typical path followed by the normalized residual during the non linear solution process just described. It can be noticed that the residual

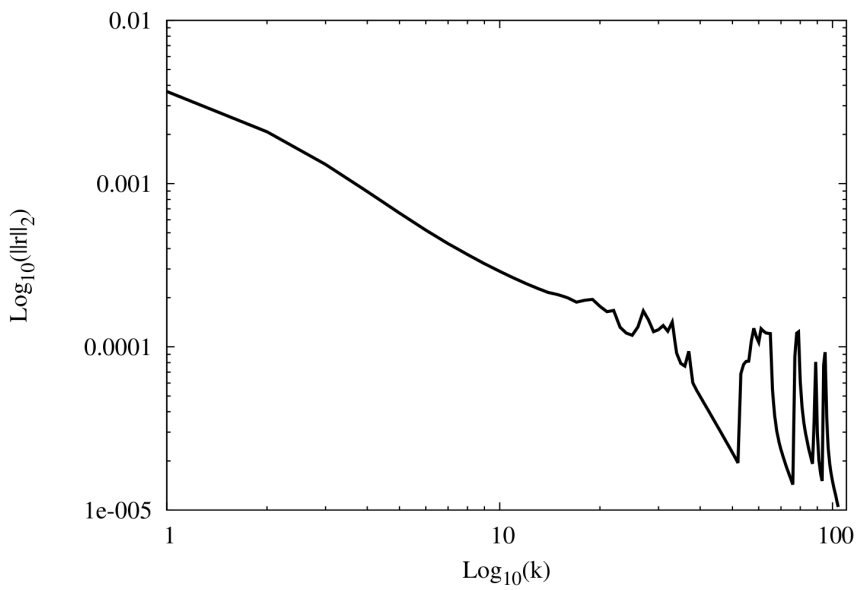

Fig. 4.7. Convergence behavior for the solution of the fluid structure interaction problem.

drop is quite smooth during the first phase but it becomes more bumpy when low residual values are reached; at about 60 iterations the solution starts to diverge with a relaxation factor of 0.8 and the dynamic relaxation algorithm decreases it to 0.6, to reach the 10^{-5} convergence tolerance. The lower relaxation is necessary because the minimum film thickness value for this example is close to one micron and the pressure-deformation interaction is definitely non negligible.

4.2.1 The Preconditioned bi-Conjugate Gradient stabilized method for the solution of sparse linear systems

As shown in Fig. 4.7, many outer iterations are necessary to solve the fluid structure interaction problem. Considering that at every iteration the linear system of Eq. 4.17 has to be solved and that the fluid structure interaction problem has to be faced at every time step in the overall solution loop it is clear that a very efficient linear solver is a must to conclude a simulation in a reasonable amount of time.

The pattern of the matrix **A**, determined by the discretization of the Reynolds equation on the grid of Fig. 4.3 is represented in Fig. 4.8. As anticipated, **A** is a

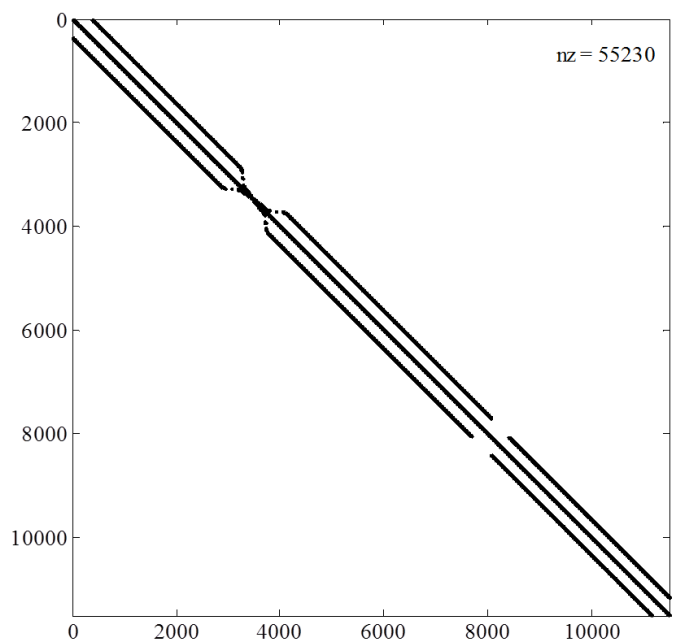

Fig. 4.8. Typical sparse pattern for the matrix **A** from the discretization of the Reynolds equation on the grid of Fig. 4.3.

sparse matrix and even though from Fig. 4.8 it looks symmetric, the values of the entries are different, due to the non uniform viscosity and film thickness.

The linear system of Eq. 4.17 can be solved with direct or iterative methods. Due to the properties of the matrix **A**, an iterative procedure was prefered: the

biconjugate gradient stabilized method (BiCGstab). The BiCGstab method belongs to the Krylov-types methods and is one of the most popular solvers in computational fluid dynamics. The performance of the solver depends on the condition number κ of the matrix $\mathbf{A}$, i.e. the ratio between the maximum and the minimum eigenvalue. In particular, it can be proven (see Shewchuk, 1994) that the maximum number of iterations required to reduce the initial error norm of a factor ϵ is:

$$\nu_{\max} \leq \sqrt{\kappa} \ln \left(\frac{2}{\epsilon} \right) \tag{4.21}$$

To overcome this limitation, in most of the applications the biconjugate gradient stabilized method is not applied directly to the linear system of Eq. 4.17, but rather to the following equivalent system:

$$\mathbf{M}^{-1}\mathbf{A}\boldsymbol{p} = \mathbf{M}^{-1}\boldsymbol{b} \tag{4.22}$$

The matrix $\mathbf{M}^{-1}\mathbf{A}$ should have a much smaller condition number and/or better clustered eigenvalues than the original matrix itself. A matrix $\mathbf{M}$ with this property is called preconditioner. Since using a preconditioner in an iterative method generates some extra cost, both initially for the setup and per iteration for its application, a trade-off can be found between these disadvantages and the gain in convergence speed. The concept of convergence speed in this context is not referred to the number of iteration required to reduce the error norm below a certain value, but rather to the time required by this process. It's clear that a preconditioner won't be attractive if it allows the problem to be solved in a few iterations but it requires an unreasonable amount of time to be constructed and applied. There are many possible types of preconditioners available, from very simple ones, like Jacobi or SSOR, to more advanced ones, as incomplete factorizations, polynomial preconditioners or preconditioners based on the properties of the differential equation to be solved.

In this work the incomplete *LU* factorization preconditioner was used. The incomplete factorization is an approximation of the matrix $\mathbf{A}$ given by the product $\mathbf{M} = \mathbf{LU}$ of a lower and upper triangular matrix respectively; the factorization is defined incomplete because in the construction of $\mathbf{L}$ and $\mathbf{U}$ the non-zero entries located

in positions where the matrix **A** is zero are either ignored or considered only if certain conditions are satisfied. In the first case, the factorization is called incomplete level-0 LU, or ILU(0). In the second case, elements outside of the non-zero pattern of **A** may be accepted if they lie within a certain fill-in level and drop tolerance (see Saad, 2003); this last type of factorization is called ILUT(k,δ). The ILUT(k,δ) is most of the time more effective than ILU(0) but it requires more time to be computed depending on which value of fill in and drop tolerance are selected.

Figure 4.9 shows a comparison of different solution methods in terms of iterations ν required to drop the normalized residual below a certain tolerance. The different solvers performance were compared on a 160×1440 elements grid, corresponding to about 140000 non zero entries in the matrix **A**. The film thickness and the resulting pressure field for the test case are illustrated in Fig. 4.9 as well: the high pressure region observed between point P_1 and P_2 is due to the combination of the diverging clearance and the cylinder block's circumferential velocity of 1000 rpm (clockwise).

The green line in Fig. 4.9 describes the Successive Over Relaxation (SOR) solver, with an over-relaxation factor of 1.8. That was the solver that has been used in all the previous works to integrate the Reynolds equation in the cylinder block / valve plate interface (see Wieczorek and Ivantysynova, 2002; Huang and Ivantysynova, 2003; Jouini and Ivantysynova, 2008; Ivantysynova and Baker, 2009). The other three dotted lines represent the performance of the BiCGstab solver with different types of preconditioners. The SOR solver takes slightly more than 1000 iterations to reach the normalized residual, while the BiCGstab is more effective even with a poor Jacobi preconditioner, converging in less than 400 iterations. Furthermore, as expected, using the ILUT(0) and ILUT(k,δ) preconditioners the BiCGstab performs much better, reaching the normalized residual in 113 and 63 iterations respectively.

Focusing on computation time, Table 4.1 reports an overview for different grid sizes. On the 1440×160 cells grid, the ratio between the number of iterations required by ILUT-BiCGstab and SOR is slightly the same of the ratio between the computation times ($63/1022 \approx 2203/36880 \approx 0.06$). In this case the iterations number reduction

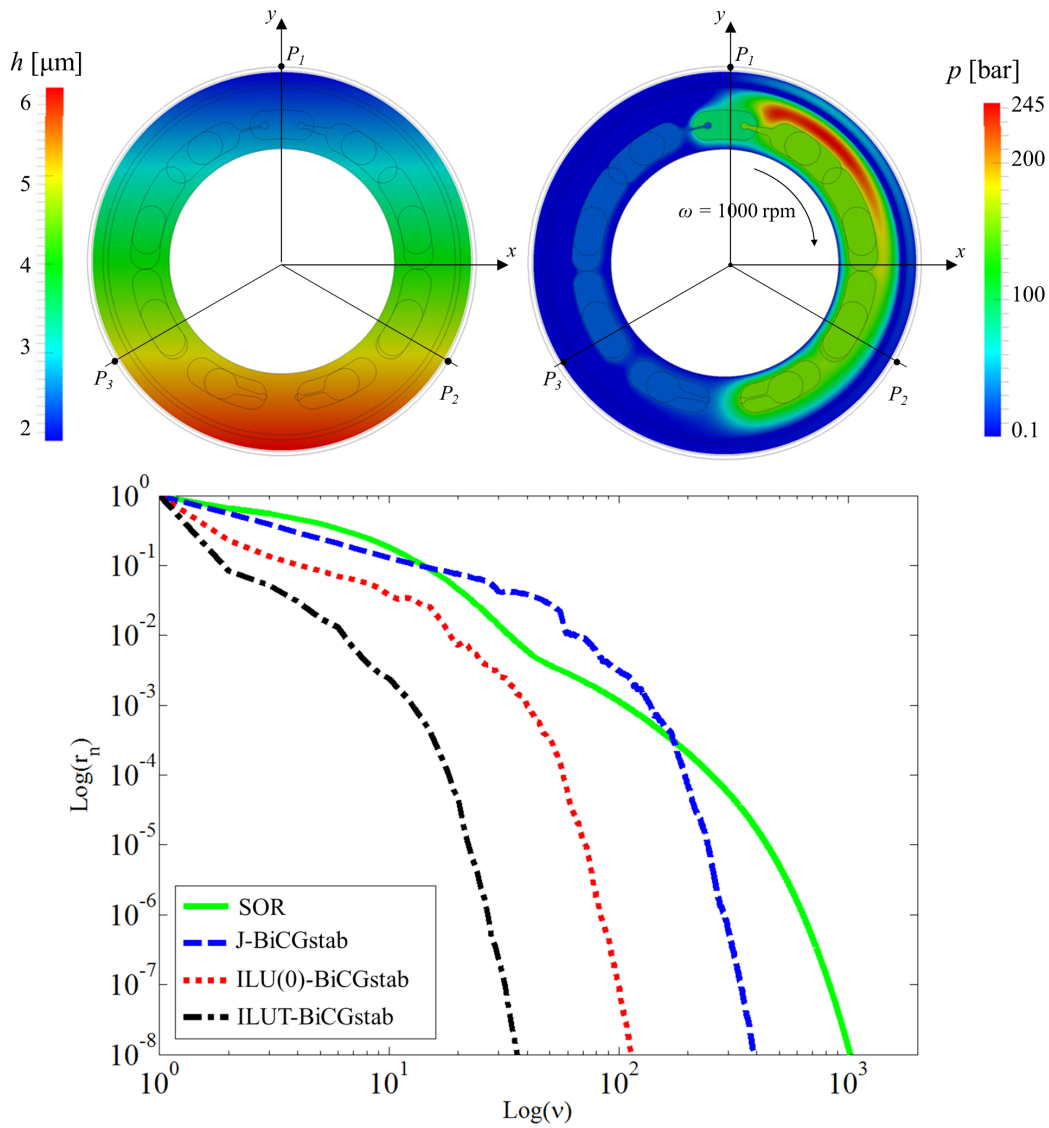

Fig. 4.9. Convergence behavior for different solution methods for a grid of $m \times n = 160 \times 1440$ elements (the non zero entries in $\mathbf{A}$ were 139924. The film thickness and the associated pressure field are also represented.

corresponds to a similar reduction in CPU time. However, on coarser grids the gain in time obtained by ILUT-BiCGstab solver is not as good as the gain in iterations. The solver needs in fact less iterations to reach a converged solution due to the smaller size of $\mathbf{A}$ and the advantage given by a better matrix preconditioning has a smaller

Grid size	Fluid elements	Computation time [ms]			
		SOR	J-BiCGstab	ILU(0)-BiCGstab	ILUT-BiCGstab
90×10	356	13	4	3	4
180×20	2320	62	17	12	16
360×40	8682	274	99	51	63
720×80	35413	2390	756	339	347
1440×160	139924	36880	5382	2404	2203

Table 4.1
Computation time in [ms] required by the solvers of Fig. 4.9 on different grid sizes. The processor was an Intel i7 870@2.93 GHz.

impact. For this reason the preconditioner that was chosen in this work is the ILU(0) which overall has shown the best performance; the ILU(0)-BiCGStab has shown of being (on average) at least five times faster than the SOR solver on the usual grid size used for practical computation. The implementation of an alegbraic multigrid method was investigated because it could probably be even faster than the ILU(0)-BiCGStab solver. However, if the solution time of the linear system in Eq. 4.17 is further decreased, the calculation of the elastic deformations of the solid parts (described in detail in chapter 6) become the actual bottleneck in the overall fluid structure interaction solution loop.

4.2.2 Treatment of sub-ambient pressure regions

In some conditions the solution of the Reynolds equation can predict sub-ambient pressure values, sometime even negative absolute pressure. This happens frequently in the cylinder block / valve plate interface. This situation is physically unacceptable because when the pressure in the lubricant drops below the saturation value, the dissolved gases will be released and furthermore vapor cavitation will occur if the pressure drops even further to the vapor pressure.

Mineral oils contain between 8 ans 12% of dissolved air and the saturation pressure can be assumed to be approximately equal (eventually slightly lower) to the ambient pressure, as the lubricant is exposed to the ambient atmosphere for long periods of time under normal operative conditions. When pressure reaches the saturation value air starts to come out of the solution and this phenomenon will maintain the pressure close to the the ambient level. In this work the Sommerfeld approach is used (see Szeri, 2011; Hamrock et al., 2004) and any pressure value lower than the saturation is forced to remain at that level. Practically the solution of the Reynolds equation is carried out using two pressure fields. The first is allowed to became negative and it is just used to monitor the convergence of the solution through the residual. On the second pressure field a minimum pressure value equal to the saturation point is enforced throughout the domain; this pressure field is used to calculate the forces associated to the pressure field, the elastic deformations and the fluid properties.

4.3 Discretization of the Energy equation

The Energy equation is partial differential equation describing a convective-diffusive process in three dimensions and it can be represented in compact form as follows:

$$\boldsymbol{\nabla} \cdot (\rho \boldsymbol{V} T - \Gamma \boldsymbol{\nabla} T) = S \tag{4.23}$$

The diffusion coefficient Γ and the source term S are defined as indicated in Eq. 4.24.

$$\Gamma = \frac{\lambda}{c_p}, \qquad S = \frac{\mu}{c_p} \Phi_d \tag{4.24}$$

The dissipation function Φ_d in Eq. 4.24 is expressed by Eq. 2.31; μ, c_p and λ are respectively the dynamic viscosity, heat capacity at constant pressure and thermal conductivity of the fluid. By applying the divergence theorem, with the same considerations of section 4.1.1, Eq. 4.23 becomes

$$\sum_{i=1}^{8} (\rho \boldsymbol{V}_i T_i - \Gamma_i \boldsymbol{\nabla} T_i) \cdot \delta \mathscr{A}_i \boldsymbol{n} \; = \int_{\mathscr{V}} S \tag{4.25}$$

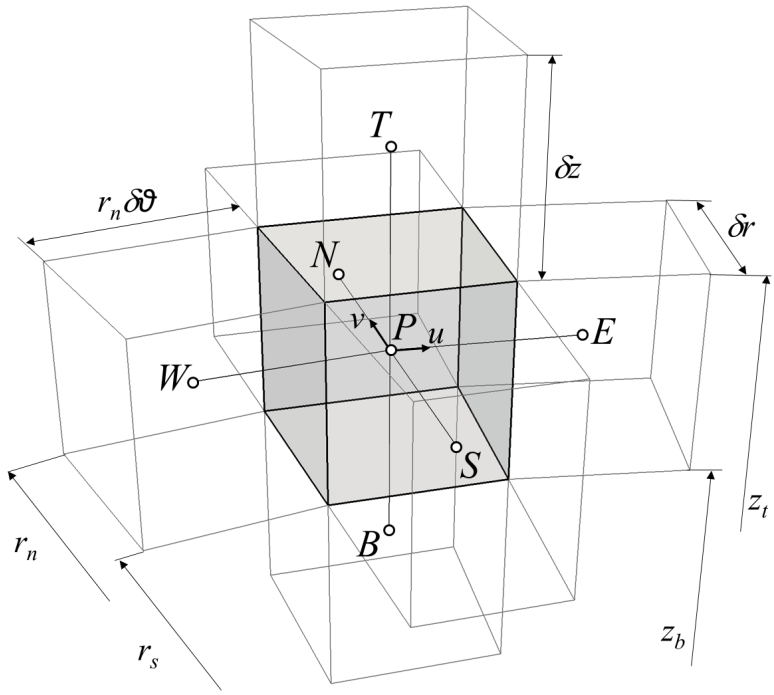

Fig. 4.10. Three dimensional elements used to discretize the Energy equation.

The summation in Eq. 4.25 is over the 8 faces w, e, s, n, b, t of the three dimensional element represented in Fig. 4.10. The convective and diffusive terms in Eq. 4.25 can be expanded as indicated in Eq. 4.26.

$$\begin{aligned}
&\left[(\rho uT)_w - \frac{\lambda_w}{c_{p_w}}\left(\frac{\partial T}{\partial \vartheta}\right)_w\right](\delta r\delta z_w) + \left[(\rho uT)_e - \frac{\lambda_e}{c_{p_e}}\left(\frac{\partial T}{\partial \vartheta}\right)_e\right](\delta r\delta z_e) + \\
&+\left[(\rho vT)_s - \frac{\lambda_w}{c_{p_s}}\left(\frac{\partial T}{\partial r}\right)_s\right](r_s\delta\vartheta\delta z_s) + \left[(\rho vT)_n - \frac{\lambda_w}{c_{p_n}}\left(\frac{\partial T}{\partial r}\right)_n\right](r_n\delta\vartheta\delta z_n) + \\
&+\left[-\frac{\lambda_b}{c_{p_b}}\left(\frac{\partial T}{\partial z}\right)_b\right]\left(\frac{\delta\vartheta}{2}\left(r_n^2 - r_s^2\right)\right) + \left[-\frac{\lambda_t}{c_{p_t}}\left(\frac{\partial T}{\partial z}\right)_t\right]\left(\frac{\delta\vartheta}{2}\left(r_n^2 - r_s^2\right)\right) = \\
&= \int_{\delta\mathscr{V}} S dv \qquad (4.26)
\end{aligned}$$

In Eq. 4.26 the convection does not apply on the bottom and top boundary faces (labeled with b and t) because, as indicated in Eq. A.5, there is no flow along the clearance.

The approximation of the diffusive terms is accomplished in the same way described in the case of the Reynolds equation (see Eq. 4.9).

$$\begin{aligned}
&\left(\frac{\partial T}{\partial \vartheta}\right)_w \approx \frac{T_P - T_W}{r\delta\vartheta}, \quad \left(\frac{\partial T}{\partial \vartheta}\right)_e \approx \frac{T_E - T_P}{r\delta\vartheta};\\
&\left(\frac{\partial T}{\partial r}\right)_s \approx \frac{T_P - T_S}{\delta r}, \quad \left(\frac{\partial T}{\partial r}\right)_n \approx \frac{T_N - T_P}{\delta r};\\
&\left(\frac{\partial T}{\partial z}\right)_b \approx \frac{T_P - T_B}{\delta z}, \quad \left(\frac{\partial T}{\partial z}\right)_t \approx \frac{T_T - T_P}{\delta z}.
\end{aligned} \tag{4.27}$$

In the case of the convective terms, the problem is to assign a temperature value to the cell faces when just the temperature at the cells centroid is known. The approach used to approximate the gradient at the face (CDS) is second order accurate, but it can be problematic if used to approximate the convective term, because it may lead to conditions in which the Scarborough criterion (introduced in section 4.1.1) is not satisfied, with a consequence possibility of divergence in the solution process.

An alternative scheme to the CDS is the Upwind Difference Scheme (UDS), which is first order accurate, but ensures stability in the solution process (see Patankar, 1980). According to the UDS scheme, the value of temperature at the cell faces depends upon the flow direction. The mass flow rates at the cell face is defined as in Eq. 4.28.

$$\begin{aligned}
&F_w = (\rho u)_w (\delta r \delta z_w), \quad F_e = (\rho u)_e (\delta r \delta z_e);\\
&F_s = (\rho v)_s (r_s \delta\vartheta \delta z_s), \quad F_n = (\rho v)_n (r_n \delta\vartheta \delta z_n).
\end{aligned} \tag{4.28}$$

With reference to Eq. 4.28, the temperature at the cell faces are defined as follows.

$$\begin{aligned}
&T_w = \begin{cases} T_W & \text{if } u_w > 0 \\ T_P & \text{otherwise} \end{cases}, \quad T_e = \begin{cases} T_P & \text{if } u_e > 0 \\ T_E & \text{otherwise} \end{cases};\\
&T_s = \begin{cases} T_S & \text{if } v_s > 0 \\ T_P & \text{otherwise} \end{cases}, \quad T_n = \begin{cases} T_P & \text{if } v_n > 0 \\ T_N & \text{otherwise} \end{cases};\\
&T_b = \frac{T_P + T_B}{2}, \qquad T_t = \frac{T_P + T_T}{2}
\end{aligned} \tag{4.29}$$

Combining Eq. 4.28 and 4.29, Eq. 4.26 can be rewritten in the standard form.

$$a_P T_P = a_W T_W + a_E T_E + a_S T_S + a_N T_N + a_B T_B + a_B T_B + b \tag{4.30}$$

The algebraic coefficients are represented in compact form as indicated by Eq. 4.31.

$$
\begin{aligned}
&a_W = \frac{\lambda \delta r \delta z_w}{r \vartheta c_p} + \max\left[F_w, 0\right], \quad a_E = \frac{\lambda \delta r \delta z_e}{r \vartheta c_p} + \max\left[-F_e, 0\right]; \\
&a_S = \frac{\lambda r_s \delta \vartheta \delta z_s}{\delta r c_p} + \max\left[F_s, 0\right], \quad a_N = \frac{\lambda r_n \delta \vartheta \delta z_n}{\delta r c_p} + \max\left[-F_n, 0\right]; \\
&a_B = \frac{\lambda \delta \vartheta \left(r_n^2 - r_s^2\right)}{2 \delta z c_p}, \qquad a_T = \frac{\lambda \delta \vartheta \left(r_n^2 - r_s^2\right)}{2 \delta z c_p} \\
&a_P = a_W + a_E + a_S + a_N + a_B + a_T + \left(F_e - F_w + F_n - F_s\right) \\
&b = \delta \mathscr{V} \frac{\mu_P}{cp} \left[\left(\frac{u_T - u_B}{2 \delta z} \right)^2 + \left(\frac{v_T - v_B}{2 \delta z} \right)^2 + \frac{4}{3} \left(\frac{u_P}{r_P} \right)^2 + \left(\frac{v_P}{r_P} \right)^2 \right] \\
&\delta \mathscr{V} = \left[\frac{\delta z_P \delta \vartheta}{2} \left(r_n^2 - r_s^2\right) \right]
\end{aligned}
\tag{4.31}
$$

In this case the source term does not need to be linearized; moreover it is interesting to observe that a_P contains also the extra mass flow rate $(F_e - F_w + F_n - F_s)$. For continuity-satisfying flow this extra term is zero, but if for some reason the continuity is not satisfied the solution can became problematic or incorrect.

4.3.1 Boundary conditions

In order to solve the Energy equation, diffusive and convective boundary conditions have to be applied. With reference to Fig. 4.11, specified temperatures are applied to all the surfaces, whereas specified velocities are applied only on the lateral surfaces. For what concerns diffusion, the effect of the applied temperature on lateral boundaries is negligible respect the effect of the applied temperature on the top and bottom ones, because the surfaces associated with the latter are two order of magnitude bigger. An accurate estimation of the surface temperature of the solid parts is therefore essential to ensure a reasonable solution of the Energy equation and this is the reason why the fluid flow module is coupled with the heat transfer module in Fig. 3.1

The lateral surfaces are instead very important for the convection, especially in situations where the interface operates under high film thickness conditions, because

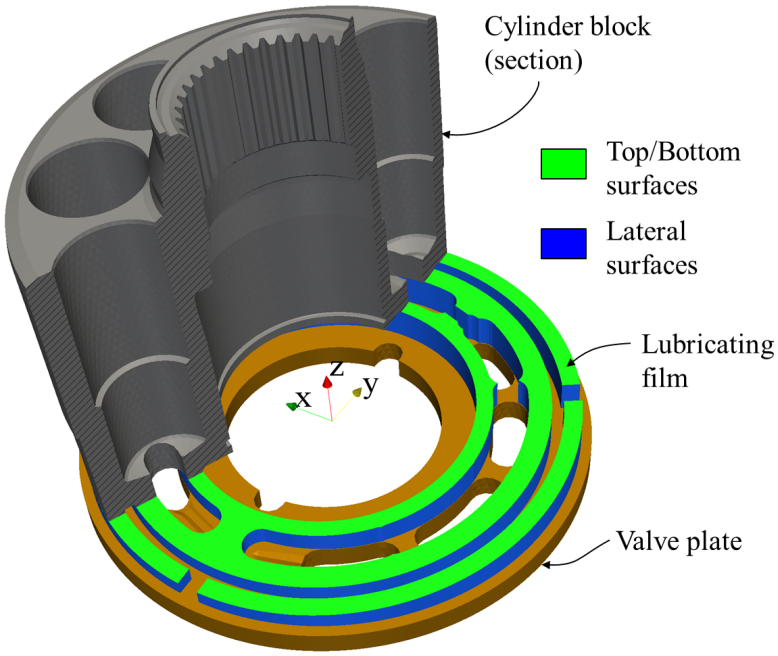

Fig. 4.11. Lubricating film (scaled 1000 times in z direction) and different surfaces where boundary conditions are required to solve the Energy equation.

part of the heat that is generated in the clearance through viscous dissipation is then carried off by the convective effect of the leakages. The convection effect at the boundaries can be due to flow entering or leaving the clearance; the first case usually occurs around the kidney openings of the cylinder block or the valve plate ports, the second at the peripherals region of the sealing land, since that is the path followed by the leakage flow.

In the case of an inflow boundary, a certain amount of oil enters in the cell with a specified temperature. Figure 4.12(a) illustrates an example where oil flows from the high pressure port into the cell P through the face w (with a velocity u_w); since the oil comes from the high pressure port its temperature is given. The high pressure port temperature, as well as the low pressure port and case temperatures are usually known from measurements.

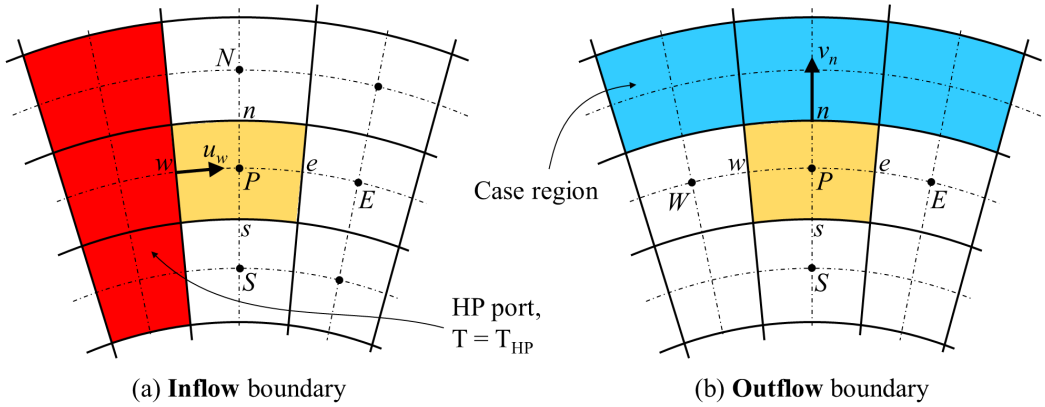

Fig. 4.12. Example of inflow and outflow boundaries in the solution of the Energy equation.

In the case illustrated in Fig. 4.12(a) the set of coefficients in Eq. 4.31 is modified as follows.

$$
\begin{aligned}
a_W &= 0, & a_E &= \frac{\lambda \delta r \delta z_e}{r \vartheta c_p} + \max\left[-F_e, 0\right]; \\
a_S &= \frac{\lambda r_s \delta \vartheta \delta z_s}{\delta r c_p} + \max\left[F_s, 0\right], & a_N &= \frac{\lambda r_n \delta \vartheta \delta z_n}{\delta r c_p} + \max\left[-F_n, 0\right]; \\
a_B &= \frac{\lambda \delta \vartheta \left(r_n^2 - r_s^2\right)}{2 \delta z c_p}, & a_T &= \frac{\lambda \delta \vartheta \left(r_n^2 - r_s^2\right)}{2 \delta z c_p} \\
a_P &= \frac{2 \lambda \delta r \delta z_w}{r \vartheta c_p} + a_E + a_S + a_N + a_B + a_T + \left(F_e + F_n - F_s\right) \\
b &= \delta \mathscr{V} \frac{\mu_P}{cp} \left[\left(\frac{u_T - u_B}{2 \delta z} \right)^2 + \left(\frac{v_T - v_B}{2 \delta z} \right)^2 + \frac{4}{3} \left(\frac{u_P}{r_P} \right)^2 + \left(\frac{v_P}{r_P} \right)^2 \right] + \left| F_w \right| T_{HP}
\end{aligned}
\tag{4.32}
$$

The source b is affected by the convective term $|F_w| T_{HP}$, which turns out to be always positive (no matter the boundary face is w, e, s or n). As in the case of Eq. 4.16 the a_p term is affected by the diffusion and, in addition, the inflow boundary is responsible of the missing F_w term in the extra mass flow rate (since the convection on the w face appears as a known term into b).

An example of outflow boundary is represented in Fig. 4.12 as well, where oil at temperature T_n is flowing from the cell P into the case region through the face n (with a velocity v_n). In this situation the temperature T_n can be defined as the temperature T_P at the cell centroid using the first order upwind scheme. However T_P

is unknown and therefore this type of boundary will not affect the source but just a_P. An extra term F_n would need to be added to a_P but that is already in Eq. 4.31, thus the only changes to Eq. 4.31 are given by the diffusion boundary, as shown in Eq. 4.33.

$$\begin{aligned}
&a_W = \frac{\lambda \delta r \delta z_w}{r \vartheta c_p} + \max\left[F_w, 0\right], a_E = \frac{\lambda \delta r \delta z_e}{r \vartheta c_p} + \max\left[-F_e, 0\right]; \\
&a_S = \frac{\lambda r_s \delta \vartheta \delta z_s}{\delta r c_p} + \max\left[F_s, 0\right], a_N = 0; \\
&a_B = \frac{\lambda \delta \vartheta \left(r_n^2 - r_s^2\right)}{2 \delta z c_p}, a_T = \frac{\lambda \delta \vartheta \left(r_n^2 - r_s^2\right)}{2 \delta z c_p} \\
&a_P = a_W + a_E + a_S + \frac{2 \lambda r_n \delta \vartheta \delta z_n}{\delta r c_p} + a_B + a_T + \left(F_e - F_w + F_n - F_s\right) \\
&b = \delta \mathscr{V} \frac{\mu_P}{cp} \left[\left(\frac{u_T - u_B}{2 \delta z} \right)^2 + \left(\frac{v_T - v_B}{2 \delta z} \right)^2 + \frac{4}{3} \left(\frac{u_P}{r_P} \right)^2 + \left(\frac{v_P}{r_P} \right)^2 \right]
\end{aligned} \tag{4.33}$$

4.4 Solution of the energy equation

Combining the algebraic Eq. 4.14 for all the control volumes in the computational domain a linear system of the form of Eq. 4.17 is obtained. The Energy equation does not present any non-linearity and therefore a convergence loop like the one presented in the case of the Reynolds equation is not necessary. Also in this case the ILU(0)-BiCGstab solver described in section 4.2 was used used for the solution of the linear system.

5. THE HEAT TRANSFER PROBLEM

The heat transfer problem consists in the determination of the temperature field in the solid parts surrounding the lubricating interface. The governing equation is the steady state, conductive form of the Energy equation:

$$\boldsymbol{\nabla} \cdot (\lambda \boldsymbol{\nabla} T) = 0 \tag{5.1}$$

Equation 5.1 can be solved numerically with different methods, like finite volumes, finite differences or finite elements. The solid bodies associated with the cylinder block / valve plate interface have complex shape and their discretization can be achieved effectively only with unstructured grids, making more appealing methods like finite volumes or finite elements. As already described in section 4.1 the finite volumes method can deal with complex geometries but its formulation becomes more complex in that case. On the other hand, the advantage of the finite volumes method's unstructured formulation is that the control volumes can be polyhedral of general shape, with a variable number of neighbors: this gives to the grid generation remarkable freedom and flexibility. The finite elements method formulation is intrinsically unstructured but the implementation complexity depends on the type of elements selected. If elements with moderately easy formulation are used, the finite elements method becomes more attractive than the finite volumes method.

In this work the discretization of the solid parts is achieved through a commercial software using tetrahedral elements, because the complex tridimensional shapes of the solid parts can be modeled effectively with limited effort. Since the tetrahedron is the only element that is used, the finite element formulation of the heat transfer problem was preferred to the finite volumes counterpart, because besides being easier to implement it also turned out being computationally faster. Furthermore, a similar finite element formulation can be used to model the linear elastic deformation

problem associated with the determination of the thermal deflections or the pressure deformation, and the two problems can be solved through a unique thermo-elastic finite element solver.

5.1 Boundary conditions

Solution of Eq. 5.1 requires a proper set of boundary conditions to be applied on all the external surfaces $\mathcal{S}_i$ of the solid part. Formally, three types of boundary conditions can be applied:

Dirichlet condition: the surface temperature is fixed and it can be represented either by a uniform value or by a non uniform temperature field

Neumann condition: an heat flux q_i is directly applied to the boundary surface $\mathcal{S}_i$; q_i can be either represented either by a uniform or a non-uniform field.

Mixed condition: an heat flux q_i is indirectly applied to the boundary surface $\mathcal{S}_i$ through the Newton's law of cooling

$$q_i = h\left(T_{\mathcal{S}_i} - T_\infty\right) \tag{5.2}$$

where h is the convection coefficient associated with the heat exchange on the surface $\mathcal{S}_i$, $T_{\mathcal{S}_i}$ is the surface temperature and T_∞ the temperature of the fluid surrounding the surface.

In the case of the cylinder block / valve plate interface the Dirichlet condition is never applied because all the surface temperatures are essentially unknown. Mixed condition is always preferred because T_∞ can be easily determined through measurements and h can be estimated with acceptable level of accuracy through numerical correlations or CFD analysis. Neumann conditions are applied whenever a precise estimation of the heat flux applied to $\mathcal{S}_i$ is available: this is the case of the sealing surfaces defining the interface, because the heat fluxes are calculated from the knowledge of the temperature field in the lubricant through the Fourier law, Eq. 2.33.

5.1.1 Calculation of the heat fluxes towards the solid parts

The calculation of the heat fluxes towards the solid parts is fundamental to accurately predict the lubricating interface performance. As already anticipated in chapter 3.1 the solid body temperature affects the thermal deflections and therefore the predicted geometry of the clearance; furthermore, the solid part's surface temperature is the most important boundary condition in the solution of the Energy equation in the lubricant and its incorrect estimation will lead to a wrong prediction of the fluid property (viscosity especially).

The heat flux from the lubricant to the solid parts is defined by the Fourier Eq. 2.33, which can be approximated as follows:

$$q(r,\vartheta) = -\lambda \left(\frac{\partial T(r,\vartheta)}{\partial z(r,\vartheta)} \right)_{wall} \approx -\lambda \frac{2\left(T_s(r,\vartheta) - T_f(r,\vartheta)\right)}{\delta z(r,\vartheta)} \tag{5.3}$$

where λ is the thermal conductivity of the oil, T_s is the surface temperature and T_f the fluid temperature at the fluid cell attached to the boundary surface; δz is the size of the cell in z direction, the factor 2 comes from the fact that the distance between the fluid element centroid (where the information of temperature is available) and the surface is just half of the element size.

As indicated in Eq. 5.3, the heat flux is in general non uniform, being a function of the angular and radial positions in the clearance; moreover the two grids used to solve the fluid flow and the heat transfer problems are different, being the first a structured grid of quad elements and the second an unstructured tetrahedral grid. To solve the problem of transferring a given field from the centroids of the fluid grid to the faces of the structure grid a "cells to cells" interpolation method was developed, and is described in section 6.5.

5.1.2 Estimation of the convection coefficients

Mixed boundary conditions are widely used to model the thermal behavior of the cylinder block / valve plate interface. However, Eq. 5.2 describes a very complicated

phenomenon through a very simple formulation, addressing all the complication of the problem to the determination of the convection coefficient h. Chen (2005) developed a methodology to estimate the convection coefficient for the cylinder block's external surfaces based on empirical correlations, valid for simplified situations. In this work, some of the results from Chen (2005) were used, but in order to improve the accuracy and to extend the analysis to the valve plate and end case bodies a CFD based methodology was introduced.

The heat transfer in the rotating kit of axial piston machines represent a conjugate heat transfer problem, where the solution should be extended to the fluid and solid domains. Nevertheless, these type of analysis are complicated and acceptable results can be achieved by solving just for the fluid domain, imposing either a fixed temperature or a fixed heat flux boundary condition at the interface with the solid. In the first case, by combining the Fourier's law (Eq. 2.33) with the Newton's law of cooling (Eq. 5.2) the convection coefficient is defined as:

$$h = -\frac{\lambda \left(\boldsymbol{\nabla} T\right)_w \cdot \boldsymbol{n}}{T_w - T_\infty} \tag{5.4}$$

In Eq. 5.4, λ is the thermal conductivity of the oil, T_w the wall temperature, T_∞ the bulk temperature of the oil and $\boldsymbol{n}$ the vector normal to the surface defining the fluid region. In the second case, since the heat flux q_b is imposed, the Fourier's law doesn't need to be used and the convection coefficient is simply given by Eq. 5.5.

$$h = \frac{q}{T_w - T_\infty} \tag{5.5}$$

The determination of the convection coefficient will be different if a fixed temperature or a fixed heat flux are applied. However, the results are not much different and a possible approach is to take a value within the two extremes defined by these two types of boundary conditions.

The domain considered in the study being presented is illustrated in Fig. 5.1. The displacement chambers, the valve plate port and the discharge canal are modeled, in order to capture the full path followed by the oil during the displacement action of the

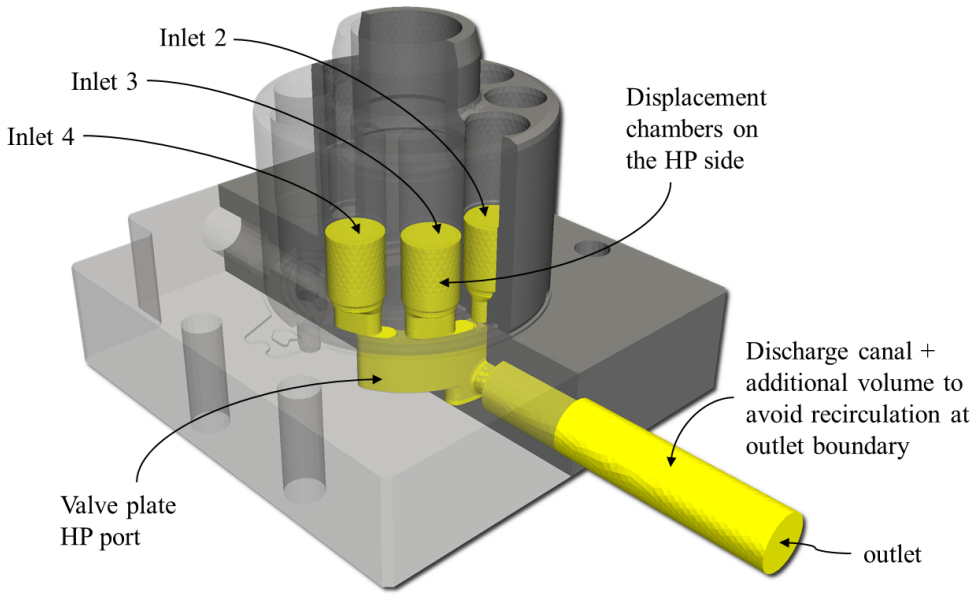

Fig. 5.1. Fluid domain used to estimate the convection coefficient.

machine; an additional volume was added to the discharge canal to avoid recirculation at the outlet.

Governing equations and solution scheme

The fluid flow in the domain illustrated in Fig. 5.1 needs to be modeled with the full Navier-Stokes Eq. A.1 and in addition the effect of turbulence have to be considered. A possible approach to solve the problem is to consider the mean flow through the Reynolds decomposition, where the flow is decomposed into time-averaged and fluctuating quantities. The resulting Reynolds stress tensor is determined through a turbulence model, thtough the so called turbulence viscosity hypothesis (see Versteeg and Malalasekera, 2007); such model is known as RANS, which stands for Reynolds Averaged Navier-Stokes. Moreover, in order to determine the temperature in the fluid flow, the energy equation 2.29 has to be linked with the solution process.

Therefore, the governing equations of the problem are

- Full Navier-Stokes equation, Eq. A.1;
- Continuity equation, Eq. A.6;
- Transport equations for the turbulent kinetic energy k and its dissipation rate ϵ (a good description of the $k - \epsilon$ model and the formulation of the model equations can be found in Versteeg and Malalasekera 2007);
- Energy equation, Eq. 2.29.

The fluid flow was solved with an external open source software, OpenFOAM, from the ESI Group. The SIMPLE (Semi Implicit Method for Pressure Linked Equations) method developed by Patankar (1980) is already implemented in an incompressible, steady state solver offered by OpenFOAM, which can also be linked with a variety of RANS turbulence models through the turbulence viscosity. The SIMPLE solver in the official release was modified in this work to account also for the thermal problem, by adding the energy equation to in the solution process. A number of

The dynamic of the discharge process was not modeled for the same reasons described in section 3.1 about the stationary character of the thermal problem.

Boundary conditions

In order to solve the problem, a proper set of boundary condition have to be defined for each of the solution variable. The different boundary conditions defined for the solution of the non-isothermal turbulent flow in the domain of Fig. 5.1 are summarized below.

$\boldsymbol{V}$: the velocity of the fluid at the inlet is assumed to be the same of the piston velocity, described by Eq. 2.3 as a function of the angular position φ; on the walls the non-slip condition is applied and the velocity gradient is specified to be zero at the outlet.

p : according to the velocity boundary, pressure is specified to have zero gradient at the inlets and on the walls, whereas is imposed to a fixed value of 1 bar at the outlet;

T : temperature is specified at the inlet, the walls are fixed to a uniform temperature or uniform heat flux and the outlet is always set to zero heat flux condition.

k : as suggested by Versteeg and Malalasekera (2007) the turbulent kinetic energy is assigned through the indication of the turbulence intensity T_i (a typical value for high speed flow inside complex geometry is 10%):

$$k_i = \frac{3}{2}(VT_i)^2 \tag{5.6}$$

At the outlet the zero gradient conditions applies, whereas wall functions (see Versteeg and Malalasekera, 2007) are automatically applied by the solver to all the walls.

ϵ : the rate of dissipation of the turbulence kinetic energy at the inlet is suggested by Versteeg and Malalasekera (2007) to be calculated as

$$\epsilon = C_\mu^{3/2} \frac{k_i^{3/2}}{d_K} \tag{5.7}$$

where C_μ is one of the five constant of the model and d_K is the piston diameter. Likewise for k, zero gradient conditions applies at the outlet and wall functions are automatically applied by the solver to all the walls.

Example of calculated heat transfer coefficient

Figure 5.2 shows an example of calculated convection coefficient over the displacement chamber surface of the cylinder block and also how the average value over the surface changes with the outlet flow in the case of a pump of commercial production. The calculations were made by assuming the maximum speed of the pistons, therefore the actual values of the convection coefficient have has to be reduced of a factor of $2/\pi$, which comes from the average of the pistons speed expressed through Eq. 2.3.

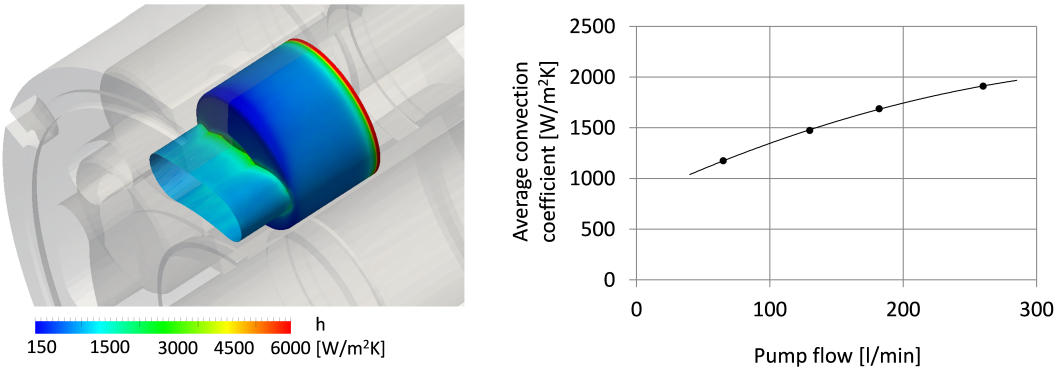

Fig. 5.2. Example of calculated convection coefficient and variation of the average value among the surface as a function of pump flow.

Another example is represented in Fig. 5.3 for the low and high pressure ports in the end case. It is interesting to notice that due to the different geometry of the two

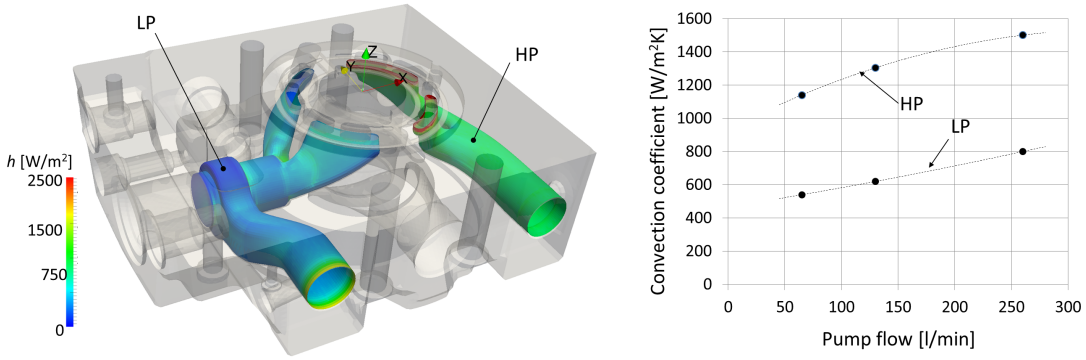

Fig. 5.3. Example of calculated convection coefficient for 130 l/min pump flow and variation of average convection coefficient upon the surface as a function of the pump flow.

ports in this example, the two values of the convection coefficient change significantly. The high pressure port has smaller section and therefore higher fluid speed than the low pressure port with a resulting more important heat exchange through convection.

5.2 Typical settings of the thermal boundary conditions

The entire external surfaces of the cylinder block and valve plate & end case assembly are split into a set of patches where a specific thermal boundary condition is applied. Each patch should define a surface where a known heat flux is applied or a surface where the convective heat exchange has more or less the same intensity.

Figure 5.4 illustrates the typical thermal boundary conditions applied to the cylinder block body. The sealing land surface is indicated with `gap`; a heat flux calculated

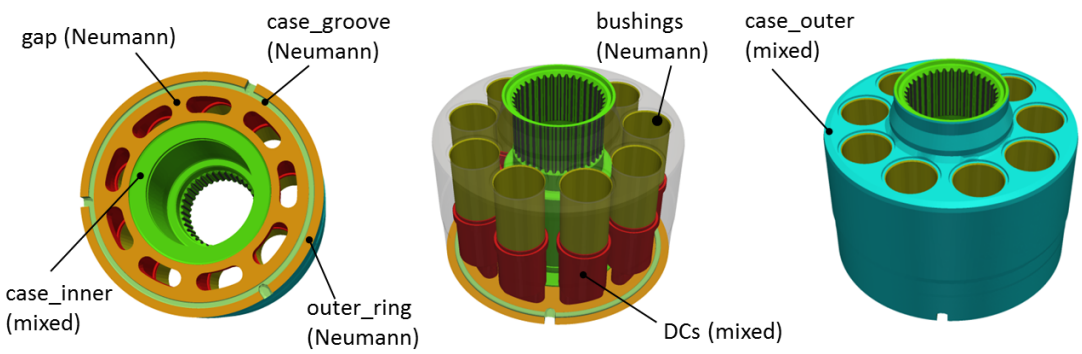

Fig. 5.4. Thermal boundary condition applied to the cylinder block body.

through Eq. 2.24 is applied (Neumann condition). In the presented example the `outer_ring` surface encloses a thicker region of fluid where hydrodynamic effects are not present, the heat dissipation can be calculated by simplifying the expression of the viscous dissipation function. Assuming $R_{or,in}$ and $R_{or,out}$ to be the inner and outer radii of the outer bearing, and h_{or} the fluid film thickness the heat flux associated with this region is approximated through the viscous dissipation as follows:

$$q \approx \frac{\mu h_{or} \pi \left(R_{or,out}^2 - R_{or,in}^2\right) \left(\frac{\partial v}{\partial z}\right)^2}{2\pi \left(R_{or,out}^2 - R_{or,in}^2\right)} = \frac{\mu h_{or} \left[\frac{\omega (R_{or,out} + R_{or,out})}{2h_{or}}\right]^2}{2} \tag{5.8}$$

In Eq. 5.8 the viscous dissipation is calculated as gradient of the circumferential velocity determined by the dragging effect of the cylinder block; the power dissipated in the fluid is assumed to head to the cylinder block and valve plate in the same amount.

A similar approach is followed to calculate the heat flux over the `case_groove` surface. The heat fluxes applied to the bushings are calculated using a fluid structure interaction and thermal model for the piston cylinder interface developed by Pelosi (2012) and therefore a Neumann condition is applied.

Figure 5.5 illustrates the typical thermal boundary conditions applied to the valve plate and end case assembly. Likewise the cylinder block, the same Neumann condi-

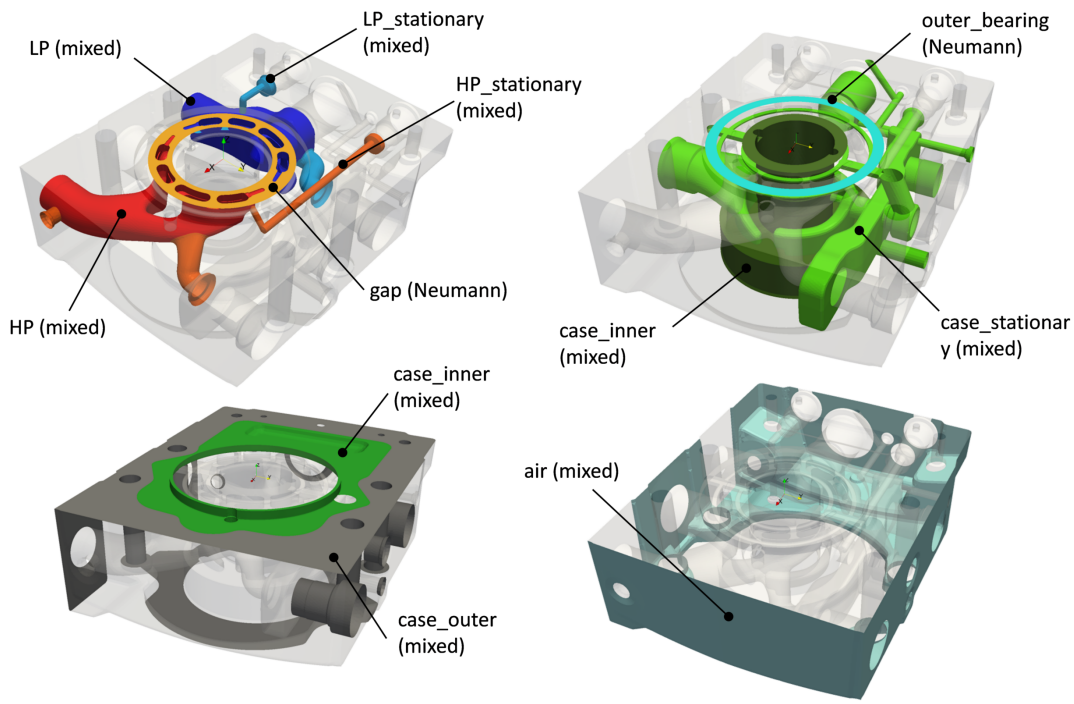

Fig. 5.5. Thermal boundary condition applied to the valve plate and end case assembly.

tion is applied on the surface `gap` in contact with the fluid film and on the surface `outer_bearing` corresponding to the outer bearing. The two ports of low and high pressures were split into a "main" and a "stationary" regions. The main part is where the fluid flows through suction and delivery, whereas the stationary regions are connected to closed ports and the fluid is not expected to exchange much heat there since it doesn't really move.

In any region of the end case where the fluid is stationary, the heat exchanged is calculated by assuming a low value of convection coefficient, typically 50 W/m^{2}K; an example in Fig. 5.5 is the surface labeled as `case_sationary` which corresponds to the inlet of the charge pump and an additional internal pocket. The outer part of the end case in contact with the ambient was labeled as `air`, a value of 30 W/m^{2}K and a surrounding temperature of 25°C were applied. Some of the outer surface of the end case are also in contact with other metallic parts like the bottom surface of the housing and the flange fittings on the low and high pressure ports; these surfaces are likely to be at a temperature close to the fluid in the case. A Dirichlet condition could be applied, but a mixed condition with high convection coefficient was preferred because a little more flexible.

5.3 Finite element discretization of the heat transfer equation

The finite element discretization of the heat transfer equation is accomplished with an approach based on the Galerkin weighted residual method of approximating solutions to differential equations. Weighted residual methods are based on the definition of an assumed solution (trial function) which satisfies the boundary conditions but does not solve exactly the partial differential equation inside its domain. In the case of Eq. 5.1, indicating the assumed solution with $\tilde{T}$, the error is defined as follows:

$$e(x, y, z) = \boldsymbol{\nabla} \cdot \left(\lambda \boldsymbol{\nabla} \tilde{T}\right) \neq 0 \tag{5.9}$$

The trial function $\tilde{T}$ is defined through a certain number of arbitrary parameters a_i that are adjusted in order to minimize the integral of the error of the assumed solution. More precisely, the weighted residual methods require the integral of the error times a weighting function W_i to be zero throughout the element volume $\delta\mathscr{V}$:

$$\int_{\delta\mathscr{V}} W_i e dv = \int_{\delta\mathscr{V}} W_i \boldsymbol{\nabla} \cdot \left(\lambda \boldsymbol{\nabla} \tilde{T}\right) dv = 0 \tag{5.10}$$

Equation 5.10 can be rewritten by expanding the term in the integral:

$$\int_{\delta\mathscr{V}} \boldsymbol{\nabla} \cdot \left(W_i \lambda \boldsymbol{\nabla} \tilde{T} \right) dv - \int_{\delta\mathscr{V}} \boldsymbol{\nabla} W_i \cdot \lambda \boldsymbol{\nabla} \tilde{T} dv = 0 \tag{5.11}$$

Equation 5.11 can be further reworked by applying the divergence theorem to the first member:

$$\int_{\delta\mathscr{A}} W_i \lambda \boldsymbol{\nabla} \tilde{T} \cdot \boldsymbol{n} da - \int_{\delta\mathscr{V}} \boldsymbol{\nabla} W_i \cdot \lambda \boldsymbol{\nabla} \tilde{T} dv = 0 \tag{5.12}$$

A convenient formulation of $\tilde{T}$ defines the arbitrary parameters a_i to be represented by the value of the dependent function at the nodes of the finite element. In this case it can be shown (see Grandin, 1986) that the trial function is defined through the product of the natural coordinate matrix $\mathbf{N}$ and the temperature nodal vector $\boldsymbol{T}_i$:

$$\tilde{T} = \mathbf{N}^T \boldsymbol{T}_i \tag{5.13}$$

The Galerkin method defines the weighting factors as the derivative of the trial function with respect to the coefficients a_i. With the choice of the temperature nodal vector as trial function's parameters the weighting function is just

$$W_i = \frac{\partial \tilde{T}}{\partial T_i} = \mathbf{N}^T \tag{5.14}$$

Substituting Eq. 5.14 into Eq. 5.12 yields to

$$\int_{\delta\mathscr{A}} \mathbf{N}^T \lambda \boldsymbol{\nabla} \tilde{T} \cdot \boldsymbol{n} da - \int_{\delta\mathscr{V}} \boldsymbol{\nabla} \mathbf{N}^T \cdot \lambda \boldsymbol{\nabla} \tilde{T} dv = 0 \tag{5.15}$$

The first member in Eq. 5.15 represent the integral of the heat flux $\boldsymbol{q}$ on the element's face; moreover the second member can be rewritten using the definition of the trial function 5.13

$$\int_{\delta\mathscr{A}} \mathbf{N}^T \boldsymbol{q} \cdot \boldsymbol{n} da - \lambda \int_{\delta\mathscr{V}} \boldsymbol{\nabla} \mathbf{N}^T \boldsymbol{\nabla} \mathbf{N} dv \, \boldsymbol{T}_i = \int_{\delta\mathscr{A}} \mathbf{N}^T \boldsymbol{q} \cdot \boldsymbol{n} da - \int_{\delta\mathscr{V}} \mathbf{B}^T \mathbf{C} \mathbf{B} dv \, \boldsymbol{T}_i = 0 \tag{5.16}$$

In Eq. 5.16 the temperature-gradient interpolation matrix $\mathbf{B} = \boldsymbol{\nabla} \mathbf{N}$ and the constitutive matrix $\mathbf{C}$ have been introduced; for the thermal problem, assuming the

material isotropic, the constitutive matrix is a diagonal matrix having the thermal conductivity on the main diagonal:

$$\mathbf{C} = \begin{bmatrix} \lambda & 0 & 0 \\ 0 & \lambda & 0 \\ 0 & 0 & \lambda \end{bmatrix} \tag{5.17}$$

According to the type of boundary condition, the first member of Eq. 5.16 can be written as follows:

$$\int\limits_{\delta\mathscr{A}} \mathbf{N}^T \boldsymbol{q} \cdot \boldsymbol{n} da = \begin{cases} \int\limits_{\delta\mathscr{A}} \mathbf{N}^T \boldsymbol{q_b} \cdot \boldsymbol{n} da & \text{for Neumann bounday} \\ h \int\limits_{\delta\mathscr{A}} \mathbf{N}^T \left(T - T_\infty\right) da & \text{for Mixed bounday} \end{cases} \tag{5.18}$$

The Mixed boundary can be further expanded by expressing T through the nodal temperatures $\boldsymbol{T}_i$ as follows:

$$h \int\limits_{\delta\mathscr{A}} \mathbf{N}^T \left(T - T_\infty\right) da = h \int\limits_{\delta\mathscr{A}} \mathbf{N}^T \mathbf{N} da \, \boldsymbol{T}_i - h \int\limits_{\delta\mathscr{A}} \mathbf{N}^T T_\infty da \tag{5.19}$$

Combining Eq. 5.16, 5.18 and 5.19 the standard finite elements formulation of the problem is obtained:

$$\mathbf{k}_T \boldsymbol{T}_i = \boldsymbol{q}_{cv} + \boldsymbol{q}_b \tag{5.20}$$

The thermal stiffness matrix $\mathbf{k}_T$ is defined mainly by the conductive matrix $\mathbf{k}_{cd}$ but, if at least one face of the element has a convective boundary, the convective matrix $\mathbf{k}_{cv}$ needs to be included as well:

$$\mathbf{k}_T = \mathbf{k}_{cd} + \mathbf{k}_{cv} = \int\limits_{\delta\mathscr{V}} \mathbf{B}^T \mathbf{C} \mathbf{B} dv + h \int\limits_{\delta\mathscr{A}} \mathbf{N}^T \mathbf{N} da \tag{5.21}$$

The convection and applied heat boundary "force" vectors are defined as

$$\boldsymbol{q}_b = \int\limits_{\delta\mathscr{A}} \mathbf{N}^T \boldsymbol{q_b} \boldsymbol{n}^T da \tag{5.22}$$

$$\boldsymbol{q}_{cv} = h \int\limits_{\delta\mathscr{A}} \mathbf{N}^T T_\infty da \tag{5.23}$$

The explicit definition of Eq. 5.20 depends on the type of element that is used to discretize the continuum.

Extending the analysis to all the elements discretizing the continuum, a linear problem similar to Eq. 5.20 is obtained:

$$\mathbf{K}_T \boldsymbol{T}_i = \boldsymbol{Q}_{cv} + \boldsymbol{Q}_b \tag{5.24}$$

where $\mathbf{K}_T$ is the global thermal stiffness matrix and $\boldsymbol{Q}_{cv}$ and $\boldsymbol{Q}_b$ are the total convection and applied heat boundary force vectors resulting from all the boundary surfaces. The global thermal stiffness matrix is a square, sparse, symmetric matrix and its size is equal to the total number of nodes used to discretize the continuum because each node has just one degree of freedom, the nodal temperature. This makes the assembling process straightforward, because the global numbering of each node corresponds to the position in the stiffness matrix. Details about the global stiffness matrix assembly can be found in Grandin (1986).

5.4 The linear tetrahedron

The tetrahedron element is the easiest tridimensional element to construct mathematically. In terms of accuracy however the tetrahedron is not the best choice because, as it will be shown shortly, the approximate solution is forced to vary linearly throughout the element. On the other hand, besides the straightforward mathematical formulation, the tetrahedron allows the finite element problem to be defined quickly and with a limited amount of memory. Moreover, if required, the solution accuracy associated with higher order elements can be approached with finer tetrahedral meshes. These arguments, combined with the ability to mesh virtually any kind of geometry, made the tetrahedron the element chose for all the FEM analysis carried out in this work.

Figure 5.6 represent a tetrahedron with its local node numbering and the definition of the natural coordinates. A point P in the tetrahedron is identifies by the four natural coordinates L_1, L_2, L_3 and L_4. As illustrated in Fig. 5.6 in the case of L_1,

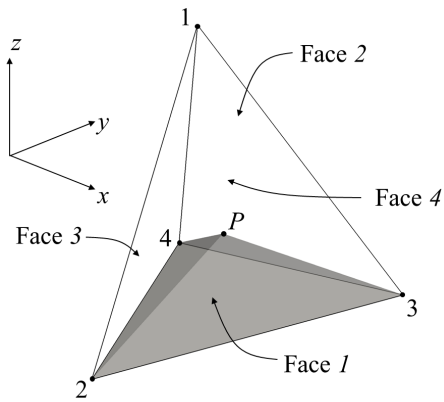

Fig. 5.6. Tetrahedron element, local numbering and definition of the natural coordinate

each coordinated is determined by the ratio between the volume $\delta\mathscr{V}_i$ of the tetrahedron defined by the point P and one of the four faces and the total volume $\delta\mathscr{V}$:

$$L_i = \frac{\delta\mathscr{V}_i}{\delta\mathscr{V}} \tag{5.25}$$

However, only three of the four natural coordinates are linearly independent and in fact the sum of the four sub-tetrahedra has to be equal to the total tetrahedron volume:

$$L_1 + L_2 + L_3 + L_4 = 1 \tag{5.26}$$

The tetrahedron is defined as an isoparametric element because the natural coordinates are the interpolation coefficients to express the temperature T at any given point P inside the tetrahedron as a function of the nodal values:

$$\begin{aligned} T(P) = L_1T_1 + L_2T_2 + L_3T_3 + (1 - L_1 - L_2 - L_3)T_4 = \\ = L_1(T_1 - T_4) + L_2(T_2 - T_4) + L_3(T_3 - T_4) + T_4 \end{aligned} \tag{5.27}$$

and the global coordinates of a given point as a function of the nodal position:

$$\begin{cases} x = L_1(x_1 - x_4) + L_2(x_2 - x_4) + L_3(x_1 - x_4) + x_4 \\ y = L_1(y_1 - y_4) + L_2(y_2 - y_4) + L_3(y_1 - y_4) + y_4 \\ z = L_1(z_1 - z_4) + L_2(z_2 - z_4) + L_3(z_1 - z_4) + z_4 \end{cases} \tag{5.28}$$

From Eq. 5.27 it can be noticed that the variation of temperature in the element is linear and therefore the temperature gradient will be constant throughout the element.

5.4.1 The temperature-gradient interpolation matrix

The temperature-gradient interpolation matrix expresses the temperature gradient in the element as a function of the nodal temperatures. The derivative of the temperature with respect to the natural coordinates can be expressed as follows

$$\begin{cases} \dfrac{\partial T}{\partial L_1} = \dfrac{\partial T}{\partial x}\dfrac{\partial x}{\partial L_1} + \dfrac{\partial T}{\partial y}\dfrac{\partial y}{\partial L_1} + \dfrac{\partial T}{\partial z}\dfrac{\partial z}{\partial L_1} \\ \dfrac{\partial T}{\partial L_2} = \dfrac{\partial T}{\partial x}\dfrac{\partial x}{\partial L_2} + \dfrac{\partial T}{\partial y}\dfrac{\partial y}{\partial L_2} + \dfrac{\partial T}{\partial z}\dfrac{\partial z}{\partial L_2} \\ \dfrac{\partial T}{\partial L_3} = \dfrac{\partial T}{\partial x}\dfrac{\partial x}{\partial L_3} + \dfrac{\partial T}{\partial y}\dfrac{\partial y}{\partial L_3} + \dfrac{\partial T}{\partial z}\dfrac{\partial z}{\partial L_3} \end{cases} \tag{5.29}$$

Using the interpolation functions in Eq. 5.28, Eq. 5.29 can be rewritten in matrix form as follows:

$$\begin{pmatrix} \dfrac{\partial T}{\partial L_1} \\ \dfrac{\partial T}{\partial L_2} \\ \dfrac{\partial T}{\partial L_3} \end{pmatrix} = \begin{bmatrix} x_1 - x_4 & x_2 - x_4 & x_3 - x_4 \\ y_1 - y_4 & y_2 - y_4 & y_3 - y_4 \\ z_1 - z_4 & z_2 - z_4 & z_3 - z_4 \end{bmatrix} \begin{pmatrix} \dfrac{\partial T}{\partial x} \\ \dfrac{\partial T}{\partial y} \\ \dfrac{\partial T}{\partial z} \end{pmatrix} \tag{5.30}$$

The temperature gradient with respect the global coordinate system (x, y, z) is derived by inverting the matrix in Eq. 5.30.

$$\begin{pmatrix} \dfrac{\partial T}{\partial x} \\ \dfrac{\partial T}{\partial y} \\ \dfrac{\partial T}{\partial z} \end{pmatrix} = \frac{1}{|J|} \begin{bmatrix} b_{(1,1)} & b_{(1,2)} & b_{(1,3)} \\ b_{(2,1)} & b_{(2,2)} & b_{(2,3)} \\ b_{(3,1)} & b_{(3,2)} & b_{(3,3)} \end{bmatrix} \begin{pmatrix} \dfrac{\partial T}{\partial L_1} \\ \dfrac{\partial T}{\partial L_2} \\ \dfrac{\partial T}{\partial L_3} \end{pmatrix} \tag{5.31}$$

The coefficients $b_{(i,j)}$ are defined as follows:

$$b_{(1,1)} = (y_2 - y_4)(z_3 - z_4) - (y_3 - y_4)(z_2 - z_4)$$

$$
\begin{aligned}
b_{(1,2)} &= (y_3 - y_4)(z_1 - z_4) - (y_1 - y_4)(z_3 - z_4) \\
b_{(1,3)} &= (y_1 - y_4)(z_2 - z_4) - (y_2 - y_4)(z_1 - z_4) \\
b_{(2,1)} &= (x_3 - x_4)(z_2 - z_4) - (x_2 - x_4)(z_3 - z_4) \\
b_{(2,2)} &= (x_1 - x_4)(z_3 - z_4) - (x_3 - x_4)(z_1 - z_4) \\
b_{(2,3)} &= (x_2 - x_4)(z_1 - z_4) - (x_1 - x_4)(z_2 - z_4) \\
b_{(3,1)} &= (x_2 - x_4)(y_3 - y_4) - (x_3 - x_4)(y_2 - y_4) \\
b_{(3,2)} &= (x_3 - x_4)(y_1 - y_4) - (x_1 - x_4)(y_3 - y_4) \\
b_{(3,3)} &= (x_1 - x_4)(y_2 - y_4) - (x_2 - x_4)(y_1 - y_4)
\end{aligned}
\tag{5.32}
$$

The Jacobian determinant in Eq. 5.31 is equal to one sixth of the tetrahedron volume and it is defined as in Eq. 5.33.

$$
|J| = (x_1 - x_4)b_{(1,1)} + (y_1 - y_4)b_{(2,1)} + (z_1 - z_4)b_{(3,1)} = \frac{\delta \mathscr{V}}{6} \tag{5.33}
$$

In order to have a 3×4 matrix for $\mathbf{B}$, the matrix in Eq. 5.31 is multiplied by the matrix that defines the relationship among the four natural coordinates.

$$
\begin{aligned}
\mathbf{B} &= \frac{1}{|J|} \begin{bmatrix} b_{(1,1)} & b_{(1,2)} & b_{(1,3)} \\ b_{(2,1)} & b_{(2,2)} & b_{(2,3)} \\ b_{(3,1)} & b_{(3,2)} & b_{(3,3)} \end{bmatrix} \begin{bmatrix} 1 & 0 & 0 & -1 \\ 0 & 1 & 0 & -1 \\ 0 & 0 & 1 & -1 \end{bmatrix} = \\
&= \frac{1}{|J|} \begin{bmatrix} b_{(1,1)} & b_{(1,2)} & b_{(1,3)} & -(b_{(1,1)} + b_{(1,2)} + b_{(1,3)}) \\ b_{(2,1)} & b_{(2,2)} & b_{(2,3)} & -(b_{(2,1)} + b_{(2,2)} + b_{(2,3)}) \\ b_{(3,1)} & b_{(3,2)} & b_{(3,3)} & -(b_{(3,1)} + b_{(3,2)} + b_{(3,3)}) \end{bmatrix}
\end{aligned}
\tag{5.34}
$$

The definition of the $\mathbf{B}$ matrix in Eq. 5.34 confirms that the temperature gradient is constant through the element.

5.4.2 Surface integrals

The calculation of surface integrals involving the product of natural coordinates is particularly easy for the linear tetrahedron thanks to the following formula (see Grandin, 1986):

$$\int_{\delta\mathscr{A}} L_1^{\alpha} L_2^{\beta} L_3^{\gamma}\, da = 2\delta\mathscr{A} \frac{\alpha!\,\beta!\,\gamma!}{(\alpha+\beta+\gamma+2)!} \tag{5.35}$$

Two different situations are encounter in Eq. 5.21, 5.22 and 5.23:

$$\int_{\delta\mathscr{A}} \mathbf{N}^T\mathbf{N} da = \int_{\delta\mathscr{A}} \begin{bmatrix} L_1^2 & L_1L_2 & L_1L_3 & L_1L_4 \\ L_2L_1 & L_2^2 & L_2L_3 & L_2L_4 \\ L_3L_1 & L_3L_2 & L_3^2 & L_3L_4 \\ L_4L_1 & L_4L_2 & L_4L_3 & L_4^2 \end{bmatrix} da \tag{5.36}$$

$$\int_{\delta\mathscr{A}} \mathbf{N}^T da = \int_{\delta\mathscr{A}} \begin{bmatrix} L_1 \\ L_2 \\ L_3 \\ L_4 \end{bmatrix} da \tag{5.37}$$

Since the integrals in Eq. 5.36 and 5.37 are calculated over one element face, the associated natural coordinate is zero. If the Face 1 in Fig. 5.6 is considered, by applying the formula 5.35, Eq. 5.37 becomes

$$\int_{\delta\mathscr{A}_1} \mathbf{N}^T da = \int_{\delta\mathscr{A}_1} \begin{bmatrix} 0 \\ L_2 \\ L_3 \\ L_4 \end{bmatrix} da = \frac{2\delta\mathscr{A}_1}{3!} \begin{bmatrix} 0 \\ 1 \\ 1 \\ 1 \end{bmatrix} = \frac{\delta\mathscr{A}_1}{3} \begin{bmatrix} 0 \\ 1 \\ 1 \\ 1 \end{bmatrix} \tag{5.38}$$

and with similar considerations Eq. 5.36 results as follows:

$$\int_{\delta\mathscr{A}_1} \mathbf{N}^T\mathbf{N}da = \int_{\delta\mathscr{A}_1} \begin{bmatrix} 0 & 0 & 0 & 0 \\ 0 & L_2^2 & L_2L_3 & L_2L_4 \\ 0 & L_3L_2 & L_3^2 & L_3L_4 \\ 0 & L_4L_2 & L_4L_3 & L_4^2 \end{bmatrix} da = \frac{\delta\mathscr{A}_1}{6} \begin{bmatrix} 0 & 0 & 0 & 0 \\ 0 & 1 & 1/2 & 1/2 \\ 0 & 1/2 & 1 & 1/2 \\ 0 & 1/2 & 1/2 & 1 \end{bmatrix} \tag{5.39}$$

Analogous results are found for the other three faces of the element.

5.5 Finite element formulation of the thermal problem with the tetrahedron element

Thanks to the results presented in the previous sections the finite element formulation of the thermal problem in Eq. 5.20 can be formalized for the tetrahedron element.

Since the temperature-gradient interpolation matrix is constant (see Eq. 5.34), the integral which defines the conductive matrix $\mathbf{k}_{cd}$ can be easily calculated as follows:

$$\mathbf{k}_{cd} = \int_{\delta\mathscr{V}} \mathbf{B}^T\mathbf{C}\mathbf{B}\, dv = \frac{|J|}{6}\mathbf{B}^T\mathbf{C}\mathbf{B} \tag{5.40}$$

If the element has one or more faces associated with a convective boundary, the corresponding convective matrix $\mathbf{k}_{cv}$ can be calculated as in Eq. 5.39. For instance, with a convective boundary applied to Face 1, the thermal element stiffness matrix becomes

$$\mathbf{k}_T = \frac{|J|}{6}\mathbf{B}^T\mathbf{C}\mathbf{B} + \frac{h\delta\mathscr{A}_1}{6} \begin{bmatrix} 0 & 0 & 0 & 0 \\ 0 & 1 & 1/2 & 1/2 \\ 0 & 1/2 & 1 & 1/2 \\ 0 & 1/2 & 1/2 & 1 \end{bmatrix} \tag{5.41}$$

Otherwise, with only conduction $\mathbf{k}_T$ reduces to Eq. 5.40.

Also the calculation of the convection and applied heat boundary "force" vectors is particularly straightforward with the tetrahedron element. Assuming Face 1 to be the face where the boundary condition is applied, Eq. 5.22 and 5.23 become

$$\boldsymbol{q}_b = \int_{\delta\mathscr{A}} \mathbf{N}^T \boldsymbol{q_b} \boldsymbol{n}^T da = \frac{q_n \delta\mathscr{A}_1}{3} \begin{bmatrix} 0 \\ 1 \\ 1 \\ 1 \end{bmatrix} \tag{5.42}$$

$$\boldsymbol{q}_{cv} = h \int_{\delta\mathscr{A}} \mathbf{N}^T T_\infty da = \frac{h T_\infty \delta\mathscr{A}_1}{3} \begin{bmatrix} 0 \\ 1 \\ 1 \\ 1 \end{bmatrix} \tag{5.43}$$

Expression similar to Eq. 5.41 and 5.43 can be easily derived for the other element faces.

5.6 Solution scheme

The thermal analysis of the solid parts is carried out at the end of each revolution. The heat fluxes associated with the viscous dissipation in the fluid flow are therefore averaged as indicated in Eq. 5.44.

$$q_{avg} = \frac{1}{T} \int_T q(t)\, dt \approx \frac{1}{T} \sum_{i=1}^{n} q_i \delta t_i \tag{5.44}$$

In Eq. 5.44 is the total number of time steps and T is the time for one revolution; δt_i is the simulation time step, which can be constant or variable. Once the surface temperature of the solid bodies is available, the surface temperature field is interpolated from the structure to the fluid grid, in order to be applied as more precise boundary condition during the solution of the Energy equation.

The linear system of Eq. 5.24 is solved through the Conjugate Gradient method with ILDLT(0) preconditioner, since the global thermal stiffness matrix is symmetric and positive definite. Thanks to the finite elements formulation the thermal problem is linear and just a certain number of inner iterations of the Conjugate Gradient solver are required to obtained the temperature field in the solid parts.

6. CALCULATION OF THE ELASTIC DEFORMATION OF THE SOLID PARTS

In this chapter the methodology used to calculate the elastic deformation of the solid parts due to pressure and temperature loads are described. In the first two sections the finite element formulation for the solution of the linear elastic problem is introduced. Considerations about the constraints applied to the solid parts are presented in section 6.3. The influence method used for the fast computation of the solid bodies deformations in then described and the chapter ends with considerations about the correction of the film thickness with the deformation of the solid parts due to pressure and temperature loads.

6.1 Linear elastic deformation analysis and solution

The methodology used in this work to determine the deformation of the solid parts is based on the principle of the minimum potential energy. The principle of minimum potential energy states that among all the possible geometrical configurations that a body can assume, the true one, corresponding to the satisfaction of the stable equilibrium, is identified by a minimum value for the total potential energy.

A mathematical justification of the principle of minimum potential energy can be introduced through the principle of the virtual work. In particular, it can be shown that the total potential energy represents the functional for equilibrium elasticity problems (see Wang, 1953). The total potential energy Π is the sum of the strain energy U and the applied load potential energy V, as indicated in Eq. 6.1.

$$\Pi = U + V \tag{6.1}$$

When the variational form of a problem exist (i.e. the functional is defined) the problem can be approximately solved by defining a solution function $\tilde{\boldsymbol{u}}$ that minimizes the functional. The definition of $\tilde{\boldsymbol{u}}$ involves selecting a function that satisfies the boundary conditions and contains arbitrary constants, which are successively defined through the minimization process.

Under a general three dimensional stress state, the strain energy associated with an element of volume $\delta\mathscr{V}$ is defined by Eq. 6.2 (see Grandin, 1986).

$$U = \frac{1}{2}\int_{\delta\mathscr{V}} \boldsymbol{\epsilon}^T \boldsymbol{\sigma}\, dv \tag{6.2}$$

where $\boldsymbol{\epsilon}$ is the strain and $\boldsymbol{\sigma}$ the stress in the element. With points in a continuum having displacement components $\boldsymbol{u}$ with components u, v and w in the x, y and z directions respectively, the matrix form of the linear strain-displacement relationships is expressed by Eq.6.3.

$$\boldsymbol{\epsilon} = \boldsymbol{\epsilon}_F + \boldsymbol{\epsilon}_T = \begin{pmatrix} \epsilon_x \\ \epsilon_y \\ \epsilon_z \\ \gamma_{xy} \\ \gamma_{yz} \\ \gamma_{xz} \end{pmatrix} = \begin{bmatrix} \frac{\partial}{\partial x} & 0 & 0 \\ 0 & \frac{\partial}{\partial x} & 0 \\ 0 & 0 & \frac{\partial}{\partial x} \\ \frac{\partial}{\partial y} & \frac{\partial}{\partial x} & 0 \\ 0 & \frac{\partial}{\partial z} & \frac{\partial}{\partial y} \\ \frac{\partial}{\partial z} & 0 & \frac{\partial}{\partial x} \end{bmatrix} \begin{pmatrix} u \\ v \\ w \end{pmatrix} \tag{6.3}$$

In Eq. 6.3, $\boldsymbol{\epsilon}$ represents the total strain vector, $\boldsymbol{\epsilon}_F$ is the elastic strain due to the applied loads and $\boldsymbol{\epsilon}_T$ is the temperature induced strain. The temperature induced strains are associated with the expansion or contraction observed in a solid body when it undergoes a temperature change ΔT with respect to a reference temperature

T_0; the temperature induced strain can be expressed though the coefficient of linear expansion α_T as indicated in Eq. 6.4.

$$\boldsymbol{\epsilon}_T = \begin{pmatrix} \epsilon_x \\ \epsilon_y \\ \epsilon_z \\ \gamma_{xy} \\ \gamma_{yz} \\ \gamma_{xz} \end{pmatrix} = \begin{pmatrix} \alpha_T \Delta T \\ \alpha_T \Delta T \\ \alpha_T \Delta T \\ 0 \\ 0 \\ 0 \end{pmatrix} \tag{6.4}$$

The stress in the continuum is defined in therm of the elastic strain $\boldsymbol{\epsilon}_F$ through the constitutive matrix $\mathbf{C}$:

$$\boldsymbol{\sigma} = \mathbf{C}\boldsymbol{\epsilon}_F = \mathbf{C}\left(\boldsymbol{\epsilon} - \boldsymbol{\epsilon}_T\right) \tag{6.5}$$

In the case of an elasticity problem, the constitutive matrix for an isotropic material is defined as follows:

$$\mathbf{C} = \frac{E}{(1-\nu)(1-2\nu)} \begin{bmatrix} 1-\nu & \nu & \nu & 0 & 0 & 0 \\ \nu & 1-\nu & \nu & 0 & 0 & 0 \\ \nu & \nu & 1-\nu & 0 & 0 & 0 \\ 0 & 0 & 0 & \frac{1-2\nu}{2} & 0 & 0 \\ 0 & 0 & 0 & 0 & \frac{1-2\nu}{2} & 0 \\ 0 & 0 & 0 & 0 & 0 & \frac{1-2\nu}{2} \end{bmatrix} \tag{6.6}$$

where E is the elastic modulus and ν the Poisson's ratio of the material. Likewise in the case of the thermal problem, a strain-displacement $\mathbf{B}$ matrix can be defined also for the elastic problem, which expresses the strain in the element as a function of the nodal displacement:

$$\boldsymbol{\epsilon} = \mathbf{B}\boldsymbol{u}_i \tag{6.7}$$

With the definition in Eq. 6.7 the total strain energy associated with an element of volume $\delta\mathscr{V}$ can be rewritten as in Eq. 6.8.

$$U = \frac{1}{2}\int_{\delta\mathscr{V}} \left(\mathbf{B}\boldsymbol{u}_i - \boldsymbol{\epsilon}_T\right)^T \mathbf{C}\left(\mathbf{B}\boldsymbol{u}_i - \boldsymbol{\epsilon}_T\right)\, dv \tag{6.8}$$

It should be noticed that in Eq. 6.8 just the elastic strain has been included, because the potential energy associated with the thermal strain is just a constant, determined by the temperature field of the body. In order to complete the definition of the potential energy, the nodal force potential energy V has to be determined. Since in this work are considered only forces which magnitude that is not a function of the force displacement, the associated potential energy is simply the scalar product of the nodal force $\boldsymbol{f}_i$ and the displacement vector $\boldsymbol{u}_i$: [1]

$$V = -\boldsymbol{u}^T \boldsymbol{f}_i \tag{6.9}$$

By substituting Eq. 6.8 and 6.9 into Eq. 6.1, the total potential energy can be expressed as follows:

$$\Pi = \frac{1}{2} \int_{\delta \mathscr{V}} \left(\mathbf{B}\boldsymbol{u}_i - \boldsymbol{\epsilon}_T\right)^T \mathbf{C} \left(\mathbf{B}\boldsymbol{u}_i - \boldsymbol{\epsilon}_T\right) dv - \boldsymbol{u}_i^T \boldsymbol{f} \tag{6.10}$$

Equation 6.10 represents the functional that has to be minimized in order to define the approximated solution function. The functional is minimized as a function of the approximate solution's parameters, i.e. the nodal displacement: by differentiating Eq. 6.10 with respect $\boldsymbol{u}_i$, and setting the resulting equations equal to zero, the matrix form of the elasticity equation is obtained:

$$\int_{\delta \mathscr{V}} \mathbf{B}^T \mathbf{C} \mathbf{B} \, dv \, \boldsymbol{u}_i = \int_{\delta \mathscr{V}} \mathbf{B}^T \mathbf{C} \boldsymbol{\epsilon}_T \, dv + \boldsymbol{f}_i \tag{6.11}$$

The integral on the left hand side represents the element stiffness matrix $\mathbf{k}$ and the integral on the right hand side the loads associated with the temperature-induced strain, thus Eq. 6.11 can be rewritten in the compact form as follows:

$$\mathbf{k}\boldsymbol{u}_i = \boldsymbol{f}_T + \boldsymbol{f}_i \tag{6.12}$$

Equation 6.12 represents the working force deflection equation for the element and is the base of the finite element method implemented. The when the analysis is

[1] a minus sign is required because the potential is the the negative of the work done by the force

extended to all the elements used to discretized the continuum, Eq. 6.12 has to be extended for the whole system

$$\mathbf{K}\boldsymbol{u}_i = \boldsymbol{F}_T + \boldsymbol{F}_i \tag{6.13}$$

In Eq. 6.13, the sparse matrix $\mathbf{K}$ is the global stiffness matrix (also in this case $\mathbf{K}$ is symmetric and positive definite) and $\boldsymbol{F}_T$ and $\boldsymbol{F}_i$ are the total loads on the structure, determined by the applied nodal loads and by the temperature-induced strains.

Each node has three degrees of freedom because the displacement $\boldsymbol{u}$ has three components u, v and w; the size of the stiffness matrix is hence three times the number of nodes. However, when a so called essential boundary condition is specified (meaning that the displacement of one or more nodes is constrained to a certain value) the size of the stiffness matrix decreases because the lines and columns associated with the constrained degrees of freedom are eliminated; it can be concluded that the size of the linear system 6.13 will always be less or at most equal to three times the number of nodes. For these reasons the assembly process involved in the definition of the global stiffness matrix $\mathbf{K}$ is more complicated than the case of the thermal stiffness matrix; additional details can be found in Grandin (1986).

6.2 Finite element formulation of the linear elastic problem with the tetrahedron element

As for the heat transfer problem, the tetrahedron makes the formulation of Eq. 6.13 straightforward. The strain-displacement matrix can be derived with a procedure similar to the one illustrated in section 5.4.1; for the linear elastic problem $\mathbf{B}$ has the following form:

$$\mathbf{B} = \frac{1}{|J|}\begin{bmatrix} b_1 & 0 & 0 & b_2 & 0 & 0 & b_3 & 0 & 0 & b_4 & 0 & 0 \\ 0 & b_{(2,2)} & 0 & 0 & b_{(2,5)} & 0 & 0 & b_{(2,8)} & 0 & 0 & b_{(2,11)} & 0 \\ 0 & 0 & b_{(3,3)} & 0 & 0 & b_{(3,6)} & 0 & 0 & b_{(3,9)} & 0 & 0 & b_{(3,12)} \\ b_{(4,1)} & b_{(4,2)} & 0 & b_{(4,4)} & b_{(4,5)} & 0 & b_{(4,7)} & b_{(4,8)} & 0 & b_{(4,10)} & b_{(4,11)} & 0 \\ 0 & b_{(5,2)} & b_{(5,3)} & 0 & b_{(5,5)} & b_{(5,6)} & 0 & b_{(5,8)} & b_{(5,9)} & 0 & b_{(5,11)} & b_{(5,12)} \\ b_{(6,1)} 0 & 0 & b_{(6,3)} & b_{(6,4)} & 0 & b_{(6,6)} & b_{(6,7)} & 0 & b_{(6,9)} & b_{(6,10)} & 0 & b_{(6,12)} \end{bmatrix} \tag{6.14}$$

The value of the entries populating the strain-displacement matrix are defined as follows:

$$
\begin{aligned}
b_{(1,1)} &= b_{(4,2)} = b_{(6,3)} = (y_2 - y_4)(z_3 - z_4) - (y_3 - y_4)(z_2 - z_4) \\
b_{(1,4)} &= b_{(4,5)} = b_{(6,6)} = (y_3 - y_4)(z_1 - z_4) - (y_1 - y_4)(z_3 - z_4) \\
b_{(1,7)} &= b_{(4,8)} = b_{(6,9)} = (y_1 - y_4)(z_2 - z_4) - (y_2 - y_4)(z_1 - z_4) \\
b_{(1,10)} &= b_{(4,11)} = b_{(6,12)} = -\left(b_{(1,1)} + b_{(1,4)} + b_{(1,7)}\right) \\
b_{(2,2)} &= b_{(4,1)} = b_{(5,3)} = (x_3 - x_4)(z_2 - z_4) - (x_2 - x_4)(z_3 - z_4) \\
b_{(2,5)} &= b_{(4,4)} = b_{(5,6)} = (x_1 - x_4)(z_3 - z_4) - (x_3 - x_4)(z_1 - z_4) \\
b_{(2,8)} &= b_{(4,7)} = b_{(5,9)} = (x_2 - x_4)(z_1 - z_4) - (x_1 - x_4)(z_2 - z_4) \\
b_{(2,11)} &= b_{(4,10)} = b_{(5,12)} = -\left(b_{(2,2)} + b_{(2,5)} + b_{(2,8)}\right) \\
b_{(3,3)} &= b_{(5,2)} = b_{(6,1)} = (x_2 - x_4)(y_3 - y_4) - (x_3 - x_4)(y_2 - y_4) \\
b_{(3,6)} &= b_{(5,5)} = b_{(6,4)} = (x_3 - x_4)(y_1 - y_4) - (x_1 - x_4)(y_3 - y_4) \\
b_{(3,9)} &= b_{(5,8)} = b_{(6,7)} = (x_1 - x_4)(y_2 - y_4) - (x_2 - x_4)(y_1 - y_4) \\
b_{(3,12)} &= b_{(5,11)} = b_{(6,10)} = -\left(b_{(3,3)} + b_{(3,6)} + b_{(3,9)}\right)
\end{aligned}
\tag{6.15}
$$

The tetrahedron has linear shape functions and the strain is constant throughout the element, as confirmed by Eq. 6.15; the integration required to obtain the element stiffness matrix is therefore easy.

$$
\mathbf{k} = \int_{\delta\mathscr{V}} \mathbf{B}^T\mathbf{C}\mathbf{B}\, dv = \frac{|J|}{6}\mathbf{B}^T\mathbf{C}\mathbf{B} \tag{6.16}
$$

The same consideration applies for the thermal load: the integral on the right hand side of Eq. 6.11 is simply

$$
\boldsymbol{f}_T = \int_{\delta\mathscr{V}} \mathbf{B}^T\mathbf{C}\boldsymbol{\epsilon}_T\, dv = \frac{|J|}{6}\mathbf{B}^T\mathbf{C}\boldsymbol{\epsilon}_T \tag{6.17}
$$

Combining Eq. 6.16 and 6.17 the working force deflection for the tetrahedron element is obtained

$$
\frac{|J|}{6}\mathbf{B}^T\mathbf{C}\mathbf{B}\boldsymbol{u}_i = \frac{|J|}{6}\mathbf{B}^T\mathbf{C}\boldsymbol{\epsilon}_T + \boldsymbol{f}_i \tag{6.18}
$$

Equations like 6.18 are defined for all the tetrahedra discretizing the continuum and assemble together to define the sparse linear system of Eq. 6.13.

6.3 Boundary conditions

For this type of problem the boundary conditions in represent a mechanical constraint which prevent any rigid body motion that would be determined by the external load condition. There is actually an important difference between a thermal and a pressure deformation analysis in this regard.

6.3.1 Deformation due to temperature loads

In this case the thermal load contributes just to an expansion of the solid part and the net load imbalance is zero, therefore there is no physical need to apply any constraint in order to solve the problem. However a "virtual" boundary condition is beneficial in order to make the linear system of Eq. 6.13 solvable in a numerical meaning. When just thermal loads are applied to the solid part, Eq. 6.13 becomes

$$\mathbf{K}\boldsymbol{u}_i = \boldsymbol{F}_T \tag{6.19}$$

The condition that has to be enforced is that the overall displacement has to be zero, as indicated in Eq. 6.20.

$$\begin{cases} u_1 + u_2 + \ldots + u_n = 0 \\ v_1 + v_2 + \ldots + v_n = 0 \\ w_1 + w_2 + \ldots + w_n = 0 \end{cases} \tag{6.20}$$

The system in Eq. 6.21 can be rewritten by adding this condition as follows.

$$\left[\begin{array}{cccccccccc|ccc}
 & & & & & & & & & & 1 & 0 & 0 \\
 & & & & & & & & & & 0 & 1 & 0 \\
 & & & & & & & & & & 0 & 0 & 1 \\
 & & & & & & & & & & 1 & 0 & 0 \\
 & & & & & \mathrm{K} & & & & & 0 & 1 & 0 \\
 & & & & & & & & & & 0 & 0 & 1 \\
 & & & & & & & & & & & \vdots & \\
 & & & & & & & & & & 1 & 0 & 0 \\
 & & & & & & & & & & 0 & 1 & 0 \\
 & & & & & & & & & & 0 & 0 & 1 \\
\hline
1 & 0 & 0 & 1 & 0 & 0 & & 1 & 0 & 0 & 0 & 0 & 0 \\
0 & 1 & 0 & 0 & 1 & 0 & \cdots & 1 & 0 & 0 & 0 & 0 & 0 \\
0 & 0 & 1 & 0 & 0 & 1 & & 0 & 0 & 1 & 0 & 0 & 0
\end{array}\right]
\left(\begin{array}{c}
u_1 \\ v_1 \\ w_1 \\ u_2 \\ v_2 \\ w_2 \\ \vdots \\ u_n \\ v_n \\ w_n \\ \hline \lambda_x \\ \lambda_y \\ \lambda_z
\end{array}\right)
=
\left(\begin{array}{c}
F_{Tx_1} \\ F_{Ty_1} \\ F_{Tz_1} \\ F_{Tx_2} \\ F_{Ty_2} \\ F_{Tz_2} \\ \vdots \\ F_{Tx_n} \\ F_{Ty_n} \\ F_{Tz_n} \\ \hline 0 \\ 0 \\ 0
\end{array}\right) \tag{6.21}$$

The displacement $(\lambda_x, \lambda_y, \lambda_z)$ can be thought as the displacement of the center of gravity of the solid body. If the problem is well posed (i.e. there is no load imbalance) it will result in a null vector after the solution of the linear system. Actually in order to have the new entries of the same order of magnitude of the others in the stiffness matrix (and thereby prevent numerical problems), the average value of $\boldsymbol{K}$ is used instead of 1 in the two blocks on the bottom left and top right. This method has been presented in Gockel (1999) and utilized also by Schenk (2013) for solving the same problem in the slipper swash plate interface.

6.3.2 Deformation due to pressure loads

In the case of pressure deformation analysis a load imbalance will most likely be present. A physical constraint, or essential boundary conditions, shall be specify to make the stiffness matrix non singular and allow the linear system of Eq. 6.13 to be solved. The drawback in this mathematical requirement is that the solid body has

always to be constrained to obtain a solution, but the rotating kit of axial piston machines is design with many parts that are just partially constrained or not constrained at all, because they have to be free of adjusting their position in order to balance the applied external loads through the pressure field in the lubricating interfaces. For this reason previous researchers, like for example Pelosi (2012) introduced a "constraint free" methodology based on the application of an inertial field able to eliminate the load imbalance on the structure. This method can be effective and may replicate in a reasonable way the actual behavior of some of the parts in the rotating kit, like for example the pistons but it can also lead to unreasonable results in some situations. For the valve plate and cylinder block mechanical constraints are more recommended.

The valve plate it is usually mechanically fixed to the end case; there are many different design though and in some situations the problem may become more complicated. For example, there are designs where the valve plate is a thin plate of a few mm thickness[2] or other situation where the valve plate does not have any mechanical constrains but is just placed on the end case or, the worst case, a combination of the two. In such situations the end case has to be introduced in the analysis, because its deformation has a major impact on the deformation of the sealing surface of the valve plate. Furthermore, when the valve plate is not mechanically constrained to the end case a contact problem between the two bodies should to be solved; additional details in this case are discussed in Sec. 6.7.

The cylinder block is mounted on the shaft through a spline joint and the part is allowed to move in axial direction and also it has some freedom of rotation (ideally with respect to the the point O of Fig. 2.5) in the x and y directions. When the machine operates the external loads on the cylinder block described in section 2.2 are balanced by the pressure field acting o the sealing surface. The spline joint doesn't play any role in this regard because it just transfers torque in the axial direction. For

[2]this is usually done to make the valve plate easily interchangeable so that valve plates optimized for different applications can be used on the same type of unit without major changes in the overall design.

this reason, constraining the block on the splined surface, should have a negligible impact on the deformation of the sealing surface.

6.4 Influence method for pressure deformation

The elastic deformation of the solid parts due to pressure loads has to be recalculated every time that the pressure changes and this happen continuously in time, because the pressure field has to meet the oscillating loads represented in Fig. 2.21. The computation time required for the solution of the Reynolds equation is of the order of magnitude of tenth of second, whereas the elastic deformation analysis takes a few minutes to be completed, making the overall simulation time unacceptable; in order to solve this problem an off-line approach was introduced.

In the case of the cylinder block valve plate interface the pressure loads that have to be considered are represented in Fig. 6.1. Both the cylinder block and

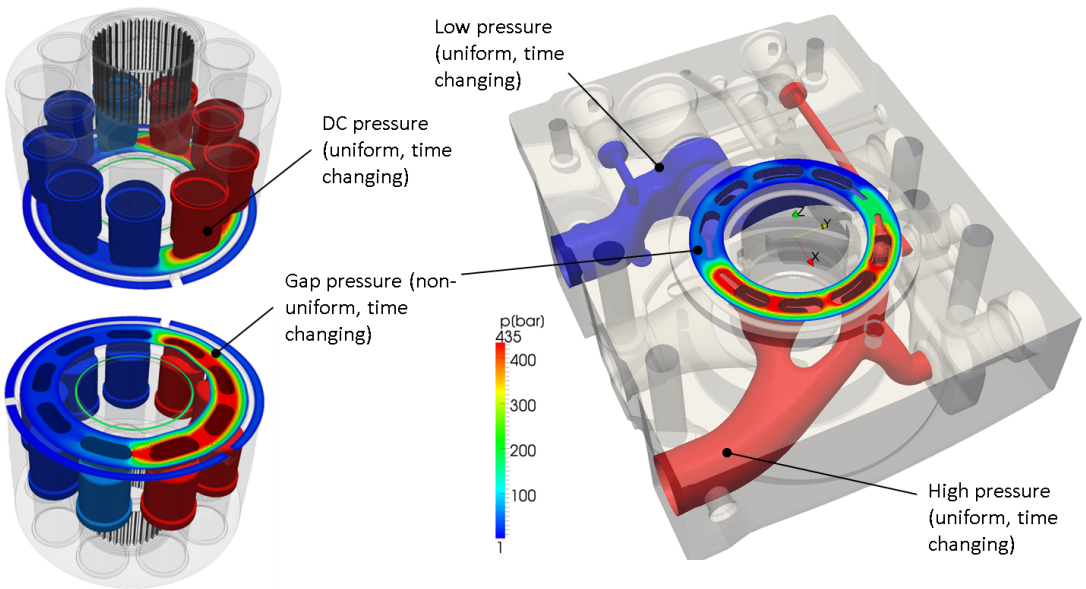

Fig. 6.1. Pressure loads on cylinder block, valve plate and end case bodies.

valve plate bodies are loaded with the non uniform pressure field in the lubricant, calculated through the Reynolds equation. The cylinder block is also loaded with

uniform pressure fields on the displacement chambers and low and high pressure ports surfaces, as indicated in Fig. 6.1.

The off-line calculation method is based on the superimposition principle and characterizes the deformation of the solid parts for an arbitrary load condition through the definition of a certain number of influence matrices. An influence matrix, **IM**, represents the deformation of the solid part associated with a reference pressure load applied on a certain area; in other words, the influence matrix represents the influence that a reference load applied on an certain area has on the overall body deformation.

In the case of a uniform pressure load, just one influence matrix is required to characterize the deformation of the solid part; the area of influence will be the total area where the pressure load is applied. The actual deformation can be obtained just by scaling the deformation stored in the influence matrix as indicated in Eq. 6.22

$$\mathbf{u} = \frac{p_i}{p_{ref}}\mathbf{IM} \tag{6.22}$$

Where p is the actual pressure load and p_{ref} the reference pressure used to determine the influence matrix **IM**. Eq. 6.22 is valid because the deformation are abundantly in the elastic region of the stress-strain characteristic of the materials. Eq. 6.22 can be used to calculate the deformation of the parts due to pressure in the displacement chambers, valve plate and end case ports and area of action of the spring.

To model the non uniform pressure load on the surfaces bounding the lubricating interface, the approach is to think about the non uniform pressure field as it was composed of a very large number of uniform pressure regions, characterized by an ideally infinitesimal area. By applying the superimposition principle, the total deformation associated with the non uniform pressure field is obtained by summing the contributions of each influence area as follows:

$$\mathbf{u} = \sum_{i=1}^{n} \frac{p_i}{p_{ref}}\mathbf{IM}_i \tag{6.23}$$

In Eq. 6.23, **u** is the overall displacement of the solid body associated with the non uniform pressure field; the summation goes throughout the n small elements used to

discretize the loaded surface, p_i is the pressure on the influence area i and p_{ref} is the reference pressure used to calculate the influence matrix $\mathbf{IM}_i$; a reference value of 100 bar was chosen. Practically speaking, after meshing the two solid bodies with tetrahedral elements, the triangular faces belonging to gap's bounding surfaces are loaded in sequence to define the two sets of influence matrices; to ensure a reasonable level of accuracy, a number of matrices between 5000 and 10000 is usually generated for each set. Furthermore, the modification on the film thickness due to the deformation of the solid parts can be operated just by knowing how the surfaces defining the interface deform in axial direction; thus, the influence matrices used in the simulation model store just that information, saving space and computation time.

Figure 2.5 depicts two examples of influence matrices relative to the cylinder block body. In Fig. 6.2(a) is represented the influence matrix relative to one of the faces

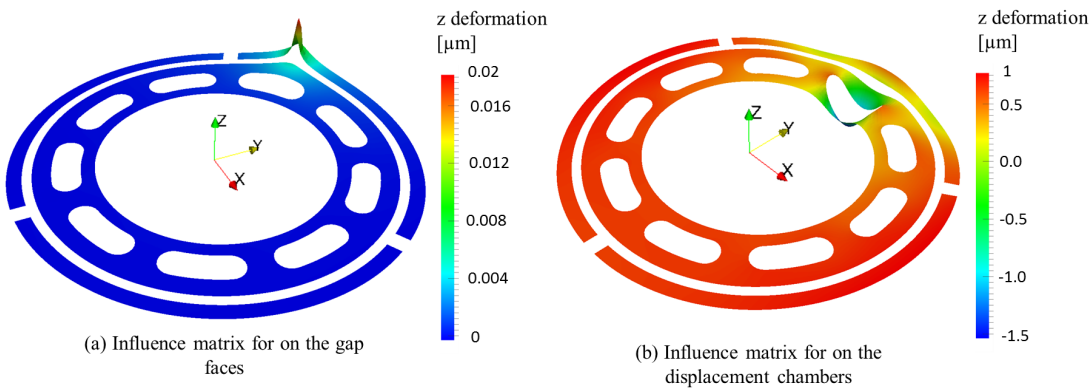

Fig. 6.2. Example of influence matrices (a) for one of the faces used to discretize the cylinder block's surface bounding the lubricating interface and (b) for one of the displacement chamber.

used to discretize the cylinder block's surface in contact with the oil; the scaling factor is 10^6:1 because the deformation in the matrix is very small, being associated with a pressure of 100 bar applied on a very small area. Fig.6.2(b) depicts the influence matrix relative to one of the displacement chamber, loaded with the same reference pressure of 100 bar; the scaling factor is 10^4:1 in this case. The deformation of the surface is mainly localized around the kidney opening and is negative because

the cylinder block is pushed towards the valve plate by the displacement chamber pressure. Moreover it can be noticed from the positive value of deformation far away from the kidney opening, that the cylinder block also inclines downward; this is due to a cantilever effect related to the constrain condition at the spline surface. However when the actual system of pressure load is considered, this effect will be compensated by the pressure field acting on the opposite direction from the gap side.

6.5 Interpolation between fluid and structure grids

The coupling between fluid flow and elastic deformation of the solid parts is problematic for two reasons. First, the fluid flow is solved on a structure grid made up with quads and the elastic deformation of the parts is calculated on an unstructured grid of tetrahedra, where the interface between fluid and structure is defined through an unstructured grid of triangles; obviously the two grids don't match. Second, the fluid flow is solved through the finite volumes method and the elastic deformation is calculated with the finite elements method; this means that the pressure is known at the center of the fluid elements centroid and the deformation at the nodes of the triangles defining the surface of the structure. Moreover, in order to correct the film thickness used to solve the Reynolds equation the deformation has to be available at the centroids of the fluid cells.

The two problems described were solved through two different interpolation methods, following the steps below:

1. the pressure field is interpolated from the fluid elements centroid to the triangular faces defining the interface with the fluid on the structure, through a "cells to cells" interpolation;

2. the elastic deformation of the solid part is calculated;

3. the nodes displacement of the structure's surface defining the interface with the fluid are interpolated to the centroids of the fluid grid through a "nodes to cells interpolation"

The two interpolation schemes are illustrated in Fig. 6.4. With the "cells to cells" scheme, the value of the interpolated field at every triangular face, Φ_i, is calculated as a weighted average of the field value, ϕ_i, at the centroid of the intersected fluid elements, where the weights are the intersection areas A_i:

$$\Phi_i = \frac{1}{A} \sum_{i=1}^{n} \phi_i A_i \tag{6.24}$$

With the "nodes to cells" interpolation the value of the interpolated field at every fluid element centroid Φ_i is calculated using a linear interpolation of the nodal values ϕ_i of the triangle containing the centroid:

$$\Phi_i = Ax_i + By_i + C \tag{6.25}$$

Where x_i and y_i are the coordinates of the fluid element centroid; the interpolation coefficients are calculated by solving the linear system in Eq. 6.26

$$\begin{cases} Ax_0 + By_0 + C = \phi_0 \\ Ax_1 + By_1 + C = \phi_1 \\ Ax_2 + By_2 + C = \phi_2 \end{cases} \tag{6.26}$$

The interpolation coefficients in Eq. 6.24 and 6.26 are calculated just once in the pre-processing phase and are then stored for a fast computation every time that the interpolation is required.

6.6 Correction of the film thickness geometry with the elastic deformations

The lubricating film geometry is corrected with the elastic deformations of the solid parts through the two terms $\delta h_{CB}(r, \vartheta)$ and $\delta h_{VP}(r, \vartheta)$ in Eq. 2.25; the two

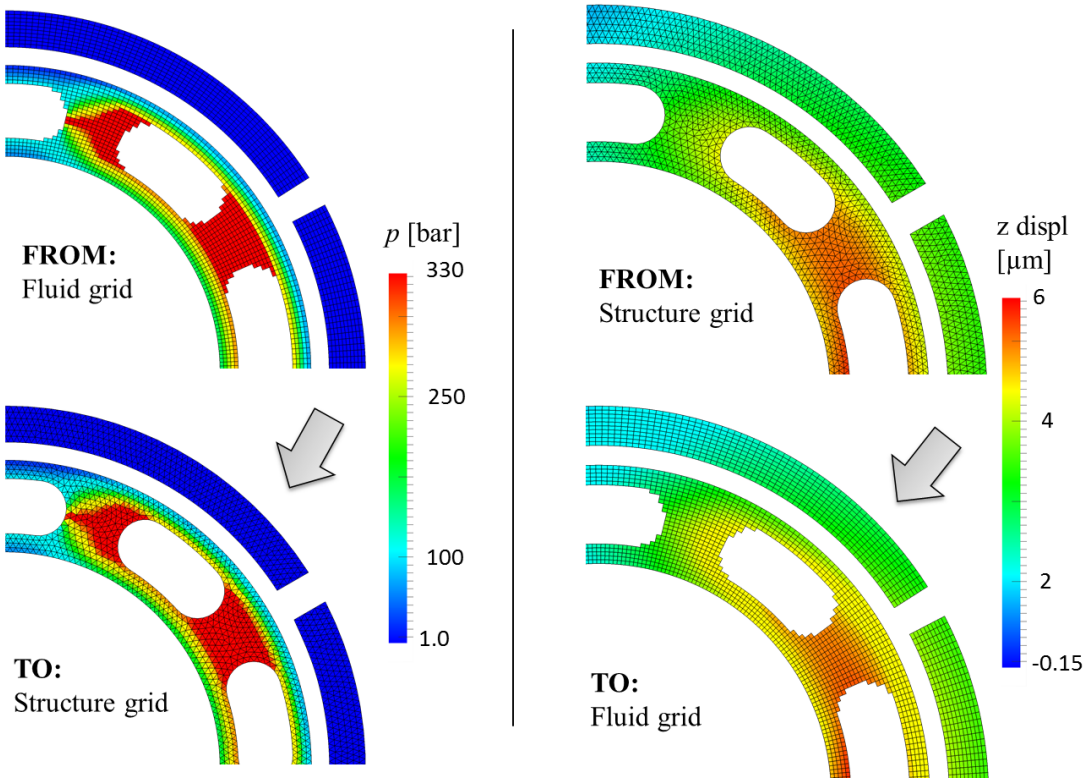

Fig. 6.3. Interpolations required to transfer pressure and elastic deformation fields from fluid to structure and vice versa.

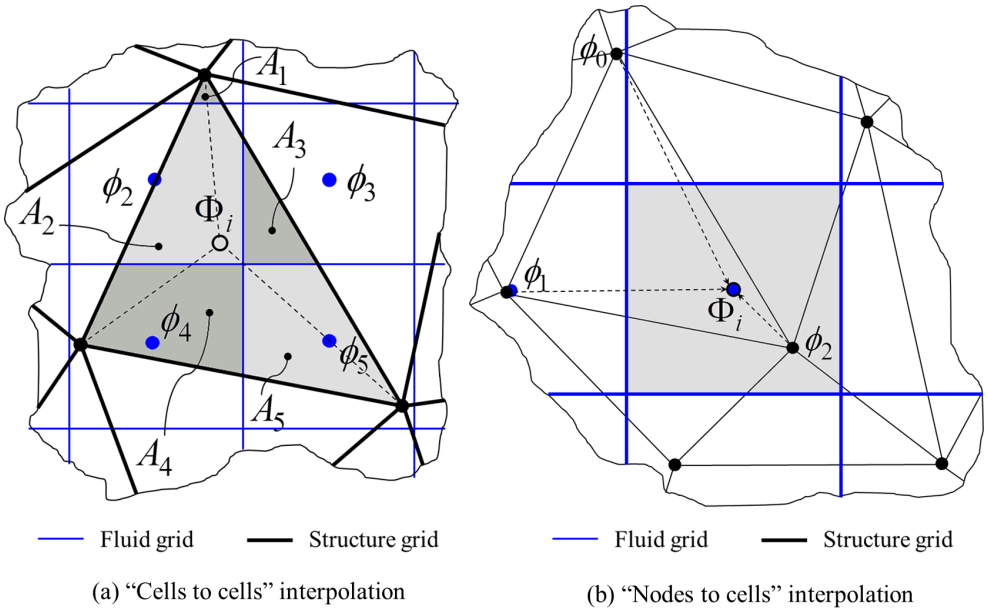

Fig. 6.4. "Cells to cells" and "nodes to cells" interpolation schemes.

corrections are defined by the sum of the elastic deformations due to pressure and thermal deflections:

$$\begin{cases} \delta h_{CB}(r,\vartheta) = \delta h^{p}_{CB}(r,\vartheta) + \delta h^{th}_{CB}(r,\vartheta) \\ \delta h_{VP}(r,\vartheta) = \delta h^{p}_{VP}(r,\vartheta) + \delta h^{th}_{VP}(r,\vartheta) \end{cases} \tag{6.27}$$

The corrections to the film thickness due to the pressure deformations of the two solid bodies are calculated directly from the influence matrices, as indicated in Eq. 6.28.

$$\begin{cases} \delta h^{p}_{CB}(r,\vartheta) = \sum_{i=1}^{n} \frac{p_i}{p_{ref}} \mathbf{IM}_i + \sum_{i=1}^{z} \frac{p_{DC,i}}{p_{ref}} \mathbf{IM}_{DC,i} + \frac{p_{S,i}}{p_{ref}} \mathbf{IM}_S \\ \delta h^{p}_{VP}(r,\vartheta) = \sum_{i=1}^{n} \frac{p_i}{p_{ref}} \mathbf{IM}_i + \frac{p_{LP}}{p_{ref}} \mathbf{IM}_{LP} + \frac{p_{HP}}{p_{ref}} \mathbf{IM}_{HP} \end{cases} \tag{6.28}$$

In Eq. 6.28, n is the number of faces used to discretize the bodies surface in contact with the lubricant, z is the number of pistons in the machine and the subscripts DC, LP, HP, S indicates respectively the displacement chamber, low pressure port, high pressure port and spring. The computation of Eq. 6.28 was parallelized through the `OpenMP` API, in order to minimize the solution time. On multi-core processors the time required to calculate Eq. 6.28 can be reduced to a few tens of milliseconds, making it of the same order of magnitude of the time required to solve the linear system in Eq. 4.17 during the fluid structure interaction convergence loop.

The thermal deflections are calculated just at the end of each revolution, when also the temperature fields in the solid parts are estimated; these deformations are typically of the order of magnitude of tens of microns. If the lubricating film is corrected directly with the thermal deformation of the two bounding surfaces the simulation will most likely fail, due to the penetration of the cylinder block surface into the valve plate surface. This problem was solved realizing that are not the overall bodies deflections that affect the lubricating film behavior, but just the relative change of the surfaces in contact with the lubricant. Indicating with $\boldsymbol{w}^{th}_{CB}$ and $\boldsymbol{w}^{th}_{VP}$ the overall axial thermal deformations of the cylinder block and valve plate surfaces in

contact with the lubricant, the relative thermal deformations used to correct the film thickness are defined as follows:

$$\begin{cases} \delta h_{CB}^{th}(r,\vartheta) = \left|\min\left\{\boldsymbol{w}_{CB}^{th}\right\} - \boldsymbol{w}_{CB}^{th}\right| \\ \delta h_{VP}^{th}(r,\vartheta) = -\left|\max\left\{\boldsymbol{w}_{VP}^{th}\right\} - \boldsymbol{w}_{VP}^{th}\right| \end{cases} \tag{6.29}$$

Figure 6.5 illustrates the temperature field in the cylinder block and valve plate for a

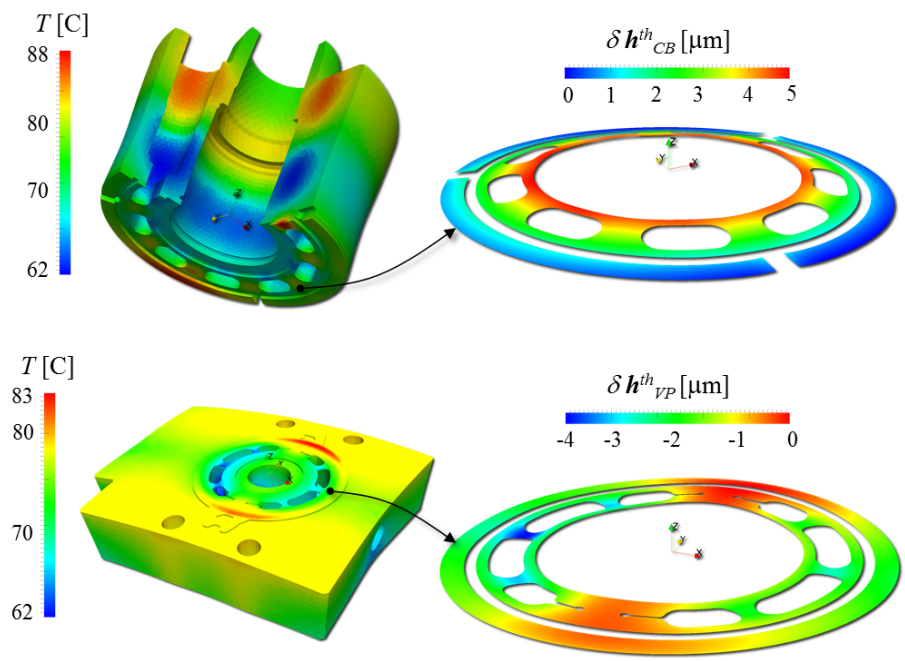

Fig. 6.5. Example of temperature field in the cylinder block and valve; the solid parts are warped with the thermal deflections with a scale of 1000:1. The relative deformations of the two surfaces in contact with the lubricant are shown on the right.

75 cc unit, at 1000 rpm and 300 bar differential pressure; the two bodies are warped using the associated thermal deflection, scaled 1000:1. The relative changes to the two surfaces in contact with the lubricant, $\delta h_{CB}^{th}(r,\vartheta)$ and $\delta h_{VP}^{th}(r,\vartheta)$, are shown on the right. It can be notice that, thanks to the definitions 6.29, the thermal deformations are ensured to be always positive for the cylinder block and negative for the valve plate; in this way any problem of possible penetration during the correction is solved.

6.7 Additional consideration about the calculation of the elastic deformation of the valve plate and end case assembly

The approach described in this chapter is based on the assumption that the elastic deformation of the solid parts is linear. Even though the magnitude of the elastic deformations associated with pressure and thermal loads are certainly in the elastic region of the stress-strain curve, in some cases the behavior of the valve plate and end case assembly can become non linear due to solid contact conditions. Figure 6.7 illustrates an example of design where a non-linear contact problem arises. Actually this design is fairly common in axial piston units of commercial production and it is worth to discuss its analysis in this section.

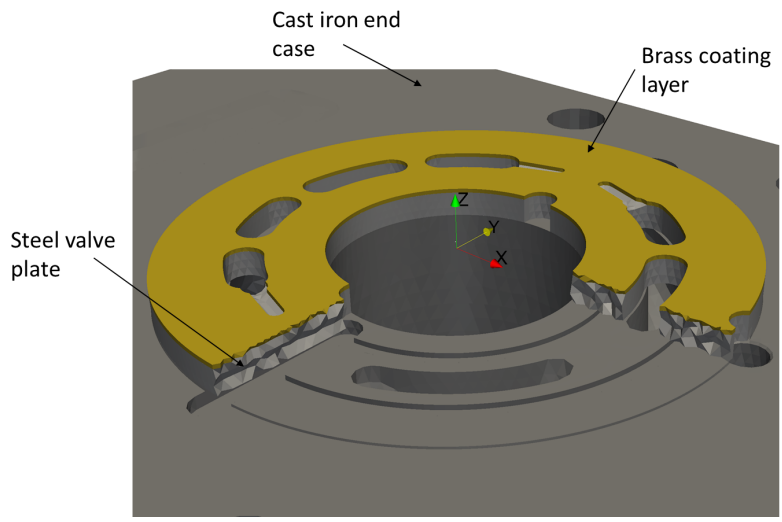

Fig. 6.6. Thermal deflection of the valve plate and end case assembly.

The valve plate is a few mm thick steel plate coated with a thin bronze layer; the end case is instead made of cast iron. There is no mechanical connection between valve plate and end case except a little pin on the outer region of the valve plate. The pin prevents the valve plate from rotating around the z axis but it allows a translation in z direction, which might eventually lead the valve plate to slightly detach from the end case.

The solid contact between the valve plate and the end case is a problem that theoretically can not be modeled rigorously with the approach developed in this work. The linear elastic theory described in Sec. 6.1 is not able to handle solid contact problems; moreover even if a more sophisticated non-liner approach were to be developed, the influence method described in section 6.4 could not be applied because it is based on the superimposition principle, which rely on the hypothesis of linear behavior of the structure. Furthermore, the valve plate is bi-metal and its thermal behavior is different from the end case. More precisely, the thermal deflection of the bi-metal valve plate is greater than the thermal deflection of the end case and since there is no physical constrain between the two solids, a gap in between may be generated. The situation is illustrated in Fig. 6.7: the contour represents a reasonable temperature field in the bi-metal valve plate and end case during operation (calculated through the simulation model) and the two bodies are warped with the associated thermal deflection, with a scale of 1000:1.

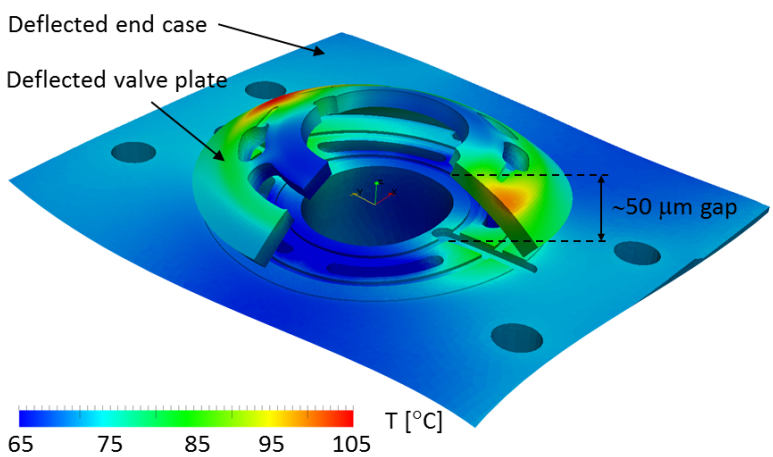

Fig. 6.7. The contour represents a reasonable temperature field in the bi-metal valve plate and end case during operation. The two bodies are warped with the associated thermal deflection, with a scale of 1000:1. A gap of 50 μm is present when the valve plate is not loaded with any pressure.

Without any applied pressure, a gap of about 50 μm develops between the two solid parts because the valve plate deforms into a convex shape and detaches from the end case. When pressure starts to rise in the unit, the pressure field in the fluid film pushes the valve plate down from the top; however, on the other hand oil starts to leak from the high pressure port of the end case through the gap beneath the valve plate. The pressure field determined by the leakage is purely hydrostatic whereas the pressrue field in the fluid film on the top of the valve plate is a combination of hydrostatic and hydrodynamic components. In order to prevent the valve plate from popping out, the area where the hydrostatic pressure field is generated beneath it has been design such that the pushing force from the bottom will always be smaller than the pressing force on the top, associated with the pressure field in the lubricating interface.

The question is how the valve plate deforms when pressure is applied. In the configuration illustrated in Fig. 6.7 the valve plate is quite compliant and it is reasonable to expect that even low pressures are able to flatten it back on the end case body. It is not easy to determine the minimum pressure to achieve that result though, considering that there is a pushing force from the bottom deriving from the hydrostatic pressure field at the interface with the end case. The next section describes in details how the described problems can be addressed.

6.7.1 Solid contact problem between valve plate and end case

The solid contact problem between valve plate and end case has been studied through a commercial finite element software. Figure 6.8 depicts the pressure loads applied on the assembly. The two ports in the end case were loaded with uniform pressure fields equal to the low and high pressure levels. The pressure on the top of the valve plate was obtained by averaging the pressure field that balanced the external loads on the cylinder block over one shaft revolution. The pressure on the bottom of the valve plate was calculated by solving the Laplace equation $\boldsymbol{\nabla}^2 p = 0$ on the

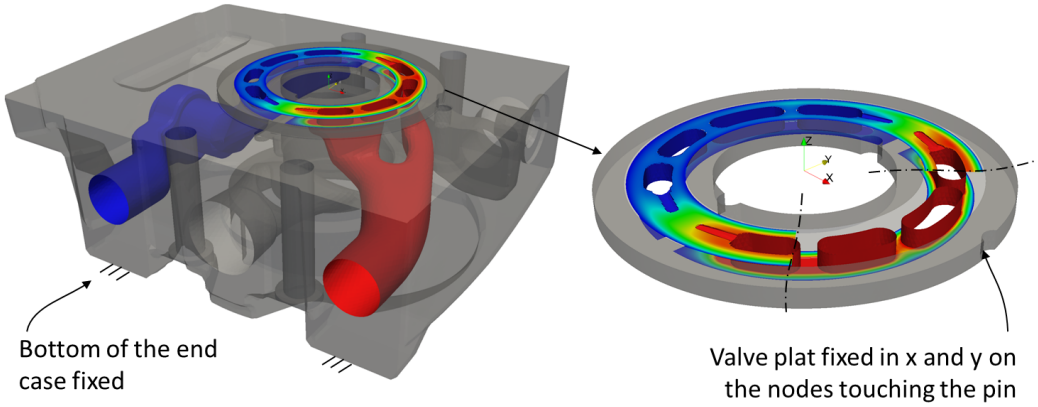

Fig. 6.8. Pressure loads on the valve plate and end case assembly considering the thermal deflection of the parts.

interface between valve plate and end case. The valve plate was fixed on the x and y directions on the nodes touching the pin on the outer surface but it was free to move anywhere else; a sliding contact interface was defined on the area shared by valve plate and end case. The end case instead was fixed in all directions on the bottom surface.

More problematic is the situation when thermal loads are also included. As described in Sec. 6.3.1, if only thermal loads are considered there will be no load imbalance and no need to apply any essential boundary condition. When thermal loads are combined with pressure loads though, a physical constrain must be applied to solve the problem. However, the physical constrain necessary for the loads deriving from pressure will have a negative impact on the calculation of the thermal deflection because it will force the part to deflect in an unnatural way. The problem has been solved by calculating the thermal deflection before any pressure deformation analysis; after being calculated, the thermal deformation has been used to modify the nodes position in the mesh. Since the contact algorithm available in the commercial FEM software is formulated through a penalty method based on the penetration of the nodes of a "slave" body into a "master" body the idea of embedding the effect of the thermal deflection directly in the mesh used to calculate the pressure deformation can

actually work quite well. Figure 6.9 shows the detail of the mesh warped with the thermal deflection; it can be noticed how the valve plate detaches on its inner radius whereas it touches the end case on the outer region.

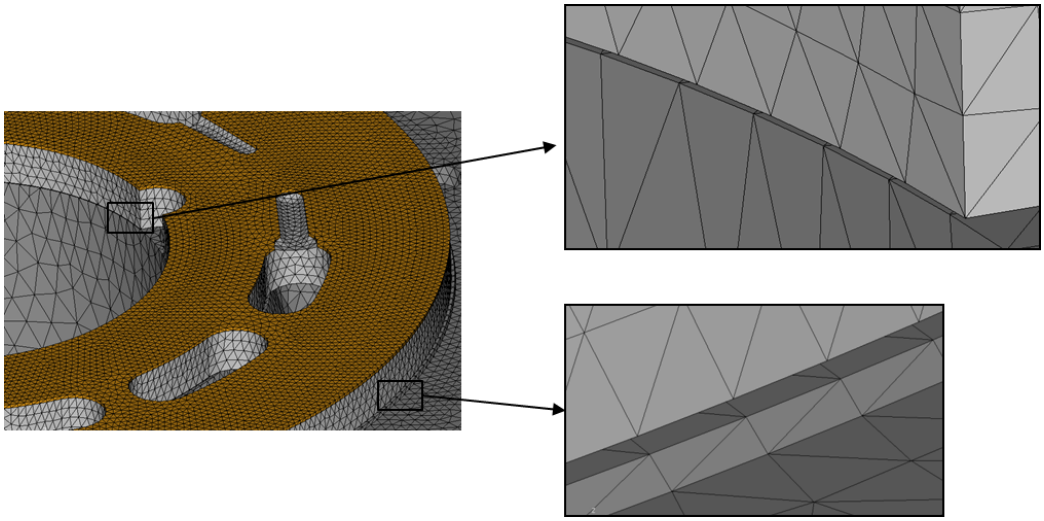

Fig. 6.9. Representation of the mesh of the valve plate end case assembly warped with the thermal deflection.

The solid contact analysis has been carried out for a number of differential pressures, $\Delta p = 50, 200, 400$ bar; the low pressure was always fixed at 25 bar. Figure 6.10 illustrates an example of the solution in terms of contour of the displacement in z direction for $\Delta p = 200$ bar. The contour shows that even though the applied pressure fields were definitely non symmetric with respect to the y axis, the valve plate deforms more or less with an axisymmetric pattern. Moreover, all the analysis have confirmed that the applied pressure fields was sufficient to flatten the valve plate back on the end case and thereby to eliminate the original gap associated with the thermal deflection. Nonetheless, even though the deflection of the valve plate is somehow canceled by the pressure deformation, the thermal deflection of the end case still plays a role because the valve plate is pushed over it by the pressure field.

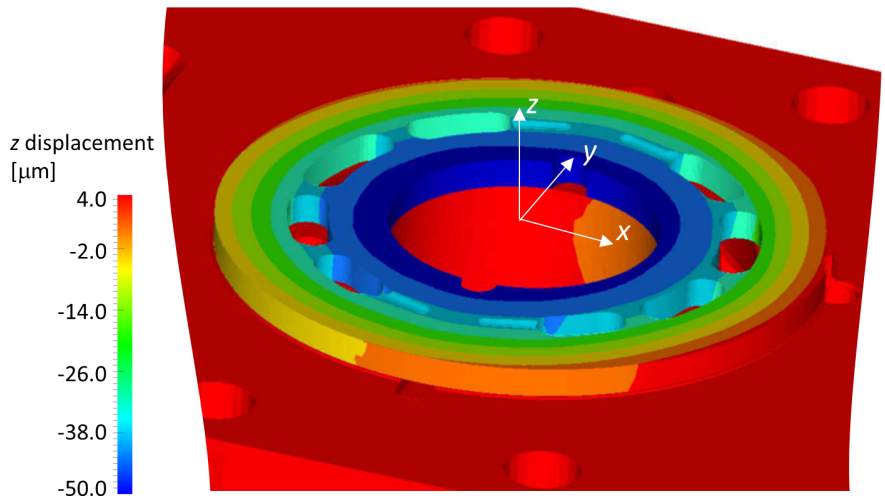

Fig. 6.10. Contour representing the displacement in z direction of the valve plate and end case assembly. The solution was found for a differential pressure of 200 bar.

6.7.2 Linear model approach for the pressure and thermal deformation analysis of the valve plate and end case assembly

Now that the overall deformation behavior of the valve plate and end case assembly is known the question is how to approximate such behavior through a linear model. The finite element solver for the calculation of the deformations due to pressure and thermal loads (described in Chapter 6) can handle assemblies by considering the parts as "welded" together in the region of contact. Considering the results illustrated in the previous section, the idea of assuming the valve plate and the end case as "welded" together appears reasonable and it plays in favor of a linear approximation. The critical aspect is to figure out how to cancel the big deflection of the valve plate but still capturing the deflection of the end case.

One approach that may be followed to achieve that result is to change the mechanical properties of the bronze coating to steel, maintaining instead the original thermal conductivity; in this way when the thermal deflection of the assembly is calculated, the valve plate just "follows" the thermal deflection of the end case, replicating the

pattern observed through the contact analysis. The same setting is acceptable also in the case of the calculation of the pressure deformation. Table 6.1 summarizes the material properties used in the model.

Material	E [GPa]	ν [ ]	λ W/mK	α μm/mK
Steel	207	0.29	43	13
Cast iron	157	0.26	55	10
Bronze*	207	0.29	115	13
Brass	110	0.31	84	18

Table 6.1
Mechanical and thermodynamic properties of the materials defined in the model. *The properties of bronze were changed to maximize the fidelity of the linear model.

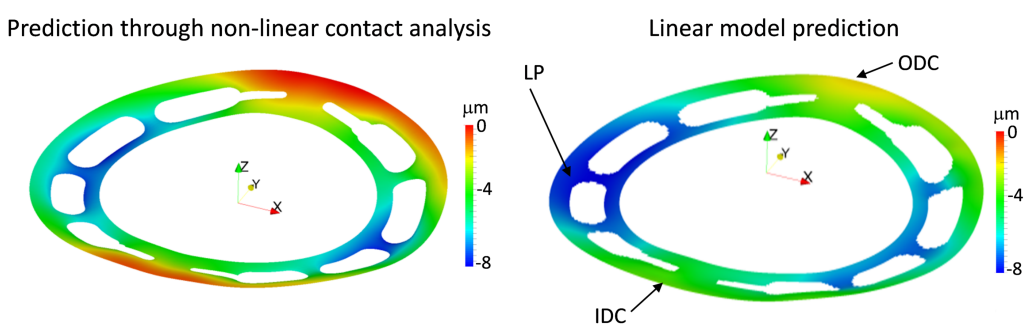

Fig. 6.11. Valve plate surface deformation, comparison between linear model and non-linear solid contact analysis for $\Delta p = 200$ bar.

Figure 6.11 shows a comparison between the predicted surface of the valve plate (considering pressure and temperature deformations) in the case of non-linear contact analysis and simplified linear approach, for a differential pressure of 200 bar. The linear model predicts a deformation that is in good correlation with the non-linear contact analysis, but some differences are visible: on the low pressure side (indicated

with LP in figure) the linear model overestimates the deformation of 3-4 microns; the deformation is instead underestimated at the two points corresponding to the piston at the inner and outer dead center, indicated with IDP and ODP respectively.

The approach follows to address the contact problem in this case is tailored to tackle the specific situation of the example chosen for the discussion; other design may require a different approach. In general, if the valve plate and end case assembly presents a solid contact situation where the valve plate is free to move, it is recommended to deeply investigate the actual behavior of the system with an advanced commercial solver. Then, the best setting of the linear model should be pursued in order to replicate the same pattern observed through the non-linear solid contact analysis.

7. MEASUREMENTS OF THE SURFACE TEMPERATURE OF THE VALVE PLATE DURING OPERATION

The final goal of the fluid structure interaction model developed in this work is to predict the fluid film thickness during operation, therefore the unquestionable validation of the model should go through the direct measurement of the fluid film thickness. The problem is that the fluid film is typically in the order of magnitude of a few microns on average and it can reach also sub-micron levels in limited region of the lubricating interface. Moreover, the region of the machine where the measurement has to be performed is hardly accessible and subjected to severe conditions.

Some attempts to measure the fluid film thickness between cylinder block and valve plate have been documented in literature and were described in Sec. 1.2. The approaches proposed by the previous researchers were successful, but what was actually measured was the relative position of the cylinder block with respect to the valve plate on one or more points, located typically on the outer region of the valve plate, outside the gap. In the case of Bergada et al. (2011) the three inductive sensors allowed the exact position of the cylinder block to be determined over one shaft revolution; the fluid film thickness was then derived by assuming the valve plate in its nominal position. This limit in this approach is in the inability to derive the actual film thickness because effects like elastic deformations or micro alteration of the surfaces are not included when the fluid film geometry is calculated just from the relative position of the cylinder block with respect to the valve plate.

Other approaches found in literature considered temperature as an indicator of the fluid film thickness. Olems (2000) developed a test stand where the internal temperature of the cylinder block was used to validate the prediction of the fluid film thickness in the piston/cylinder interface; later Jouini and Ivantysynova (2008)

measured the surface temperature of the valve plate and use it for the same purpose on the cylinder block / valve plate interface. The temperature of the solid parts defining a lubricating interface is certainly related to the fluid film thickness, but it is interesting to discuss their connection in detail in order to understand advantages and disadvantages.

7.1 Surface temperature measurements as indicator of fluid film thickness

The steady state temperature of the rotating kit during the operation of the machine represents an equilibrium between the heat that is generated in the lubricating interfaces and the heat that is carried off by the convective heat exchange with the surrounding hydraulic fluid. Chapter 5 illustrated how the the temperature is calculated and more precisely Eq. 5.3 shows that the heat flux coming from the cylinder block valve plate interface depends on the thermal conductivity of the oil and the temperature gradient across the film. At this point it is convenient to take a closer look to the Energy equation, Eq. 2.29. The energy equation can be integrated over the volume of the fluid film and thanks to the divergence theorem the following expression is found

$$\int_{\mathcal{S}} \left(\rho \boldsymbol{V} T - \frac{\lambda}{c_p} \boldsymbol{\nabla} T \right) \cdot \boldsymbol{n} da = \int_{\mathscr{V}} \frac{\mu}{cp} \Phi_d \tag{7.1}$$

The surface integral on the left hand side is on the external boundary of the fluid film and it contains the convective and the diffusive terms; the integral on the right hand side it the total power dissipated by viscous friction in the fluid film. The surface integral can be split into the lateral boundary of the fluid film and the two surfaces in contact with the solid parts. In the case of the convective term there is no fluid flow across the film, whereas the diffusion takes place mainly in that direction, being the temperature gradient predominant in that direction. Eq. 7.1 can be rewritten as follows

$$-\int_{\mathcal{S},\mathrm{cb}} \lambda \left(\boldsymbol{\nabla} T \right)_{\mathcal{S},\mathrm{cb}} \cdot \boldsymbol{n} - \int_{\mathcal{S},\mathrm{vp}} \lambda \left(\boldsymbol{\nabla} T \right)_{\mathcal{S},\mathrm{vp}} \cdot \boldsymbol{n} = -\int_{h} \left(\rho c_p \boldsymbol{V} T \right) \cdot \boldsymbol{n} + \int_{\mathscr{V}} \mu \Phi_d \tag{7.2}$$

According to the definition in Eq. 5.3 the quantities on the left hand side are the total heat fluxes on the cylinder block and valve plate surfaces in contact with the fluid film. From Eq. 7.2 is clear that the heat fluxes that will affect the steady state temperature of cylinder block and valve plate depend on the viscous dissipation in the fluid flow and the convective effect of the leakages. As indicated in Eq. 2.32 the energy that is converted into heat by viscous friction at any point in the fluid film depends on the dynamic viscosity and the derivative of the fluid velocity across the film; on the other hand, the convection is calculated by integrating the fluid velocity expressed by Eq. 2.35 over the boundary of the fluid film. Therefore both of these variables are ultimately and strictly related to the fluid film thickness, reason why the surface temperature is indeed a good indicator of the fluid film. Furthermore temperature is relatively cheap and easy to measure, making the measurement of several point on the surface feasible, which may lead to a reasonably good representation of the fluid film thickness. In addition this method captures effects like deformation and micro alteration of the surfaces because the temperature is directly related to the actual fluid film thickness.

Unfortunately, there are also disadvantages in the validation of the model with temperature measurements. First, and most intuitive, is the fact that the surface temperature is related to the fluid film thickness but it does not depends only upon it: the surface temperature is affected by the heat exchanged by convection between the solid parts and the oil outside the lubricating interfaces in the case, displacement chambers and ports. For example, if in a certain region of the lubricating interface the dissipation is underestimated because the fluid film is not properly predicted, the measured surface temperature could be still well matched if a further error in the convective heat exchanged will compensate for it.

Another problem occurs when the interface operates at very low fluid film thickness and the condition of full film lubrication is not fully satisfied. In this case the calculation of the heat dissipated will be incorrect if the viscous dissipation function is used, moreover when high pressure spikes occur the prediction of the viscosity is

also likely to be incorrect. As a consequence, the surface temperature may not be a good indicator to validate the model if the lubricating interface is known to work in the limit of mixed friction regime.

However, since the developed model is able to predict the working temperature of cylinder block and valve plate during operation and considering that the surface temperature measurement is in the end supported by a good number of advantages, this method has been chosen to validate the model prediction.

7.2 Description of the test stand and measurement procedure

Thanks to a research project with an industry sponsor a 130 cc/rev unit of commercial production was donated to carry out a comparison with the model predictions with measurements. The industry sponsor equipped the valve plate on that unit with 22 K-type thermocouples, as represented in Fig. 7.1 and 7.2.

Two series of 10 thermocopules (equally spaced in circumferential direction) were placed at two radial positions close to the inner and outer region of the sealing land. As represented in Fig. 7.2 the end case was minimally modified with respect to the original design: a circumferential grove was machined on the top part of the end case (not visible in the picture) to fit the thermocouples attached to the bottom of the valve plate and an additional hole was added to allow the thermocouples cables to have a way out of the machine. To prevent any pollution of the oil the thermocouple wires were not glued, but held with aluminum clamps; epoxy glue was used only to seal the external part of the hole on the end case. Two additional thermocouples were placed in the housing: the first thermocouple was located half a way through the thickness of the housing ad used to monitor the temperature of the metal; the second thermocouple was run all the way through the housing wall and it could probe the temperature of the oil around the cylinder block during operation.

The unit was mounted on a test stand designed to take steady state measurements. The test stand is represented in Fig. 7.3. The pump equipped with the thermocouples

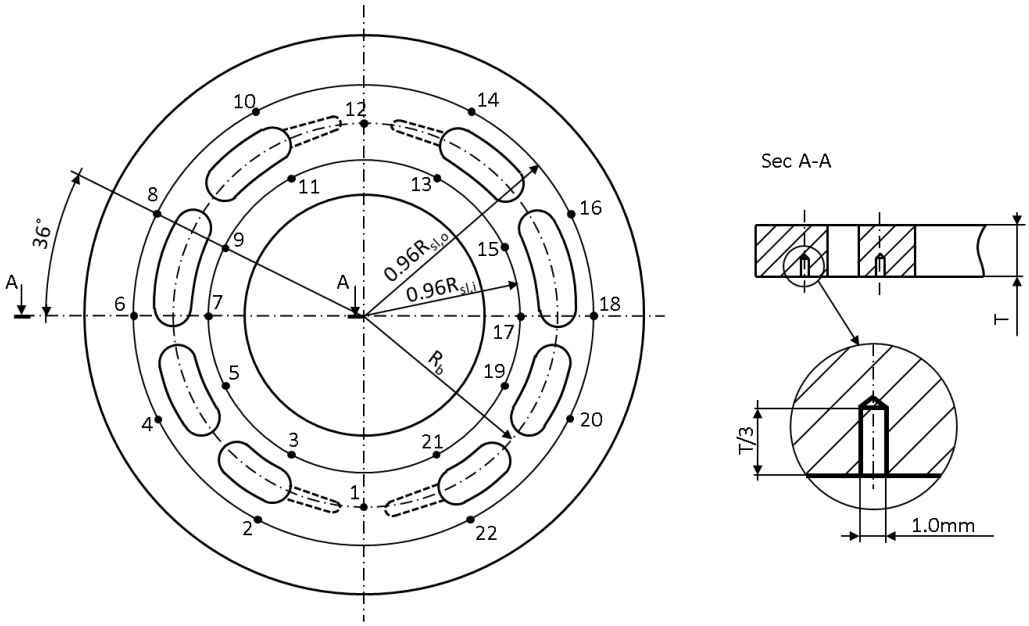

Fig. 7.1. Position of the thermocouples on the valve plate mounted on the 130cc unit used for the measurements (view from the bottom of the valve plate).

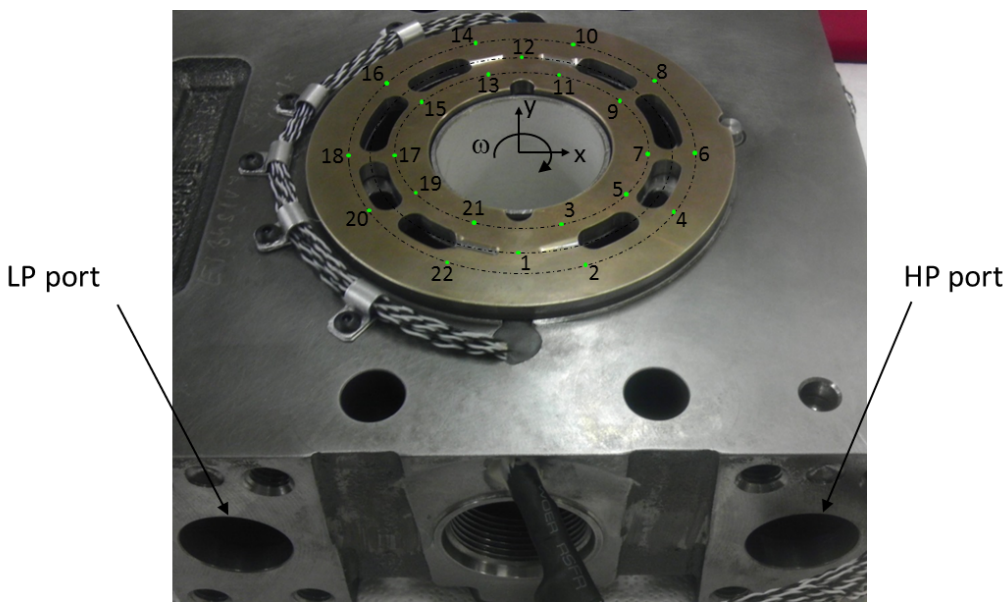

Fig. 7.2. Picture of the valve plate and case that were used for the measurements. The position of the thermocuples is also indicated.

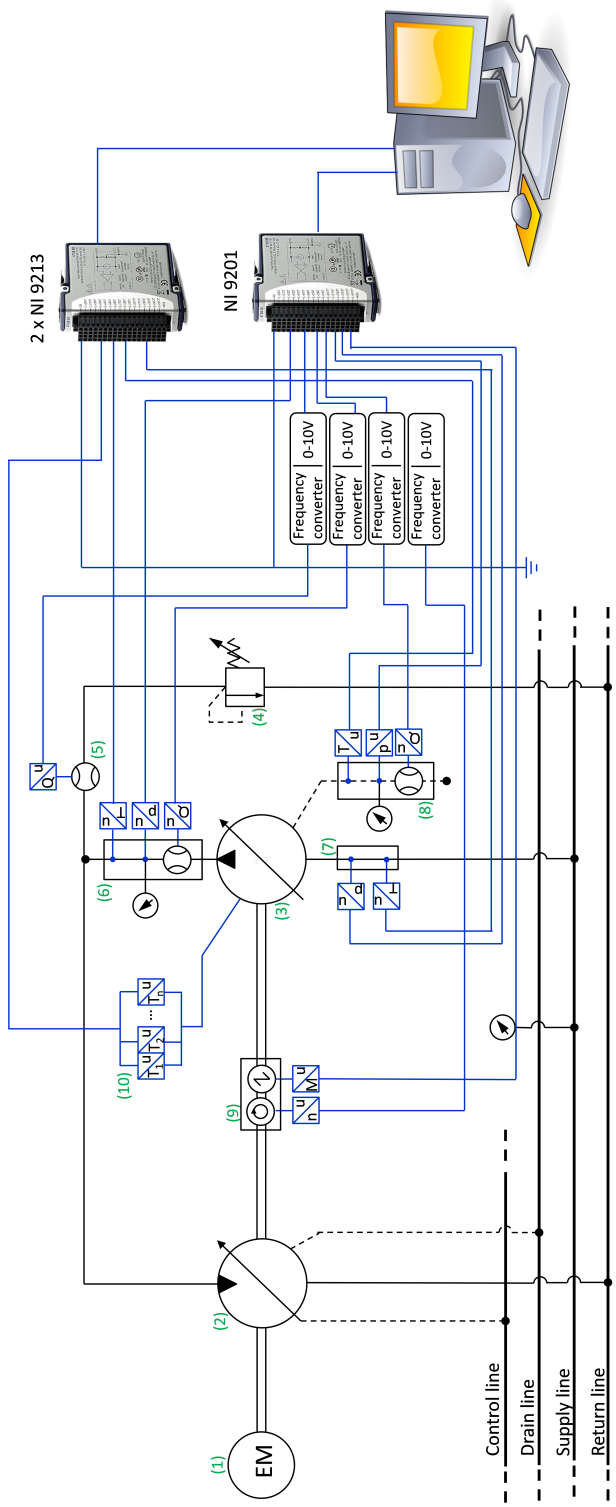

Fig. 7.3. Schematic of the test stand developed to take steady state temperature measurements on a 130cc axial piston unit.

is labeled with (3). Considering a maximum differential pressure of 400 bar during the measurements the maximum theoretical torque that the electric drive (1) would have to provide is the following:

$$M_{\mathrm{em},th} = \frac{V_{i,(4)}\Delta p}{2\pi} = \frac{130\mathrm{cc/rev}\,400\mathrm{bar}}{20\pi} \approx 830\mathrm{Nm} \tag{7.3}$$

That value was way beyond the torque limitation of the available electric drive and for this reason a second hydraulic unit of 100 cc/rev size (2) was added to the system. The second unit works as a load and allows the power absorbed by the main unit to ricirculate back on the shaft; in this way the electric drive has just to provide the torque deriving from the difference in displacement plus the torque loss:

$$M_{\mathrm{em},th} = \frac{\omega\Delta p}{2\pi}\left(V_{i,(3)} - V_{i,(2)}\right) + M_{l,2} \tag{7.4}$$

The relief valve (4) was set to the desired pressure and the displacement of unit (2) was controlled in order to have as less flow as possible through the valve. The displacement of the main unit was maintained fixed through threaded rods that held the adjustment system of the swash plate at the proper angle. Since no control pressure was needed on the main unit, the charge pump was removed.

Pressure and temperature were monitored at the inlet, outlet and case port of the main unit through the blocks (7),(6) and (8) respectively. The temperature at the inlet port of the main unit was controlled to be within $52 \pm 1°$C; the hydraulic fluid in the system was an ISO 32 viscosity grade, which means that the inlet viscosity was held at 20 cSt (see Appendix B); the inlet pressure was also controlled to 25 ± 1 bar. Moreover, for each operating condition in terms of speed, displacement and differential pressure, any measurements was taken only when steady state conditions were reached; this means that the outlet and case temperature have not being changing for at least 10 minutes before the data acquisition. This condition is very important to ensure because the predictions of the simulation model are based on the assumption of steady state conditions and thermal equilibrium. Outlet and case flows of the main unit were also measured, through the flow meters in blocks (6) and (8) respectively; in addition

input torque and angular speed at the pump's shaft was monitored through the torque meter (9).

Table 7.1 summarizes the specification of all the components in Fig 7.3. The signals from the sensors were recorded through two types of input modules from National Instruments. The NI 9211 was used for the signals of the pressure transducers and the flow meters, in this case properly programmed frequency converters were used to convert the signal into a 0-10V signal. Two NI 9213 input modules were instead used for all the thermocouples signals. The data was acquired through a compact DAQ from National instrument, NI cDAQ-9178.

The measurements results for a number of selected operating conditions are discussed in the next chapter and compared with the prediction of the fluid structure interaction and thermal model.

ID	Sensor	Specification
(1)	Elective drive	Max power: 225 kW, Max torque 615 Nm @ 3500 rpm
(2)	Hydraulic motor	Displacement 100 cc/rev, Flow at rated speed 330 l/min, Max torque @ max displacement 668 Nm
(3)	Main unit	Displacement 130 cc/rev, Flow at rated speed 416 l/min, Max torque @ max displacement 931 Nm
(4)	Pressure relief valve	max flow 350 l/min
(5)	Flow meter	1 to 250 l/min range , error ± 3% of measured value
(6)	Block containing pressure transducer, thermocouple and flow meter	Flow meter: 3.5-525 l/m range, error ± 3% of measured value; Thermocouple: K-type, error grater than 2.2° or 0.75% of measured value; Pressure transducer: 0-600 bar range, error ± 0.15% of measured value
(7)	Block containing pressure transducer and thermocouple	Thermocouple: K-type, error grater than 2.2° or 0.75% of measured value; Pressure transducer: 0-100 bar range, error ± 0.15% of measured value
(8)	Block containing pressure transducer, thermocouple and flow meter	Flow meter: 0-18 l/m range, error ± 3% of measured value; Thermocouple: K-type, error grater than 2.2° or 0.75% of measured value; Pressure transducer: 0-25 bar range, error ± 0.15% of measured value
(9)	Torque meter	0-1000 Nm range, error ± 0.2% of full scale
(10)	Set of 22 thermocouples in the valve plate plus two additional thermocouples in the housing	K-type, error grater than 2.2° or 0.75% of measured value

Table 7.1
Summary and specification of all the components in Fig. 7.3.

8. SIMULATION MODEL PREDICTIONS AND COMPARISON WITH MEASUREMENTS

In this chapter the measured valve plate surface is compared with the prediction of the model for a number of operating conditions. In the context of the validation, the simulation results relative to one selected operating condition are discussed in detail in terms of predicted fluid film thickness, pressure fields, elastic deformation of the solid parts and power losses. A further simulation study on a second unit is also proposed, in order to show the applicability of the model to a variety of different design of commercial production.

8.1 Comparison between model prediction and measurements

In this section the predicted valve plate temperature is compared with the measurements discussed in Chapter 7. All the simulation studies were carried out at partial displacement, $\beta = 50\%$, two speeds of 2000 and 2800 rpm and three differential pressures of $\Delta p = 50$, 200 and 400 bar. Figures from 8.1 to 8.12 illustrate the comparison between the measured and the predicted temperature field at the 22 points were the thermocouples were located in the valve plate. In the same figures, on the bottom, two cross sections in the $x-z$ and $y-z$ planes show the fluid film and the solid parts warped with the combination of pressure and thermal deformations in the fluid film thickness direction, with a scale of 1000:1. The average and maximum percentage errors between measured and simulated temperatures are listed for all the simulated operating conditions in Tables 8.1 and 8.2.

For almost all the operating conditions the average percentage error was below 5%, which confirms the ability of the model to predict the trend of the temperature field in the valve plate as the operating conditions changes. Also the two-dimensional

	$n = 2000$ rpm $\Delta p = 50$ bar $\beta = 50\%$	$n = 2000$ rpm $\Delta p = 200$ bar $\beta = 50\%$	$n = 2000$ rpm $\Delta p = 400$ bar $\beta = 50\%$
Avg. Err.	4.2	4.2	6.3
Max. Err.	13.6	15.0	20.32

Table 8.1
Average and maximum percentage error between measured and predicted temperature as function of operating pressure at 2000 rpm. The maximum and average error were calculated for the 21 working thermocouples in the valve plate.

	$n = 2800$ rpm $\Delta p = 50$ bar $\beta = 50\%$	$n = 2800$ rpm $\Delta p = 200$ bar $\beta = 50\%$	$n = 2800$ rpm $\Delta p = 400$ bar $\beta = 50\%$
Avg. Err.	4.3	4.6	4.9
Max. Err.	8.5	12.6	11.2

Table 8.2
Average and maximum percentage error between measured and predicted temperature as function of operating pressure at 2800 rpm. The maximum and average error were calculated for the 21 working thermocouples in the valve plate.

character of the temperature field in the valve plate is reasonably well match, even though there are points were the percentage error reached values above 15%. The simulation model confirmed that for those operating conditions a stable film of lubricant was present between cylinder block and valve plate. In some small regions though, the fluid film thickness reached values close to the combined surface roughness of the two surfaces, indicating conditions at the limit of mixed lubrication.

It interesting to notice that the model captures pretty much all the different types of variations of the temperature field with speed and operating pressure exhibited by the measurements:

- At low pressure the temperature field looks quite symmetric with respect to the vertical centerline (y-axis) and the outer region of the sealing land appears to be at higher temperature than the inner region.
- The highest temperatures were observed at the top and at the bottom of the sealing land, slightly decentered on the high pressure side
- At higher differential pressure, i.e. $\Delta p > 200$ bar the high pressure region becomes warmer than the low pressure side and furthermore the difference between inner and outer areas of the sealing land vanishes.
- the maximum temperature on the valve plate surface does not change as the pressure increases.

The observed behaviour is fully explained thanks to the results of the simulation model. The predicted fluid film was more or less axisymmetric at low pressure operation; since the circumferential velocity increases as the radial position increases, for the same fluid film thickness the viscous dissipation was higher at the outer region of the sealing land and lower at the inner region, leading to the observed temperature difference. As the working pressure increases the elastic deformation of the solid parts generates a thicker gap on the high pressure side of the interface. The combination of a thicker gap and higher pressure drastically rises the leakages; in this condition the effect of the associated viscous dissipation in radial direction becomes as important as the circumferential component associated with the rotation of the cylinder block. It is remarkable how the model can also capture the difference in temperature of almost 25° between inner and outer regions of the sealing land, which are explained by the convex deflection of the cylinder block due to the thermal loads. Further details in this regard are discussed in the next section, where a selected operating condition will be thoroughly analyzed.

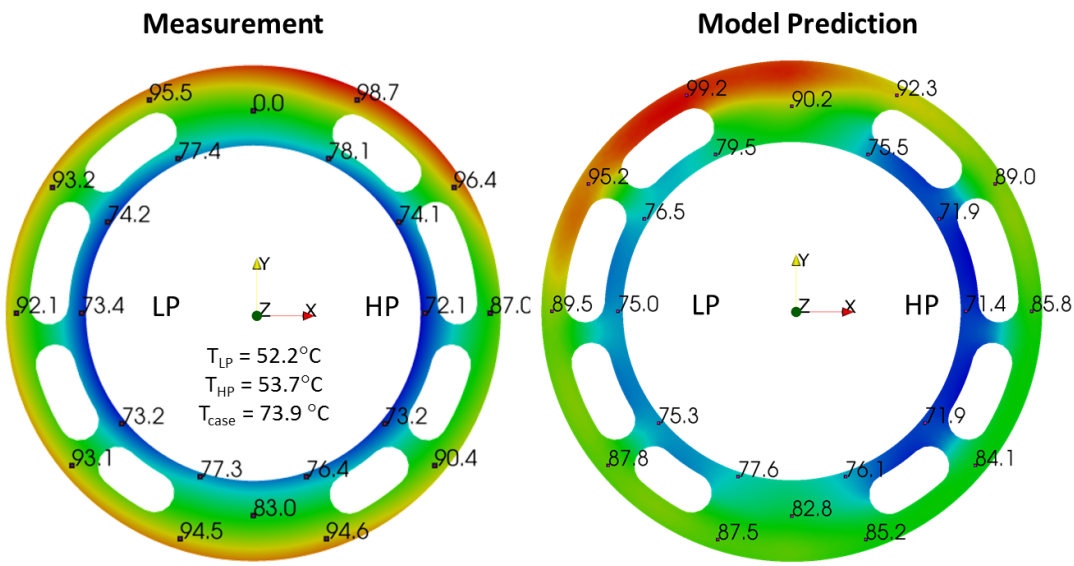

Fig. 8.1. Comparison between measured and predicted surface temperature measurement of the valve plate @ 2000 rpm, 50 bar and 50% displacement.

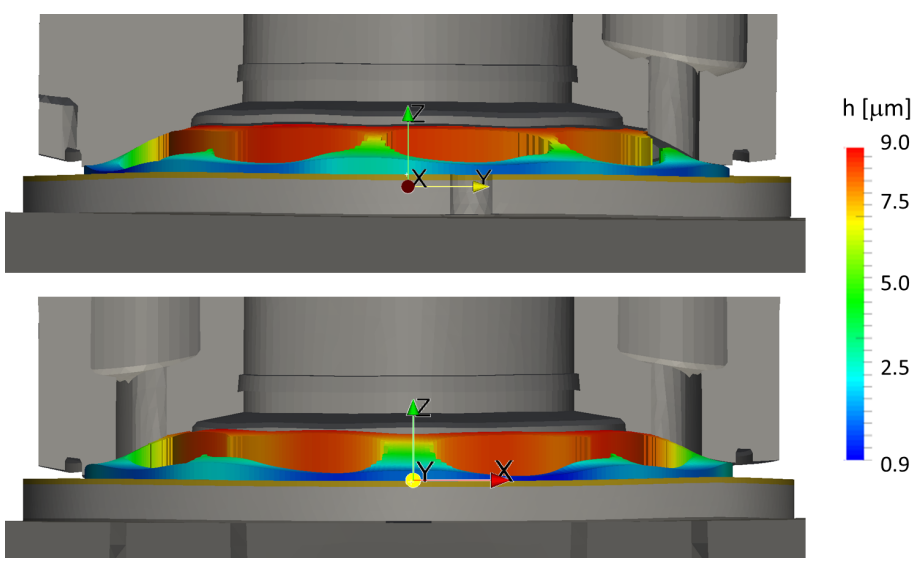

Fig. 8.2. Cross sections in the $y - z$ and $x - z$ plane, illustrating the predicted fluid film thickness between cylinder block and valve plate, @ 2000 rpm, 50 bar and 50%. The solid parts were warped with the elastic deformations due to pressure and temperature (the scaling factor is 1000:1 in z direction).

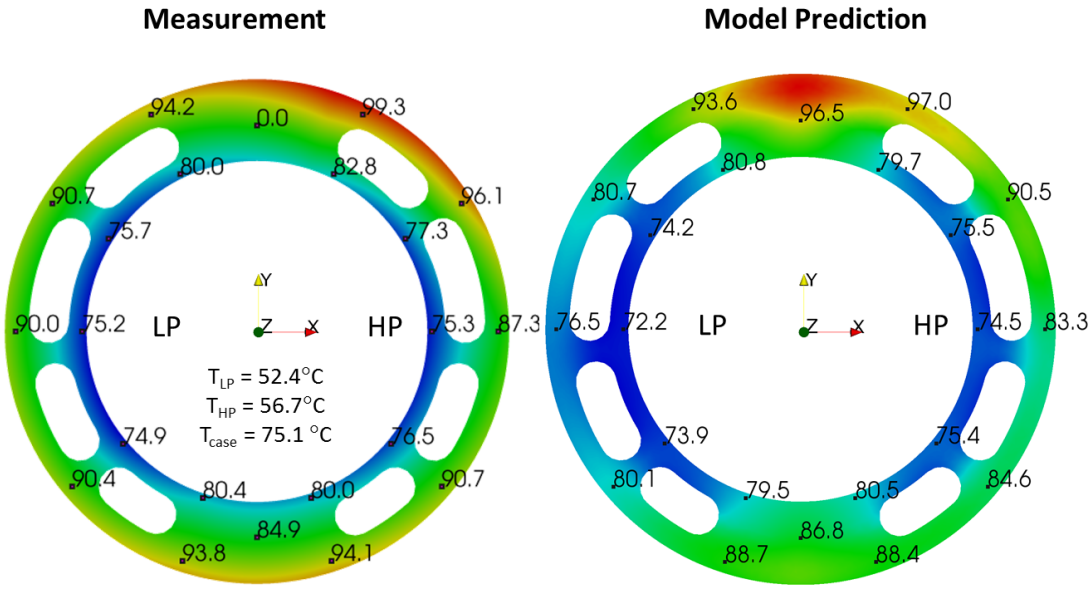

Fig. 8.3. Comparison between measured and predicted surface temperature measurement of the valve plate @ 2000 rpm, 200 bar and 50% displacement.

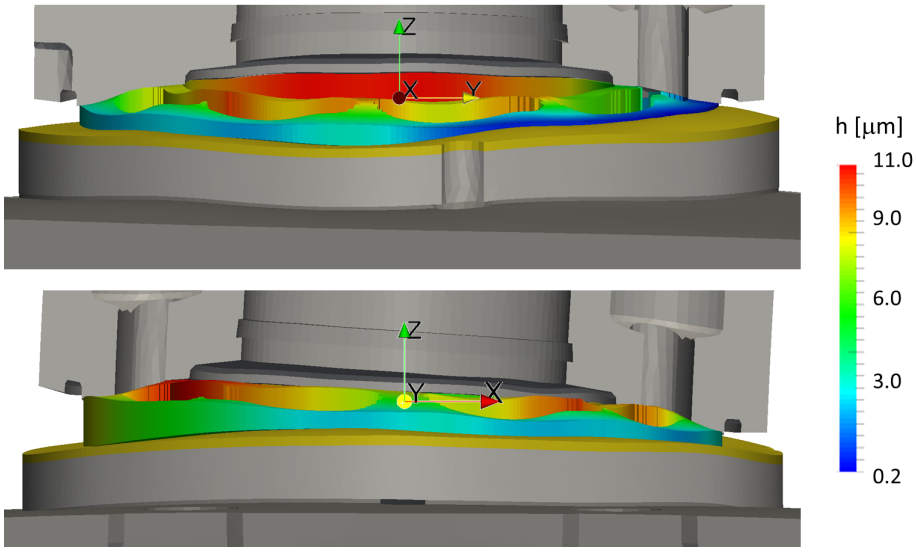

Fig. 8.4. Cross sections in the $y - z$ and $x - z$ plane, illustrating the predicted fluid film thickness between cylinder block and valve plate, @ 2000 rpm, 200 bar and 50%. The solid parts were warped with the elastic deformations due to pressure and temperature (the scaling factor is 1000:1 in z direction).

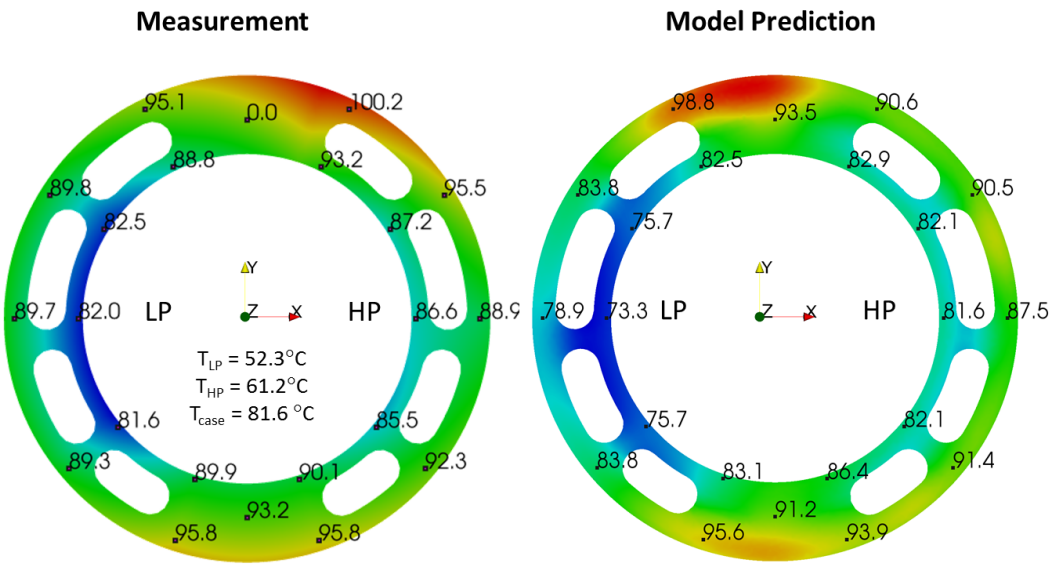

Fig. 8.5. Comparison between measured and predicted surface temperature measurement of the valve plate @ 2000 rpm, 400 bar and 50% displacement.

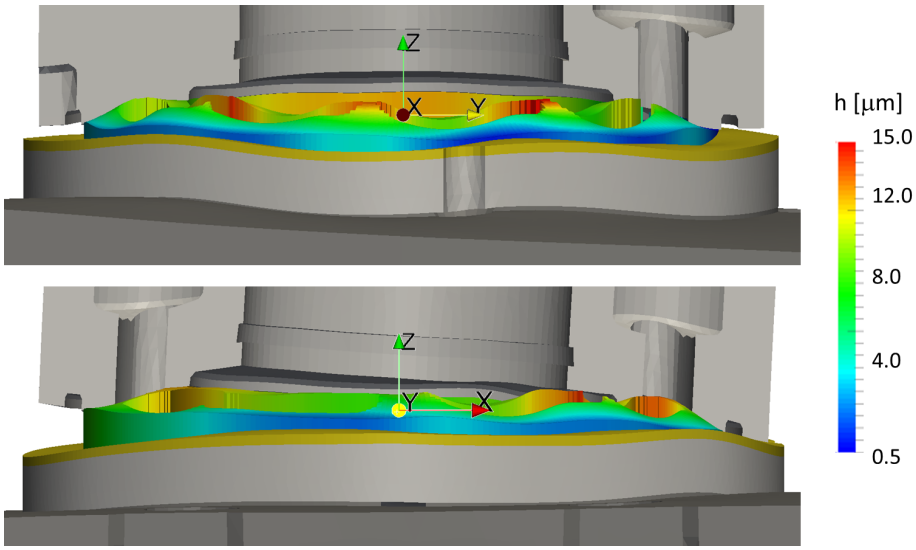

Fig. 8.6. Cross sections in the $y - z$ and $x - z$ plane, illustrating the predicted fluid film thickness between cylinder block and valve plate, @ 2000 rpm, 400 bar and 50%. The solid parts were warped with the elastic deformations due to pressure and temperature (the scaling factor is 1000:1 in z direction).

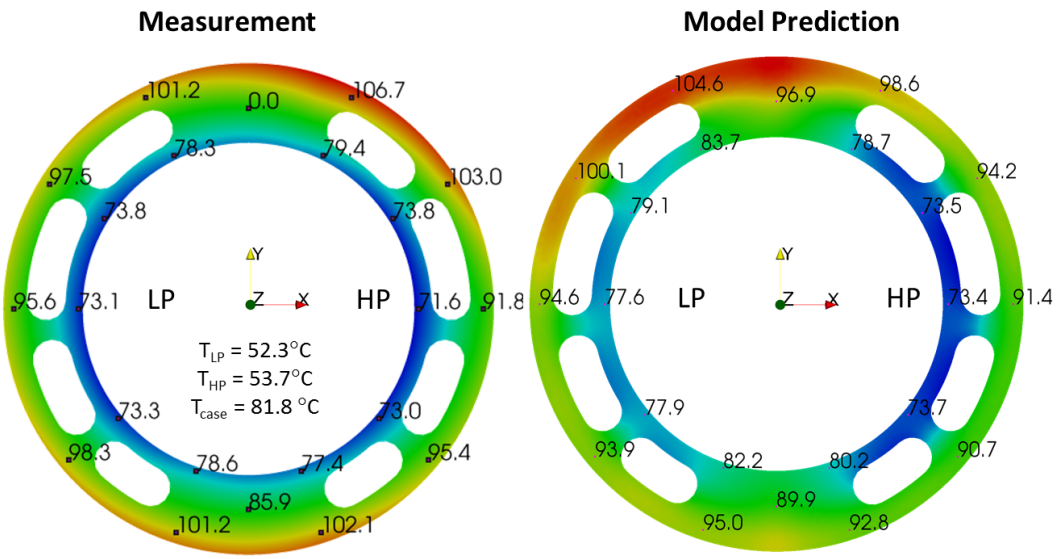

Fig. 8.7. Comparison between measured and predicted surface temperature measurement of the valve plate @ 2800 rpm, 50 bar and 50% displacement.

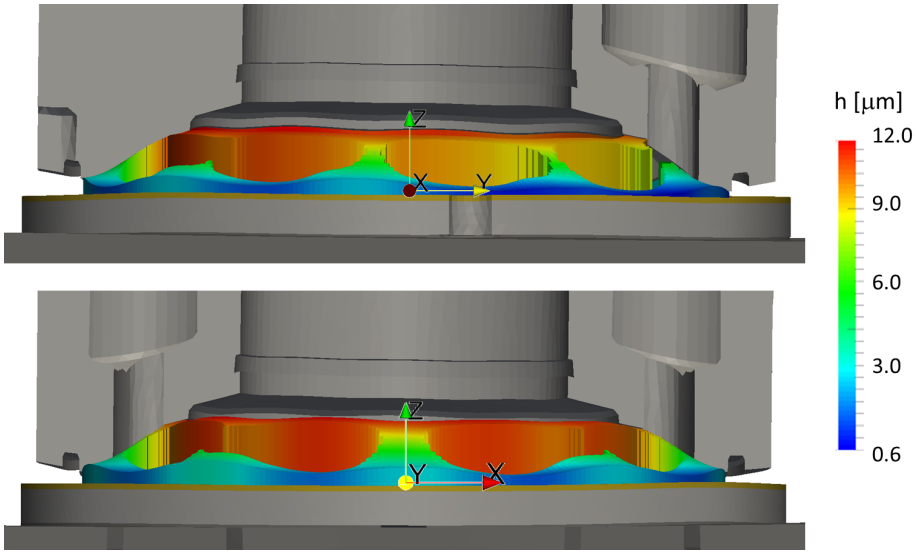

Fig. 8.8. Cross sections in the $y - z$ and $x - z$ plane, illustrating the predicted fluid film thickness between cylinder block and valve plate, @ 2800 rpm, 50 bar and 50%. The solid parts were warped with the elastic deformations due to pressure and temperature (the scaling factor is 1000:1 in z direction).

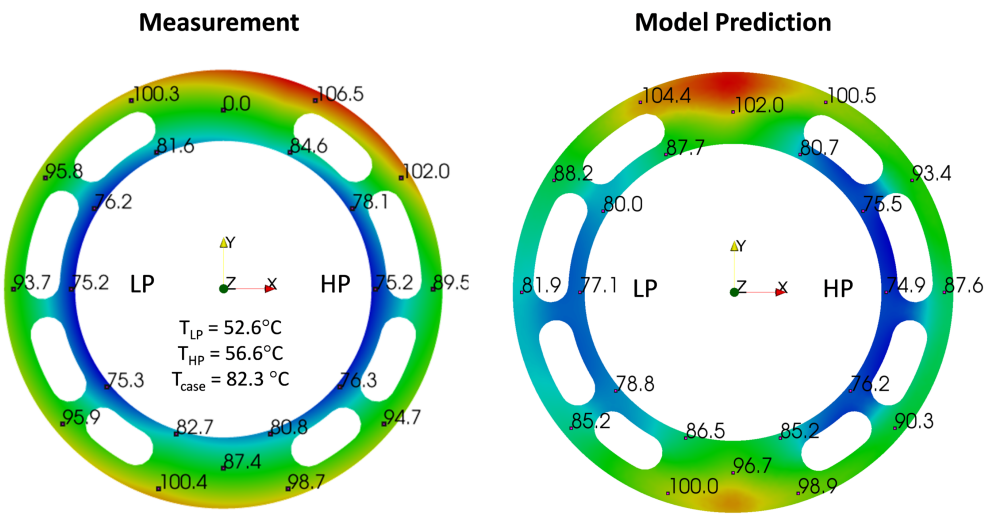

Fig. 8.9. Comparison between measured and predicted surface temperature measurement of the valve plate @ 2800 rpm, 200 bar and 50% displacement.

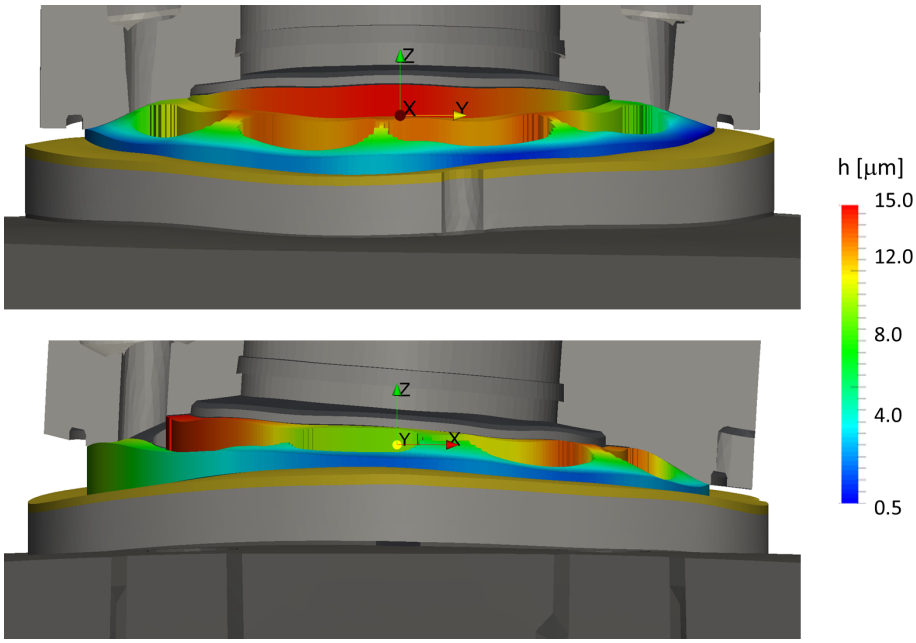

Fig. 8.10. Cross sections in the $y - z$ and $x - z$ plane, illustrating the predicted fluid film thickness between cylinder block and valve plate, @ 2800 rpm, 200 bar and 50%. The solid parts were warped with the elastic deformations due to pressure and temperature (the scaling factor is 1000:1 in z direction).

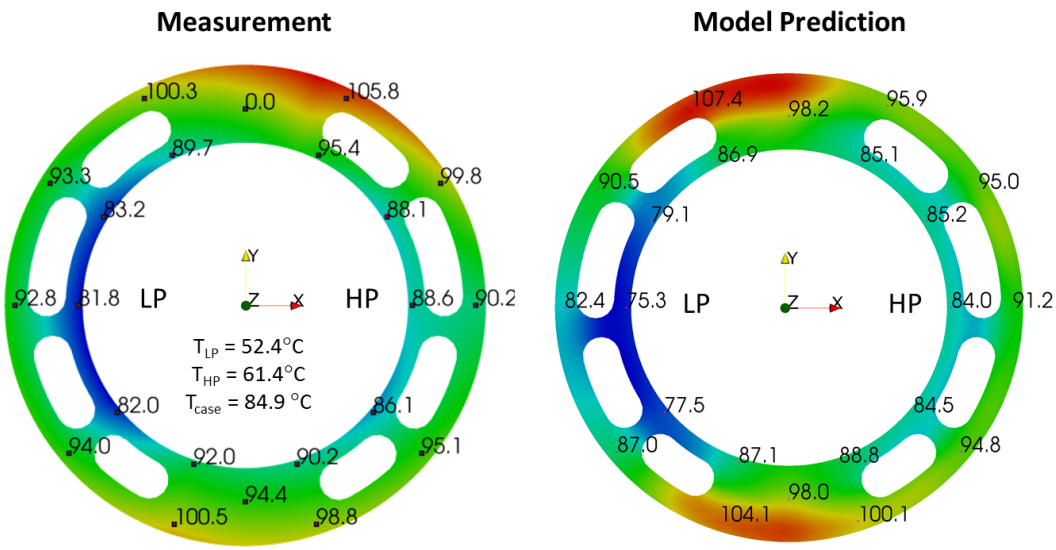

Fig. 8.11. Comparison between measured and predicted surface temperature measurement of the valve plate @ 2800 rpm, 400 bar and 50% displacement.

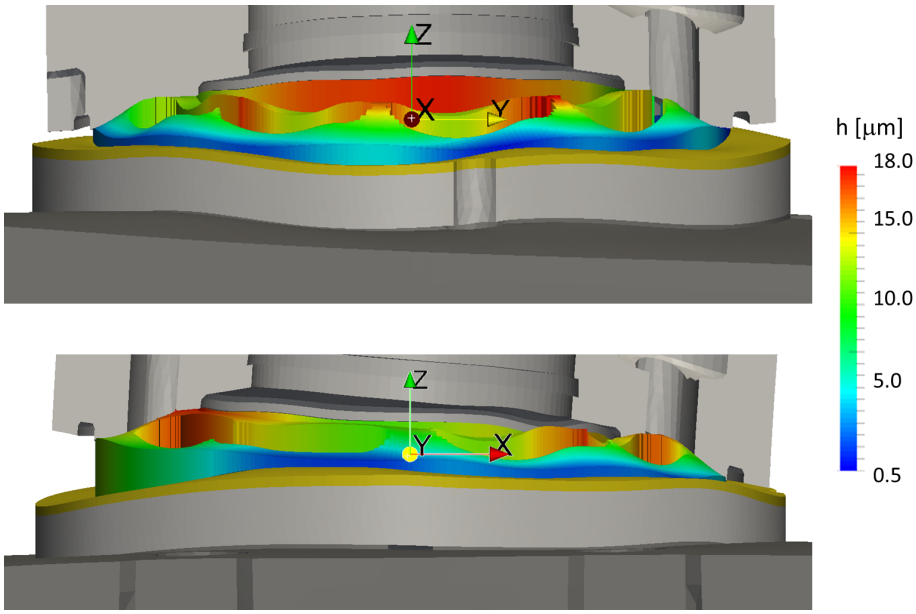

Fig. 8.12. Cross sections in the $y-z$ and $x-z$ plane, illustrating the predicted fluid film thickness between cylinder block and valve plate, @ 2800 rpm, 400 bar and 50%. The solid parts were warped with the elastic deformations due to pressure and temperature (the scaling factor is 1000:1 in z direction).

8.2 Simulation results for a selected operating condition

In this section the results of the developed fluid structure interaction and thermal model described in the previous section are discussed in detail for a selected operating condition, corresponding to a speed of 2000 rpm a differential pressure of 400 bar and 50% displacement angle. Figure 8.13 shows the total axial force F_{Bz} and the two moments M_{Bx} and M_{By} on the cylinder block resulting from the external loads condition and from the pressure field in the fluid film, when only the hydrostatic component is considered. As expected, the external loads on the cylinder block are

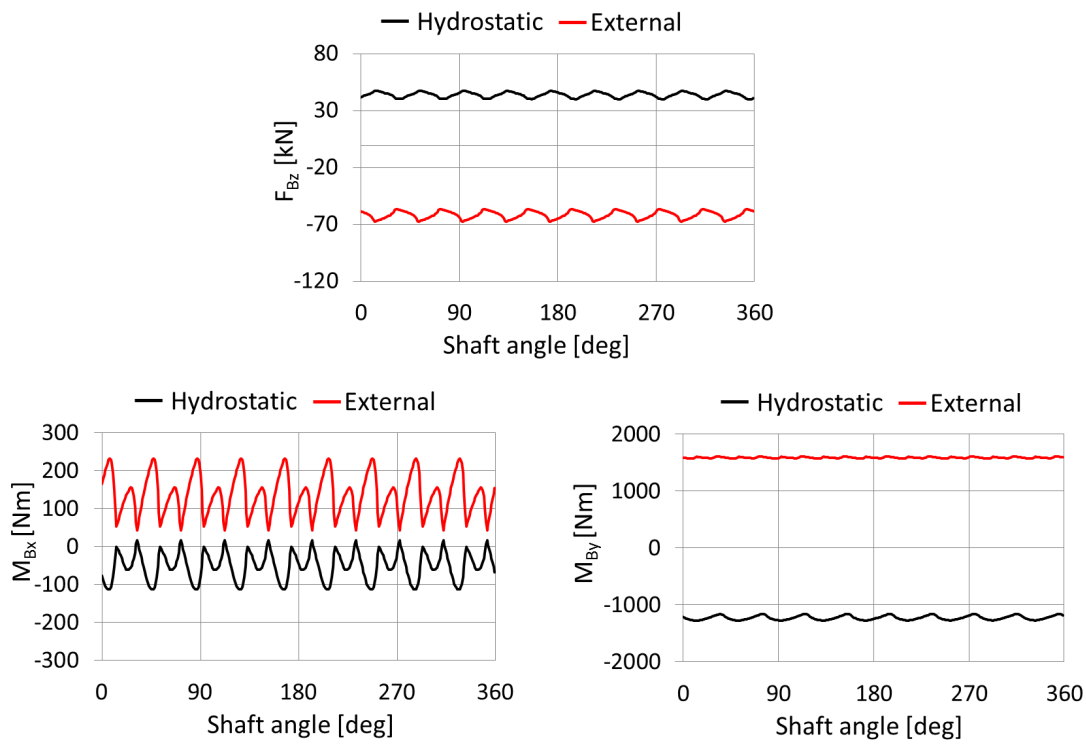

Fig. 8.13. External loads on the cylinder block over one shaft revolution @ $n = 2000$rpm, $\Delta p = 200$ bar and $\beta = 50\%$.

greater than the opposite loads determined by the hydrostatic pressure field in the fluid film: hydrodynamic components are thus necessary to achieve the equilibrium during operation. Looking just at the moments imbalance, it is reasonable to assume that the cylinder block is likely to tilt with positive rotations around the y and x axis.

The assumption is confirmed by looking at Fig. 8.14, which illustrates the predicted position of the cylinder block at the three reference points P_1, P_2 and P_3 (indicated in Fig. 2.15) with respect to the plane $z = 0$ of Fig. 2.16. The point P_2, where

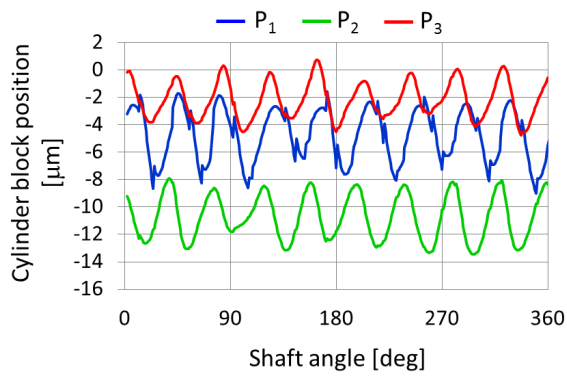

Fig. 8.14. Cylinder block position and film thickness over one shaft revolution @ $n = 2000$rpm, $\Delta p = 200$ bar and $\beta = 50\%$.

the cylinder block is mainly inclined, is located at positive x and negative y. This position is indeed the result of a combination of positive rotations around the y and x axis. The cylinder block position does not provide any information about the fluid film thickness though, because when deformations are present the fluid film thickness is not defined just by the relative position of the solid parts.

A three-dimensional representation of the fluid film may help to better understand the actual geometry of the fluid film and the operation of the lubricating interface. Fig. 8.14 illustrates the fluid film geometry scaled 1000 times in the fluid film thickness direction and the pressure field for six different angular positions, starting from $\varphi = 0$ and moving up to $\varphi = 360°$ with steps of 60°. Looking at Fig. 8.15 it is clear that low fluid film thickness conditions are limited to the peripheral region of the sealing land; the lowest fluid film is observed at the outermost region of the sealing land, along the y axis. The figure also shows that an important hydrodynamic component is present in the pressure field at all the angles. The hydrodynamic field is not just determined by the cylinder block micro-motion or inclination with respect to the valve plate: the

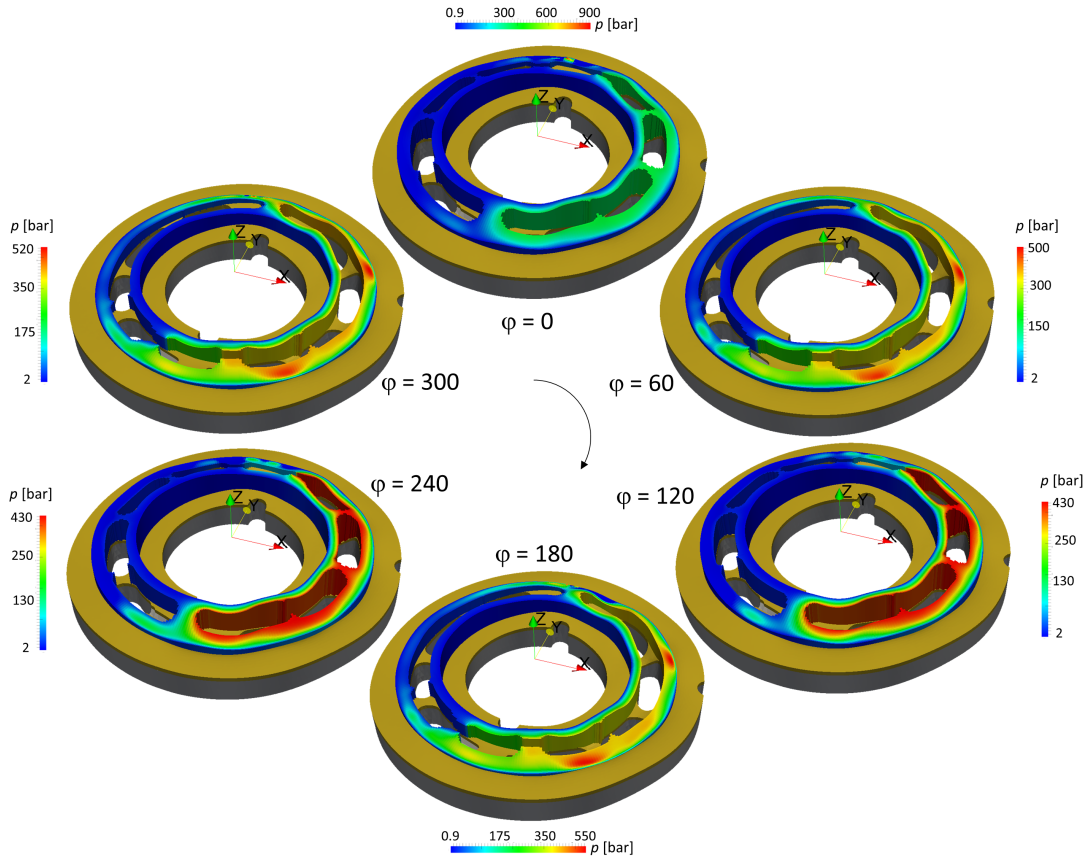

Fig. 8.15. Predicted fluid film thickness (scaled 1000:1 in z direction) and pressure field for six angular positions @ 2000 rpm, $\Delta p = 400$ bar and 50% displacement. The valve plate body is also represented and warped with scale 1000:1 in z direction with the combination of pressure and thermal loads.

elastic deformation of the parts, combined with the rotating motion of the cylinder block contributes to an additional transnational squeeze effect. It is interesting to analyze the overall deformation into the two separate contributions of pressure and thermal effect. The cylinder block surface deforms under pressure in a wave-like shape on the high pressure side, due to the pressurized fluid in the displacement chambers. The thermal deflection has instead an axisymmetric convex shape that is explained by the combination of viscous dissipation and cooling effects of the fluid in the displacement chambers, as illustrated in Fig. 8.17. The valve plate surface

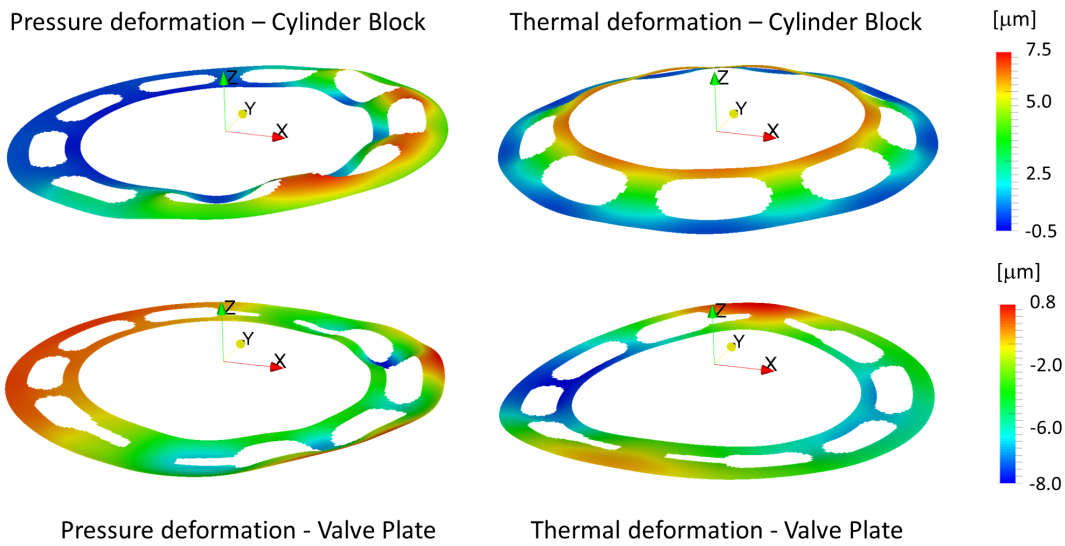

Fig. 8.16. Elastic deformations of cylinder block and valve plate surface warped with scale 1000:1 in z direction.

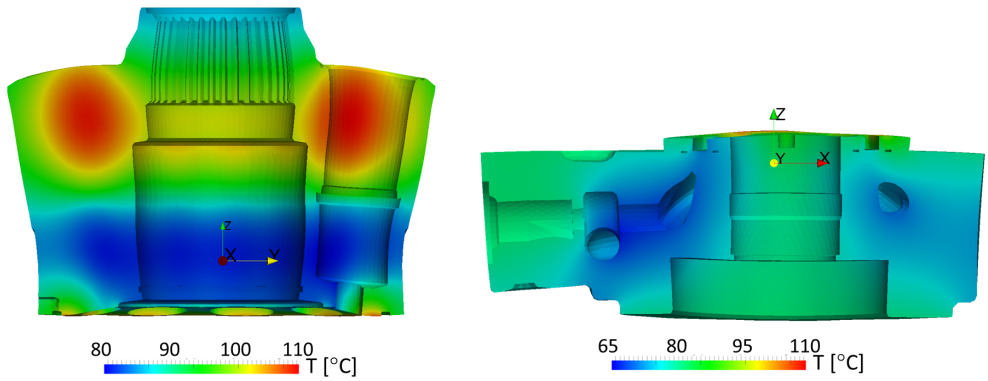

Fig. 8.17. Predicted temperature field in the cylinder block and valve plate. The two bodies were warped with the associated thermal deflection in all the directions with a scale of 1000:1.

deforms globally downward due to the pressure field in the fluid film, but the Poisson effect associated with the pressurized fluid in the high pressure port determines two upward deflections located approximately at 40° and 160° in clockwise direction from the y axis. This behavior was also observed in a more prominent way when the deformation of the valve plate and end case assembly was studied considering the

contact analysis with a commercial finite elements software: when contact and relative motion between valve plate and end case were considered the valve plate slightly detached from the end case in the two points were also the linear FEM analysis predicted maximum deformation; however, the linear analysis underestimated this effect since the two bodies were assumed as welded together.

The thermal deflection of the valve plate surface is characterized by a convex shape which develops along the x axis; the deformation is non symmetric with respect to the y axis, being the low pressure side more deformed downward. This effect is simply explained by the non-symmetric geometry of the end case, which extends more on the low pressure side in order to fit the adjustment system of the swash plate (seeFig. 8.17). The contact analysis has shown that the the valve plate remains slightly detached from the end case on the low pressure side and it does not deform of the same amount. As already pointed out in the previous section, the linear analysis overestimates the deflection of the low pressure side due to the thermal load, see Fig. 6.11

Figure 8.18 depicts the calculated power loss taking place in the cylinder block / valve plate interface over one shaft revolution. The total power loss was calculated through the viscous dissipation, Eq. 2.34 and it has an average value of about 1.7 kW. The combination of a thick fluid film on the high pressure side, visible from Fig. 8.15 ant the high differential pressure lead to a leakage of nearly 0.9 l/min. The leakage is dissipated into heat and contributes to 0.5 kW of power loss; the remaining 1.2 kW are dissipated with the viscous friction associated with Couette component of the velocity, determined by the rotation of the cylinder block.

8.3 A study of the impact of micro surface shaping on the performance of the cylinder block / valve plate interface

One of the goals of this work was to develop a model able of accounting for micro-modification of the surfaces of cylinder block and valve plate which could be

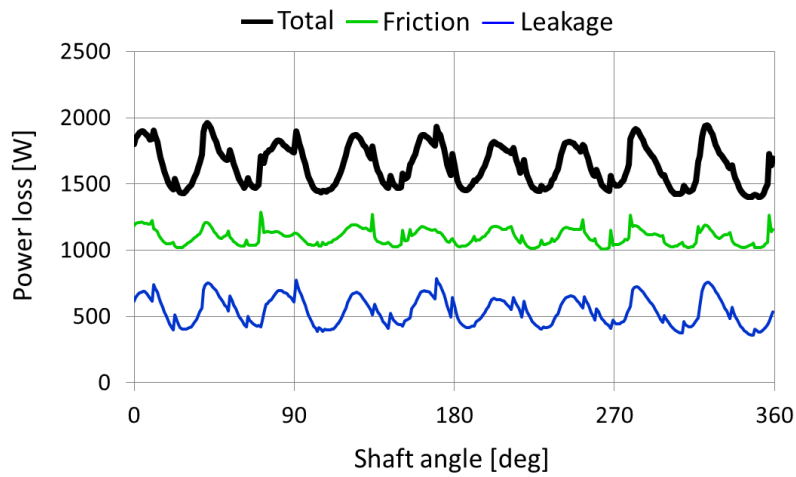

Fig. 8.18. Predicted power loss over one shaft revolution.

introduced by design or created by wear during operation. This section illustrates a simulation study on a unit where a circumferential wave pattern of a few microns amplitude is applied to the valve plate surface. The design of the cylinder block valve plate interface of the study presented in this section is different from the design of the unit analyzed in the previous section. Therefore, the results of this work not only demonstrate that the model can predict the effect of micro-modification of the surfaces on the formation of the fluid film between cylinder block and valve plate, but also show that the present model can be used to study different designs of cylinder block / valve plate interface. Actually, the proposed model was successfully applied to several different designs and the two examples described in this thesis represent just a few of the number of studies that have been accomplished.

The modification to the valve plate surface is expressed by two parameters: the amplitude A and the frequency f of the wave. The expression of the fluid film thickness, Eq. 2.25 is modified as indicated below.

$$\begin{aligned} h(r,\vartheta) =& \frac{1}{\sqrt{3}R_B} r \sin\vartheta (h_{P_2} + h_{P_2}) + \frac{1}{3R_B} r \cos\vartheta (2h_{P_1} - h_{P_2} - h_{P_3}) + \\ &+ \frac{1}{3}(h_{P_1} + h_{P_2} + h_{P_3}) + (\delta h_{CB}(r,\vartheta) - \delta h_{VP}(r,\vartheta) + A\sin(f\vartheta)) \end{aligned} \tag{8.1}$$

The idea of a micro circumferential wave pattern on the valve plate surface was introduced by Baker and Ivantysynova (2009). The two authors studied the impact of this surface's modification through the simulation model developed by Wieczorek and Ivantysynova (2002) and further improved by Huang and Ivantysynova (2003) to include the elastic deformation of the cylinder block due to pressure loads. Figure 8.19 shows the cylinder block and the valve plate of the unit selected by Baker and Ivantysynova (2009) for their study. Baker and Ivantysynova (2009) found that for

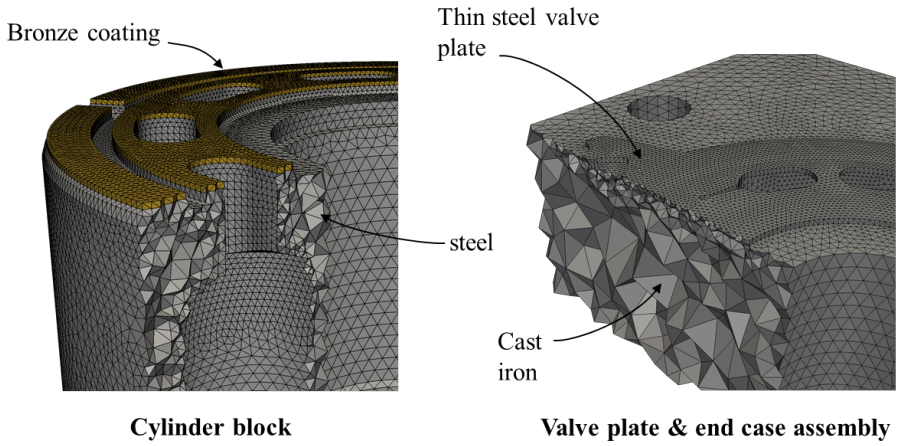

Fig. 8.19. Predicted power loss over one shaft revolution.

that design, a wave of 1μm amplitude and 15 peaks would drastically reduce the energy dissipated in the cylinder block valve plate interface over a wide range of operating conditions. The more significant reductions were found to be at low operating pressure and low displacement angle: at $\Delta p = 100$ bar, 1000 rpm and $\beta = 17\%$ a 57% reduction in power losses in the cylinder block / valve plate interface was predicted.

The aim of the study presented in this section is to investigate the impact of the additional physical phenomena introduced in this work on the effectiveness of the micro-surface pattern introduced by Baker and Ivantysynova (2009) on the same axial piston unit. In addition, before undertaking any investigation of the micro-surface pattern, the present model was further validated through surface temperature measurements on the standard design of cylinder block and valve plate design illustrated

in Fig. 8.19, published by (Jouini and Ivantysynova, 2008). The results of the validation, published in Zecchi and Ivantysynova (2012), further confirmed the accuracy of the model and suggested that the prediction of the impact of the micro-surface pattern with the present model are likely to be reliable.

The same operating conditions investigated by Baker and Ivantysynova (2009) were analyzed with the present model and the results, in terms of total power losses in the cylinder block / valve plate interface, are represented in Fig. 8.20. For a better

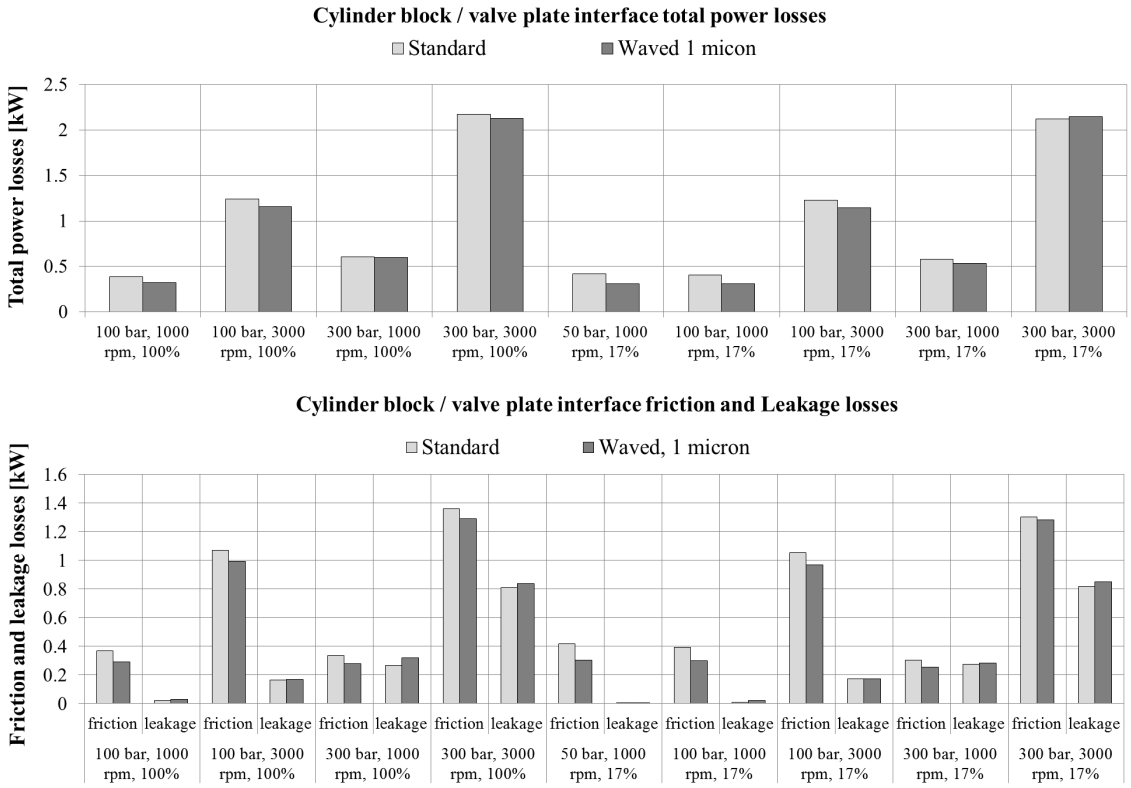

Fig. 8.20. Friction, leakage and total power losses in the cylinder block / valve plate interface for standard and waved valve plate surface predicted by the present simulation model. Standard valve plate design and micro wave pattern with 15 peaks and 1μm amplitude are represented.

understanding, the friction and leakage contribution to the total power loss are also shown. The results confirm that the waved valve plate design decreases the losses in the cylinder block / valve plate interface especially at low operating pressure, at both

full and low displacement. However, the predicted improvements are systematically lower than the previous: in the study by Baker and Ivantysynova (2008) the highest percentage difference in losses from the waved to the standard design was 57% at 100 bar, 1000 rpm and 17% displacement, while the present model predicted just a 23% improvement at the same conditions.

The lower effectiveness of the waved valve plate predicted by the present model is explained by the modifications of the film thickness determined by elasto-hydrodynamic and thermal effects. In the previous simulation study by Baker and Ivantysynova (2009), the wave pattern on the valve plate surface was responsible of a major change in the lubricating film shape, mainly at low pressure. In this condition, the limited pressure loads are associated with just a slight deformation of the cylinder block and valve plate and in addition, the deformation of the valve plate was totally neglected. Furthermore, since the model did not account for any thermal deformation of the cylinder block and valve plate, the only thermal effect was a change in viscosity and therefore the film shape was mainly affected by the wave pattern.

The situation is much different with the present model, because in this case the modification to the fluid film shape determined by the waved valve plate is just of secondary importance. Figure 8.21 and 8.22 illustrate this concept. As expected, at

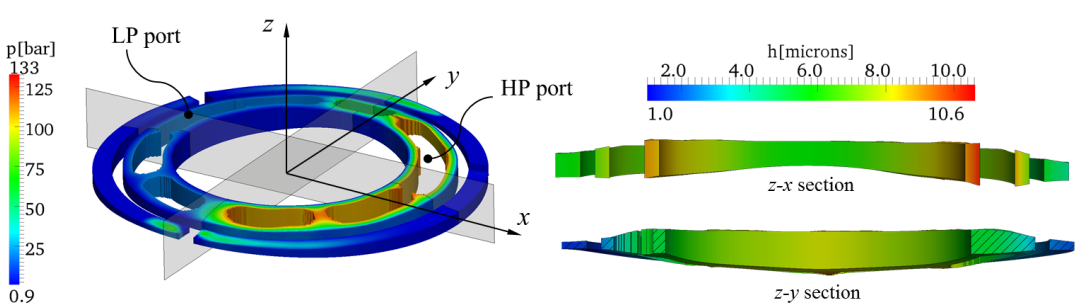

Fig. 8.21. Pressure field and film thickness for the standard design @ 1000 rpm, 100 bar and 100% displacement. (The lubricating film is magnified 1000 times in z direction

low pressure the elastic deformation is nearly negligible (the $z - x$ section does not

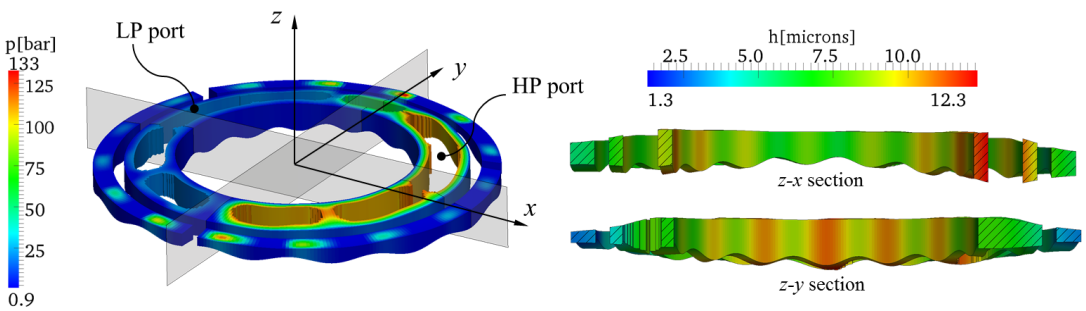

Fig. 8.22. Pressure field and film thickness for the 1μ amplitude waved valve plate @ 1000 rpm, 100 bar and 100% displacement. (The lubricating film is magnified 1000 times in z direction)

show a particular difference in film thickness between high and low pressure sides). At this operating condition the main phenomenon affecting the film shape is the thermal deformation of the solids parts: the cylinder block is responsible of the convex outline on the top side, while the valve plate / end case assembly further reduces the thickness on the peripheral along the y axis ($z - y$ section) and, at the same time, increases it along the x axis ($z - x$ section). The thermal deformation of the body is therefore what leads the performance of the interface at this condition. Certainly, for the same average film thickness the wave pattern increases the load carrying ability and in fact in Fig. 8.22 the gap is slightly thicker than in Fig. 8.21. This difference does not affect sensibly the leakage, but limits the viscous dissipation, explaining the 16% improvement of Fig. 8.20; same considerations are valid at low displacement angle, where a 23% was predicted. At higher pressure, besides the thermal effects, also the pressure deformation plays a role because it contributes to increase the average film thickness and further limits the effectiveness of the waved valve plate. At high speed and high pressure the waved surface has nearly no impact on the performance of the cylinder block / valve plate interface.

9. CONCLUSIONS AND OUTLOOK

The generation and stability pf the fluid film between cylinder block and valve plate of axial piston machines has been studied theoretically and experimentally in this work. A novel multi-physics simulation model for the prediction of the cylinder block / valve plate interface performance has been formulated and proposed to predict the steady state performance of the interface through the precise determination of the fluid film thickness as a function of the machine's operating conditions such as differential pressure, speed, displacement angle and working temperature. The film thickness is calculated over one shaft revolution on the principle of force balance, by determining the configuration of the fluid film able of meeting the external load condition of the cylinder block at every instant of time.

The major contribution of this work was in the extension of the physical phenomena included in the analysis of the interface: for the first time, the solution of the non isothermal fluid flow has been coupled with the thermal and elstic deformation analysis of the surrounding solid parts. The loads due to the pressure in the fluid film, displacement chambers, suction and discharge ports in the cylinder block and valve plate are used to calculate their resulting elastic deformations, allowing the film thickness to be estimated accounting for elasto-hydrodynamic phenomena. Furthermore, the energy dissipated in the fluid flow by viscous friction is applied as a boundary condition to solve for the steady state temperature of the solid parts, including the convective heat exchange with the oil in the case and the ambient. The temperatures of the solid bodies are used to calculate their associated thermal deflections, allowing a further correction of the film thickness prediction to be operated. Moreover, the surface temperatures of the parts are applied to improve the solution of the non isothermal fluid flow.

Such analysis is performed by coupling different numerical domains in one single numerical model. This allows the exchange of information between the different physical domains to be very flexible and effective. Several numerical techniques were formulated and coupled together in the model, to face each physical problem in the most efficient way. The non isothermal fluid flow was solved through the finite volume method and the preconditioned biconjugate gradient stabilized solver was introduced to maximize the solution speed and accuracy. Significant attention was given to the fluid-structure interaction coupling between sliding solid parts and fluid film. A fixed point iteration scheme with dynamic relaxation was developed to consider the non-linear elasto-hydrodynamic problem between the solution of the Reynolds equation and the pressure surface elastic deformation. Efficient interpolation schemes on the variables exchanged by fluid and structure were also implemented. The transient squeeze effect deriving from the rate of change of the elasto-hydrodynamic deformation was also included in the model, finding that such effect has primary importance in the prediction of the load carrying ability. A finite element thermoelastic solver was introduced to couple in a unique environment the heat transfer and the elastic deformation analysis of the solid parts. The solver takes as input the heat fluxes deriving from the viscous dissipation in the fluid flow and calculates the temperature field in the solid parts and their associated thermal deflections.

A 130 cc unit of commercial production was equipped with a number of thermocouples to measure the surface temperature of the valve plate during the machine operation. Measurements were taken under steady state condition for a wide range of operating conditions. The unit was thoroughly analyzed with the developed model and the comparison between the model prediction and the measurements confirmed the ability to predict the fluid film thickness under very different working conditions. The same outcome was confirmed by a further experimental/simulation study on a second unit of commercial production.

The model has also been successfully applied to investigate the effect of micro-surface shaping on the performance of the lubricating interface. A variety of differ-

ent designs of the cylinder block / valve plate interface have been studied with the proposed approach counting seven pumps and motors of commercial production for industrial, mobile and aerospace applications.

APPENDICES

A. DERIVATION OF THE SPECIFIC FOR OF THE REYNOLDS EQUATION USED IN THIS WORK

This appendix described in detail the derivation of the specific form of the Reynolds equation that has been used in the developed model. Such expression of the Reynolds equation is not very common in literature and since effort has been spent in its derivation it is worth to have it documented in this thesis.

For a Newtonian fluid, starting from the application of the conservation of momentum of a fluid particle, the differential form of the Navier Stokes equation is derived.

$$\frac{\partial \rho \boldsymbol{V}}{\partial t} + \boldsymbol{\nabla} \cdot \rho \boldsymbol{V}\boldsymbol{V} - \boldsymbol{\nabla} \cdot (\mu \boldsymbol{\nabla} \boldsymbol{V}) = -\boldsymbol{\nabla} p \tag{A.1}$$

Starting from Eq. A.1, in case of the fluid flow of the cylinder block / valve plate interface several assumptions can safely be made to greatly simply this equation:

1. Steady state is assumed, so the temporal inertia term $\frac{\partial \rho \boldsymbol{V}}{\partial t}$ is zero.
2. Inertial forces are negligible compared to the viscous ones, so the convective inertia term $\boldsymbol{\nabla} \cdot \rho \boldsymbol{V}\boldsymbol{V}$ can be neglected.
3. Pressure is uniform along the film thickness.
4. Gradients of the velocity in the direction of the film thickness are orders of magnitude bigger than the ones in the other directions.

There are indeed situations of practical interest where the convective inertia term $\boldsymbol{\nabla} \cdot \rho \boldsymbol{V}\boldsymbol{V}$ can be important even when the Reynolds number is rather small: this is the case of textured or dimpled surfaces. Surface texturing gained increasing attention in lubrication research because it can improve the performance of bearings by increasing the load carrying capacity for a given clearance, reducing friction and adding lubricant

storage capacity. Dobrica and Fillon (2009) carried out an interesting study about the validity of the Reynolds equation and inertia effects in textured sliders of infinite width. They concluded that, for a film thickness of the same magnitude of the dimple depth, the assumptions above are safe even for slightly large Reynolds numbers if the the ratio λ_d between the length and the depth of the dimple is sufficiently big; more precisely, they have demonstrated that for $\lambda_d = 64$ the inertia effects can totally be neglected for Reynolds number equal to 16. In this work the effect of dimpled surfaces on the cylinder block / valve plate interface was not investigated and even when the effect of micro-surface shaping was introduced, the geometry of the clearance was such that the parameter λ_d was certainly big enough to consider the assumptions above fully safe.

Figure A.1 depicts a lubricating gap bounded by two surfaces of arbitrary shape. The top surface is indicated with t and it is moving with a velocity $\boldsymbol{V}_t = (u_t, v_t, w_t)$; the bottom surface is indicated with b and it is also moving with a velocity $\boldsymbol{V}_b = (u_b, v_b, w_b)$. A given point P on the $x - y$ plane is represented in Fig. A.1 together with its projections along the z direction on the two boundary surfaces, being P_t the projection on the top surface and P_b the projection on the bottom surface. The distance (with sign) of P_t from the reference plane $z = 0$ is defined as h_t and analogous definition applies for h_b on the bottom side; notice that h_t can even be negative if the top surface lies underneath the reference plane and vice versa for h_b. The difference $h = h_t - h_b$ is the actual film thickness at the point P.

In this scenario

- Point 3 means that $p = p(x, y)$
- Point 4 means that $\dfrac{\partial \boldsymbol{V}}{\partial z} \gg \dfrac{\partial \boldsymbol{V}}{\partial x}$ and $\dfrac{\partial \boldsymbol{V}}{\partial z} \gg \dfrac{\partial \boldsymbol{V}}{\partial y}$, where $\boldsymbol{V} = (u, v, w)$ is the velocity of the lubricant in the clearance

and the Navier-Stokes equation A.1 reduces to

$$\boldsymbol{\nabla} p = \boldsymbol{\nabla} \cdot (\mu \boldsymbol{\nabla} \boldsymbol{V}) \tag{A.2}$$

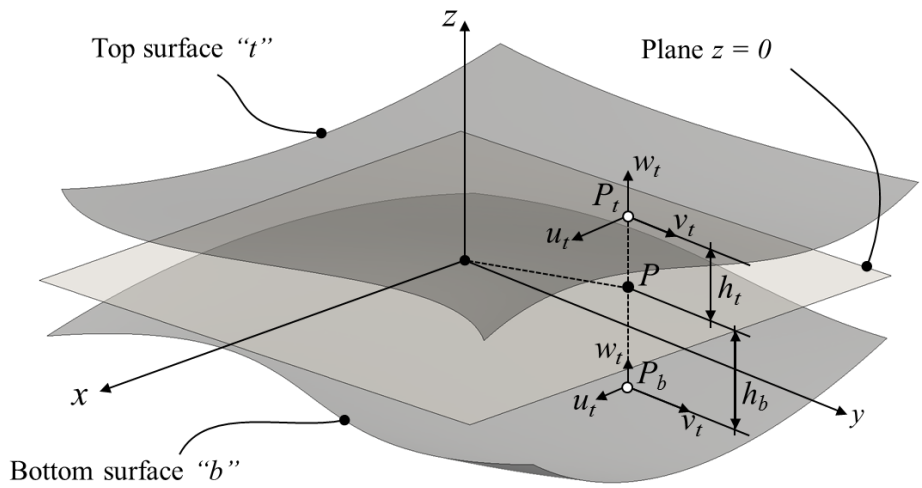

Fig. A.1. Sketch of a lubricating gap defined by two surfaces of arbitrary shape. The reference plane $z = 0$ used to derive the Reynolds equation is also represented.

In Cartesian components Eq. A.2 takes the form of Eq. A.3.

$$\begin{cases} \dfrac{\partial p}{\partial x} = \dfrac{\partial}{\partial z}\left(\mu \dfrac{\partial u}{\partial z}\right) \\ \dfrac{\partial p}{\partial y} = \dfrac{\partial}{\partial z}\left(\mu \dfrac{\partial v}{\partial z}\right) \end{cases} \tag{A.3}$$

Equations A.3 can be integrated over the z direction, obtaining

$$\begin{cases} u = \frac{z^2}{2\mu}\frac{\partial p}{\partial x} + A\frac{z}{\mu} + B \\ v = \frac{z^2}{2\mu}\frac{\partial p}{\partial y} + C\frac{z}{\mu} + D \end{cases} \tag{A.4}$$

The four integration constants can be determined imposing that

$$u = u_t \text{ and } v = v_t \quad \text{for } z = h_t$$
$$u = u_b \text{ and } v = v_b \quad \text{for } z = h_b$$

The particular solution to A.4 can be defined as follow

$$\begin{cases} u = \frac{1}{2\mu}\dfrac{\partial p}{\partial x}\left(z^2 - z(h_t + h_b) + h_t h_b\right) + z\dfrac{u_t - u_b}{h} + \dfrac{u_b h_t - u_t h_b}{h} \\ v = \frac{1}{2\mu}\dfrac{\partial p}{\partial y}\left(z^2 - z(h_t + h_b) + h_t h_b\right) + z\dfrac{v_t - v_b}{h} + \dfrac{v_b h_t - v_t h_b}{h} \end{cases} \tag{A.5}$$

Equations A.5 defines the oil velocity in the lubricating gap. It should be noticed that there are two components: one due to the pressure gradient (Poiseuille component) and one due to the dragging effect of the walls (Couette component).

Under steady state conditions, the continuity equation is expressed by Eq. A.6

$$\boldsymbol{\nabla} \cdot (\rho \boldsymbol{V}) = 0 \tag{A.6}$$

Equation A.6 is integrated over the lubricating film thickness to obtain the Reynolds equation; the problem becomes therefore the solution of the integral in Eq. A.7.

$$\int_{h_b}^{h_t} \frac{\partial (\rho u)}{\partial x} dz + \int_{h_b}^{h_t} \frac{\partial (\rho v)}{\partial y} dz + \int_{h_b}^{h_t} \frac{\partial (\rho w)}{\partial z} dz = 0 \tag{A.7}$$

The integral in Eq. A.7 can be solved by substituting the expressions in Eq. A.5 for u and v, obtaining the final result illustrated in Eq. A.8.

$$\begin{aligned} &\frac{\partial}{\partial x}\left(-\frac{\rho h^3}{12\mu}\frac{\partial p}{\partial x}\right) + \frac{\partial}{\partial y}\left(-\frac{\rho h^3}{12\mu}\frac{\partial p}{\partial y}\right) + \rho h \frac{\partial}{\partial x}\left(\frac{(u_t + u_b)}{2}\right) + \\ &+\rho h \frac{\partial}{\partial y}\left(\frac{(v_t + v_b)}{2}\right) + \frac{(u_t + u_b)}{2}\frac{\partial (\rho h)}{\partial x} + \frac{(v_t + v_b)}{2}\frac{\partial (\rho h)}{\partial y} + \\ &-\rho\left(u_t \frac{\partial h_t}{\partial x} + v_t \frac{\partial h_t}{\partial y}\right) + \rho\left(u_b \frac{\partial h_b}{\partial x} + v_b \frac{\partial h_b}{\partial y}\right) + (wt - w_b) = 0 \end{aligned} \tag{A.8}$$

Equation A.8 can be used in any geometrical configuration of the clearance, with any kind of motion of the boundary walls. Moreover, Eq. A.8 allows the viscosity to change across the film, assuming instead a uniform viscosity along the film.

The terms involving the derivative of the two surfaces velocity in Eq. A.8 are called the *stretch terms*. In this work these terms are neglected since the boundary surfaces are always characterized by a rigid motion, therefore their velocity is the same in any point and Eq. A.8 simplifies into Eq. A.9.

$$\begin{aligned} &-\frac{\partial}{\partial x}\left(\frac{\rho h^3}{12\mu}\frac{\partial p}{\partial x}\right) - \frac{\partial}{\partial y}\left(\frac{\rho h^3}{12\mu}\frac{\partial p}{\partial y}\right) + \frac{(u_t + u_b)}{2}\frac{\partial (\rho h)}{\partial x} + \frac{(v_t + v_b)}{2}\frac{\partial (\rho h)}{\partial y} + \\ &-\rho\left(u_t \frac{\partial h_t}{\partial x} + v_t \frac{\partial h_t}{\partial y}\right) + \rho\left(u_b \frac{\partial h_b}{\partial x} + v_b \frac{\partial h_b}{\partial y}\right) + \rho (w_t - w_b) = 0 \end{aligned} \tag{A.9}$$

It is convenient to express equation A.9 by means of the differential operators, in order to have a formulation independent from a specific coordinate system

$$\begin{aligned}\boldsymbol{\nabla}\cdot\left(-\frac{\rho h^3}{12\mu}\boldsymbol{\nabla}p\right)+\boldsymbol{\nabla}\cdot\left((\rho h)\,\frac{\boldsymbol{V}_t+\boldsymbol{V}_b)}{2}\right)\\ -\rho\boldsymbol{V}_t\cdot\boldsymbol{\nabla}h_t+\rho\boldsymbol{V}_b\cdot\boldsymbol{\nabla}h_b+\rho\left(w_t-w_b\right)=0\end{aligned} \tag{A.10}$$

Starting with this equation, the corresponding form for any kind of reference system can be simply derived by substituting the proper definition of the surfaces velocity and differential operators. The particular geometry of the cylinder block / valve plate interface and the motion of the cylinder block make the cylindrical coordinate system (r, ϑ, z) of Fig. 2.15 the best choice to express the Reynolds equation. In this coordinate system the differential operators are defined as in Eq. A.11.

$$\begin{aligned}\boldsymbol{\nabla}\cdot\boldsymbol{A}&=\frac{1}{r}\frac{\partial(rA_r)}{\partial r}+\frac{1}{r}\frac{\partial A_\vartheta}{\partial\vartheta}+\frac{\partial A_z}{\partial z}\\ \boldsymbol{\nabla}a&=\left(\frac{\partial a}{\partial r},\frac{1}{r}\frac{\partial a}{\partial\vartheta},\frac{\partial a}{\partial z}\right)\end{aligned} \tag{A.11}$$

In Eq. A.11, $\boldsymbol{A}$ is a generic vector and a is a generic scalar. About the velocity fields of the boundary surfaces, the valve plate is fixed while the cylinder block rotates around the z axis with an angular velocity ω, therefore they can be expressed as in Eq. A.12.

$$\begin{cases}\boldsymbol{V}_b=(0,0,0)\\ \boldsymbol{V}_t=(0,\omega r,0)\end{cases} \tag{A.12}$$

The squeeze effect in the interface is achieved by the micro-motion of the cylinder block w_t in the z direction while the valve plate is fixed and $w_b = 0$. Therefore the term $w_t - w_b$ becomes the $\partial h/\partial t$ defined by Eq. 2.26.

By substituting the definitions in Eq. A.11 and the expressions of the velocity of the two boundary surfaces of Eq. A.12, Eq. A.10 assumes its final form, expressed by Eq. A.13.

$$\frac{1}{r}\frac{\partial}{\partial r}\left(-\frac{\rho h^3}{12\mu}r\frac{\partial p}{\partial r}\right)+\frac{1}{r}\frac{\partial}{\partial\vartheta}\left(-\frac{\rho h^3}{12\mu}\frac{1}{r}\frac{\partial p}{\partial\vartheta}\right)=\omega\left(\rho\frac{\partial h_{CB}}{\partial\theta}-\frac{1}{2}\frac{\partial\left(\rho h\right)}{\partial\theta}\right)-\rho\frac{\partial h}{\partial t} \tag{A.13}$$

Equation A.13 is the Reynolds equation used in this work.

B. DETERMINATION OF THE MATHEMATICAL MODEL OF THE HYDRAULIC FLUID USED FOR THE MEASUREMENTS AND SIMULATIONS PRESENTED IN THIS THESIS

The hydraulic fluid used for the measurements described in this thesis was a mineral oil with viscosity index 32 according to the definition in the standard ISO 3448. A sample of the oil was sent to a third party laboratory where viscosity and density were measured as a function of pressure and temperature. This appendix presents the details of the development of the mathematical model used to calculate the fluid properties in simulation.

B.1 Development of the density equation

The measured variation of density as a function of pressure is illustrated in Table B.1 for three different temperatures. The variation of density is well described by the following equation

$$\begin{aligned}\rho(p,T) = \rho_0 \big[1 + c_{\rho T}(T - T_0) + c_{\rho p}(p - p_0) + c_{\rho p2}(p - p_0)^2 + \\ + c_{\rho pT}(T - T_0)(p - p_0) + c_{\rho p2T}(T - T_0)(p - p_0)^2\big]\end{aligned} \tag{B.1}$$

The reference temperature was chose to be 25°C and the reference pressure 1.03 bar, equal to the atmospheric value. The reference density is therefore $\rho_0 = 843.3$ kg/m^3. The remaining five constants are determined through best fit of the data in Table B.1. Figure B.1 shows the variation of density as a function of pressure at reference temperature, Fig. B.1-b the variation of density as a function of temperature at the reference pressure. At reference pressure, Eq. B.1 becomes

$$\rho(p_0, T) = \rho_0 \left[1 + c_{\rho T}(T - T_0)\right] \tag{B.2}$$

p[bar]	$\rho(T = 25\text{C})$ [kg/m^3]	$\rho(T = 75\text{C})$ [kg/m^3]	$\rho(T = 120\text{C})$ [kg/m^3]
1378.95	900.8	878.5	859.5
1068.69	890.1	866.9	844.4
758.42	878.8	854.0	832.8
448.16	865.8	839.0	816.0
137.90	850.7	821.2	795.2
1.03	843.3	812.0	784.3

Table B.1
Measured variation of density as a function of pressure for three different temperatures

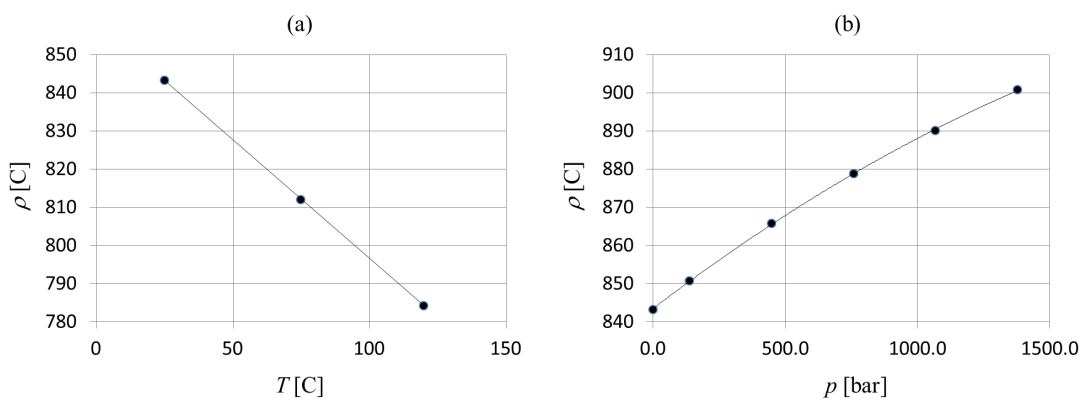

Fig. B.1. (a) variation of density as a function of temperature at the reference pressure; (b) variation of density as a function of pressure at reference temperature.

and the constant $c_{\rho T}$ was found to be $-7.365 \cdot 10^{-4}$ 1/°C. At reference temperature Eq. B.1 becomes

$$\rho(p, T_0) = \rho_0 \left[1 + c_{\rho p}(p - p_0) + c_{\rho p2}(p - p_0)^2\right] \tag{B.3}$$

The two constants were determined through a quadratic fit and are equal to $c_{\rho p} = -9.930 \cdot 10^{-9}$ 1/bar and $c_{\rho 2p} = 6.284 \cdot 10^{-5}$ 1/bar^2.

Figure B.2 show the variation of density as a function of pressure at the other two temperatures in Table B.1. At $T = \bar{T}$, Eq. B.1 becomes

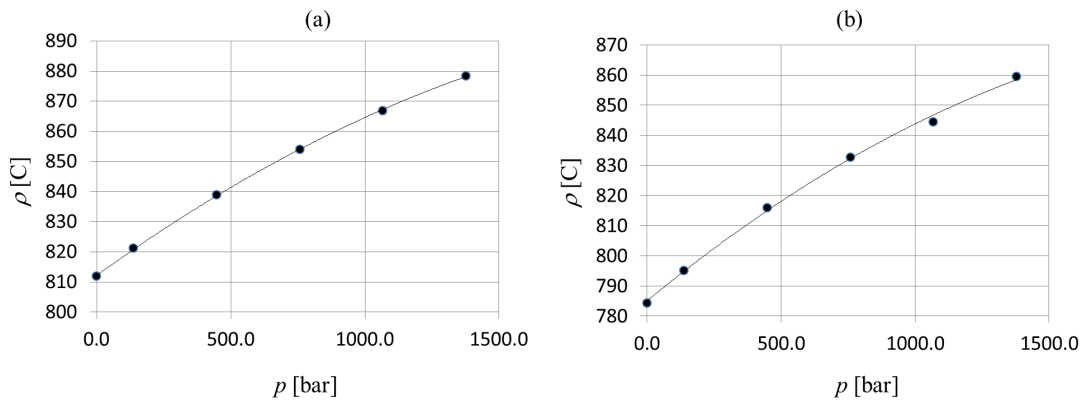

Fig. B.2. (a) variation of density as a function of pressure at $T = 75°\text{C}$; (b) variation of density as a function of pressure at $T = 120°\text{C}$.

$$\begin{aligned}\rho(p,\bar{T}) = \rho_0 \left[1 + c_{\rho T}(\bar{T} - T_0) + c_{\rho p}(p - p_0) + c_{\rho p2}(p - p_0)^2 + \right.\\ \left. + c_{\rho pT}(\bar{T} - T_0)(p - p_0) + c_{\rho p2T}(\bar{T} - T_0)(p - p_0)^2\right] = \\ = \rho_0 \left[1 + c_{\rho T}(\bar{T} - T_0)\right] + (p - p_0)\rho_0 \left[c_{\rho p} + c_{\rho pT}(\bar{T} - T_0)\right] + \\ + (p - p_0)^2 \rho_0 \left[c_{\rho p2} + c_{\rho p2T}(\bar{T} - T_0)\right]\end{aligned} \tag{B.4}$$

Equation B.4 can be written to express $\rho(p, T = 25°\text{C})$ and $\rho(p, T = 120°\text{C})$ and the two remaining constants can be calculate through the curve fittings in Fig. B.2 for $T = 75°\text{C}$ and $T = 120°\text{C}$:

- the constant $c_{\rho pT}$ was calculated as $2.637 \cdot 10^{-7}$ 1/bar°C in the case of Fig.B.2-a and $2.541 \cdot 10^{-7}$ 1/bar°C in the case of Fig.B.2-b; the average $2.589 \cdot 10^{-7}$ 1/°C was chosen.

- the constant $c_{\rho p2T}$ was calculated as $-8.125 \cdot 10^{-11}$ 1/bar^2 °C in the case of Fig.B.2-a and $-7.37 \cdot 10^{-11}$ 1/bar^2 °C in the case of Fig.B.2-b; the average $-7.748 \cdot 10^{-11}$ 1/bar^2 °C was chosen.

Table B.2 summarizes the constant that maximizes the fit of Eq. B.1 to the measured data. Equation B.1 can be rewritten by substituting the definitions of the

ρ_0 (kg/m^3)	$c_{\rho T}$ (1/°C)	$c_{\rho p}$ (1/bar)	$c_{\rho p2}$ (1/bar^2)	$c_{\rho pT}$ (1/bar°C)	$c_{\rho p2T}$ (1/bar^2 °C)
843.3	$-7.365 \cdot 10^{-4}$	$-9.930 \cdot 10^{-9}$	$6.284 \cdot 10^{-5}$	$2.589 \cdot 10^{-7}$	$-7.748 \cdot 10^{-11}$

Table B.2
Constants in the Eq. B.1 that maximize the fit with the measured data.

constants in Table B.2

$$\begin{aligned}\rho(p,T) = 843.3\,\big[1 - 7.365 \cdot 10^{-4}(T-T_0) - 9.930 \cdot 10^{-9}(p-p_0) + \\ 6.284 \cdot 10^{-5}(p-p_0)^2 + 2.589 \cdot 10^{-7}(T-T_0)(p-p_0) + \\ -7.748 \cdot 10^{-11}(T-T_0)(p-p_0)^2\big]\end{aligned} \tag{B.5}$$

The resulting density will be expressed in kg/m^3; pressure has to be entered in bar and temperature in °C. The error between the density calculated with Eq. B.1 and any measured value is always below 0.5%, confirming that the developed mathematical well replicates the observed behavior of the fluid.

B.2 Development of the isothermal bulk modulus equation

The isothermal bulk modulus is related to the density through the following equation

$$K(p,T) = \frac{\rho(p,T)}{\left(\dfrac{\partial \rho}{\partial p}\right)_T} \tag{B.6}$$

Thanks to the equation developed for the density, the bulk modulus can be derived by means of the definition in Eq. B.6 as indicated in Eq. B.7.

$$\begin{aligned}K(p,T) = \frac{1 + c_{\rho T}(T-T_0) + c_{\rho p}(p-p_0) + c_{\rho p2}(p-_0)^2}{c_{\rho p} + c_{\rho T}(T-T_0) + 2c_{\rho p2}(p-p_0) + 2c_{\rho p2T}(p-p_0)(T-T_0)} + \\ + \frac{c_{\rho pT}(T-T_0)(p-p_0) + c_{\rho p2T}(T-T_0)(p-p_0)^2}{c_{\rho p} + c_{\rho T}(T-T_0) + 2c_{\rho p2}(p-p_0) + 2c_{\rho p2T}(p-p_0)(T-T_0)}\end{aligned} \tag{B.7}$$

Figure B.5 depicts the variation of bulk modulus as a function of temperature for different constant pressures, calculated with Eq. B.7.

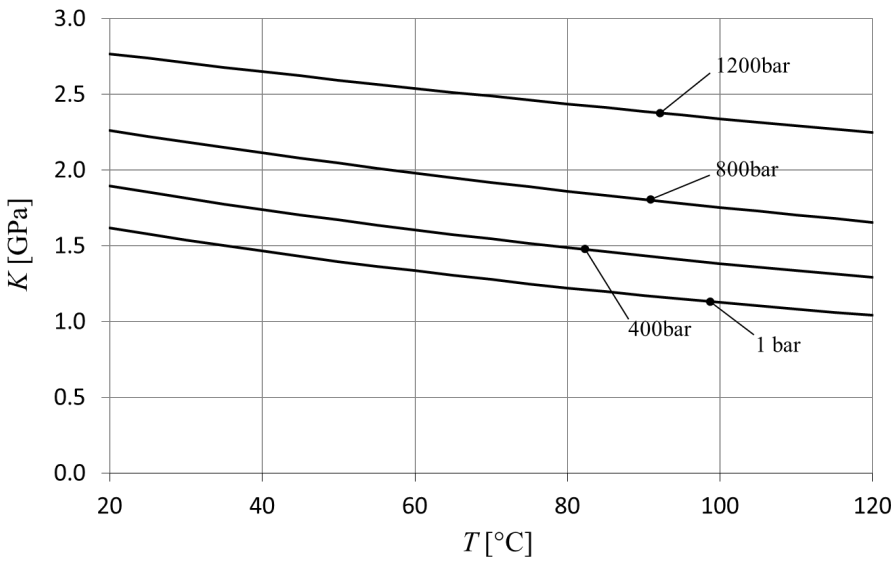

Fig. B.3. Variation of bulk modulus as a function of temperature for different constant pressures.

B.3 Development of the viscosity equation

The viscosity was measured through anelectromagnetric viscosimeter as a function of pressure is listed in Table B.3 for five different temperatures. The viscosity exhibit a quadratic variation with pressure and this variation appears to change at different temperatures, as illustrated in Fig. B.4 for $T = 25°\text{C}$ and $T = 75°\text{C}$. Therefore the equation that has to be define would look like the following.

$$\mu(p, T) = f_0(T) + f_1(T)(p - p_0) + f_2(T)(p - p_0)^2 \tag{B.8}$$

The three functions $f_0(T)$, $f_1(T)$ and $f_2(T)$ can be determined by applying the least square method to the the measured data. Figure B.9 shows the variation of $f_0(T)$, $f_1(T)$ and $f_2(T)$ with temperature. A double log scale was used because that representation make the curve fitting easier. The three functions have been defined as

p[bar]	$\mu(T = 25\text{C})$ [cP]	$\mu(T = 50\text{C})$ [cP]	$\mu(T = 75\text{C})$ [cP]	$\mu(T = 100\text{C})$ [cP]	$\mu(T = 120\text{C})$ [cP]
1377.92	528.05	162.53	61.82	28.13	17.16
1274.50	464.17	140.13	53.78	25.21	15.50
1171.07	404.94	120.22	46.91	22.55	13.96
1067.65	350.36	102.70	40.81	20.09	12.52
964.23	300.43	87.09	35.87	17.78	11.13
860.81	255.90	74.87	31.37	15.74	9.97
757.39	213.16	64.19	27.62	13.97	8.88
653.97	177.93	54.76	23.91	12.35	7.97
550.55	148.28	46.72	20.75	10.80	7.11
447.13	121.28	39.55	17.93	9.43	6.32
343.70	97.82	32.93	15.46	8.21	5.63
240.28	78.13	27.30	13.22	7.18	4.94
136.86	62.75	22.38	11.27	6.22	4.28
67.91	54.16	19.57	10.04	5.65	3.88
33.44	49.84	18.21	9.46	5.35	3.69
1.03	46.24	17.01	8.93	5.07	3.51

Table B.3
Measured variation of dynamic viscosity as a function of pressure for five different temperatures

indicated in Eq B.9.

$$
\begin{aligned}
f_0(T) &= \exp\left[-0.372 \ln T^2 + 1.314 \ln T + 3.504\right] \\
f_1(T) &= \exp\left[-1.867 \ln T^3 + 23.333 \ln T^2 - 97.48 \ln T + 132.42\right] \\
f_2(T) &= \exp\left[-0.930 \ln T^2 + 4.958 \ln T - 14.818\right]
\end{aligned}
\tag{B.9}
$$

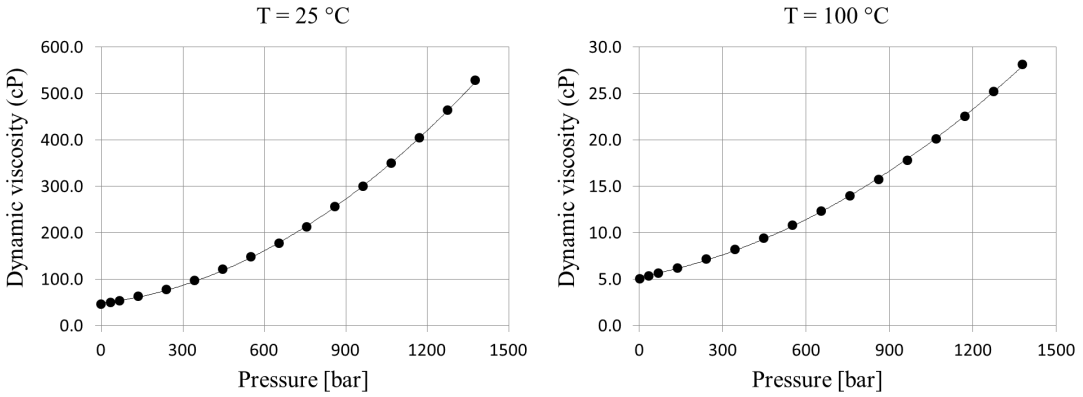

Fig. B.4. Variation of dynamic viscosity as a function of pressure at 25°C and 100°C.

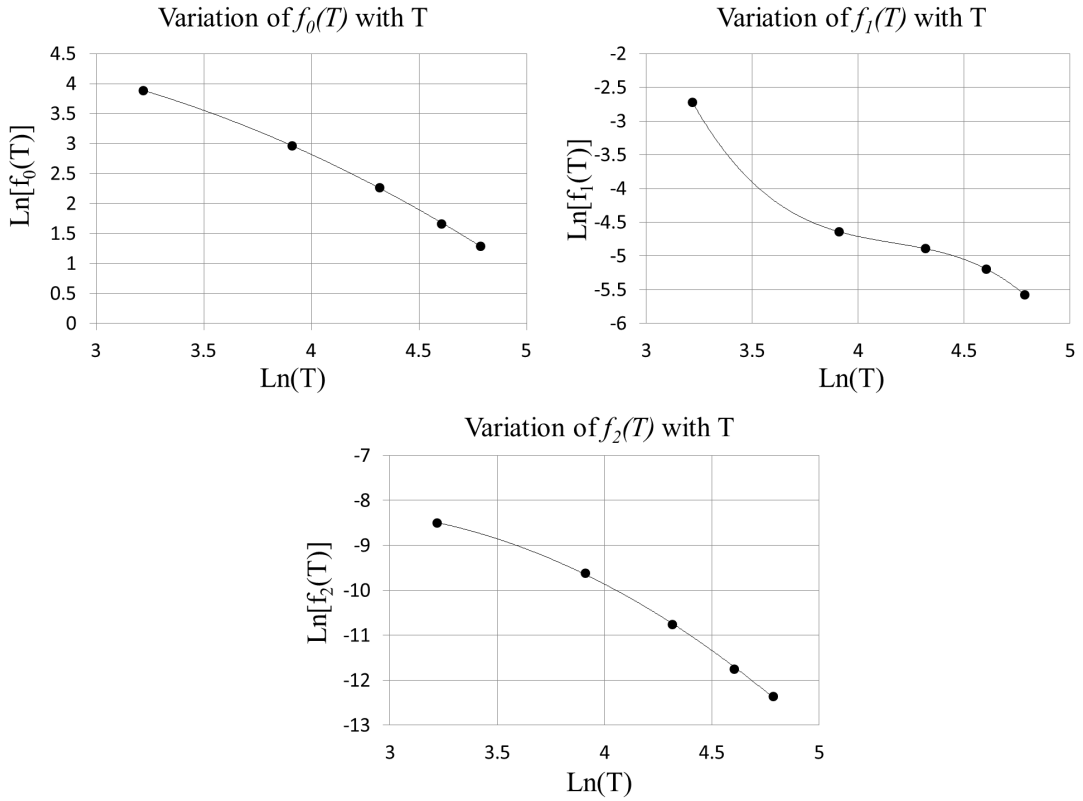

Fig. B.5. Variation of bulk modulus as a function of temperature for different constant pressures.

Equation B.8 can be rewritten thanks to the expressions in Eq. B.9.

$$\begin{aligned}\mu(p,T) = &\exp\left[-0.372\ln T^2 + 1.314\ln T + 3.504\right] + \\ &+(p-p_0)\exp\left[-1.867\ln T^3 + 23.333\ln T^2 - 97.48\ln T + 132.42\right] + \\ &+(p-p_0)^2\exp\left[-0.930\ln T^2 + 4.958\ln T - 14.818\right]\end{aligned} \tag{B.10}$$

The dynamic viscosity calculated with Eq. B.10 is going to be expressed in cP; the pressure has to be entered in bar and the temperature in °C. The error between the dynamic viscosity calculated with Eq. B.10 and the measured data is always lower than 13.5%, with an average error of 2.5% on the whole set of points. The developed mathematical model describes with high level of accuracy the variation of the dynamic viscosity over entire range of pressure and temperature spanned by the measurements.

LIST OF REFERENCES

LIST OF REFERENCES

P. Achten and M. Schellekens. Deformation effects on the load carrying capacity of the barrel bearing in axial piston pumps and motors. In *ASME International Mechanical Engineering Congress and Exposition*, pages 1–13, Chicago, Illinois, USA, 2006.

P. Achten and G. Vael. A Robust Hydrostatic Thrust Bearing for Hydrostatic Machines. In *7th International Fluid Power Conference*, pages 1–19, 2010.

J. Baker and M. Ivantysynova. ADVANCED SURFACE DESIGN FOR REDUCING POWER LOSSES IN AXIAL PISTON MACHINES. In *The 11th Scandinavian International Conference on Fluid Power, SICFP*, Linkoping, Sweden, 2009.

J. M. Bergada, D. L. Davies, S. Kumar, and J. Watton. The effect of oil pressure and temperature on barrel film thickness and barrel dynamics of an axial piston pump. *Meccanica*, 47(3):639–654, September 2011. ISSN 0025-6455. doi: 10.1007/s11012-011-9472-7.

J.M. Bergada, S. Kumar, D.Ll. Davies, and J. Watton. A complete analysis of axial piston pump leakage and output flow ripples. *Applied Mathematical Modelling*, 36 (4):1731–1751, April 2012. ISSN 0307904X. doi: 10.1016/j.apm.2011.09.016.

G. Chen. *Development of a thermal model for the rotating group in a swash plate type axial piston machine*. Master thesis, Purdue University, 2005.

M. B. Dobrica and M. Fillon. About the validity of Reynolds equation and inertia effects in textured sliders of infinite width. *Proceedings of the Institution of Mechanical Engineers, Part J: Journal of Engineering Tribology*, 223(1):69–78, January 2009. ISSN 1350-6501. doi: 10.1243/13506501JET433.

D. Downson and G.R. Higginson. A Numercial Solution to the Elastohydrodynamic Problem. *J. Mech. Eng. Sci*, 1(1):6–15, 1959.

D. Dowson. A generalized Reynolds equation for fluid-film lubrication. *International Journal of Mechanical Sciences*, 4(2):159–170, March 1962. ISSN 00207403. doi: 10.1016/S0020-7403(62)80038-1.

Ertel. Hydrodynamic Lubrication Based on New Principles. *Nature*, 190, 1939.

Y. Fang and M. Shirakashi. Mixed Lubrication Characteristics between the Piston and Cylinder in Hydraulic Piston Pump-Motor. *Trans. ASME, Journal of Tribology*, 177, 1995.

N. Franco. Pump design by force balance. *Hydraulics and Pneumatic*, 14(11):101–107, 1961.

M. Gockel. Inertia relief analysis using an automated support system. Technical report, MSC Software Support, 1999.

P. Goenka. Dynamically loaded journal bearings: finite element analysis. *Journal of Tribology (ASME)*, 106:429–439, 1984.

C.E. Goodyer. *Adaptive numerical methods for elastohydrodynamic lubrication*. Phd thesis, University of Leeds, Leeds UK., 2001.

H. Grandin. *Fundamentals of The Finite Element Method*. Macmillan Publishing Company, New York, 1986. ISBN 0-02-345480-6.

B. J. Hamrock, S. R. Schmid, and B. O. Jacobson. *Fundamental of Fluid Film Lubrication*. Marcel Dekken, Inc., New York, second edi edition, 2004. ISBN 0-8247-5371-2.

G. Hibbert, D. V. Lindsay, N. A. Shute, and D. E. Turnbull. The balancing of piston and valve plate forces in axial piston pumps and motors. Technical report, British Hydromechanics Research Association, 1971.

Y. Hong and S. Lee. A comparative study of CrXN (X=Zr, Si) coatings for the improvement of the low-speed torque efficiency of a hydraulic piston pump. *Metals and Materials International*, 14(1), 2008.

L.G Houpert and B.J. Hamrock. Fast Approach for Calculating Film Thicknesses and Pressures in Elastohydrodynamically Lubricated Conjunctions. *Journal of Tribology*, 108(3):411–420, 1986.

C. Huang and M. Ivantysynova. A new approach to predict the load carrying ability of the gap between valve plate and cylinder block. In *Bath Workshop on Power transmission and Motion Control PTMC*, pages 225–239, Bath, UK, 2003.

F. Incropera, D. DeWitt, T. Bergman, and A. Lavine. *Fundamentals of Heat and Mass Transfer*, volume 6th of *Dekker Mechanical Engineering*. John Wiley & Sons, 2007. ISBN 9780471457282.

J. Ivantysyn and M. Ivantysynova. *Hydrostatic Pumps and Motors*. Akademia Books International, New Delhi, India, 2001. ISBN ISBN-81-85522-16-2.

M. Ivantysynova and J. Baker. Power loss in the lubricating gap between cylinder block and. *International Journal of Fluid Power*, 10(2):29–43, 2009.

H. Jasak. *Error Analysis and Estimation for the Finite Volume Method with Applications to Fluid Flows*. PhD thesis, Imperial College of Science, Technology and Medicine, 1996.

N. Jouini and M. Ivantysynova. Valve plate surface temperature prediction in axial piston machines. In *5th FPNI PhD Symposium*, pages 95–110, 2008.

T. Kazama, T. Tsuruno, and H. Sasaki. Temperature Measurement of Tribological Parts in Swash-Plate Type Axial Piston Pumps. *VENTIL*, 2011(2):140–146, 2011.

J Kim and J.Y Jung. Measurement of fluid film thickness on the valve plate in oil hydraulic axial piston pumps (Part I - bearing pad effects). *KSME Int. Journal*, 17 (2):246–253, 2003.

J. Kim, H. Kim, and Y. Lee. Measurment of Fluid Film Thickness on The Valve Plate in Oil Hydraulic Axial Piston Pumps (Part II: Spherical Design Effects). *Journal of Mechamcal Science and Technology*, 19(2):655–663, 2005.

K. Kim and F. Sadeghi. Three-dimensional temperature distribution in EHD lubrication: Part II - point contact and numerical formulation. *ASME Journal of Tribology*, 115:36–45, 1992.

R. J. Klop. *Investigation of Hydraulic Transmission Noise Sources.* PhD thesis, Purdue University, 2010.

U. Küttler and W. Wall. Fixed-point fluidstructure interaction solvers with dynamic relaxation. *Computational Mechanics*, 43(1):61–72, February 2008. ISSN 0178-7675. doi: 10.1007/s00466-008-0255-5.

Berzins Lu, H., C.E. M., Goodyer, and P.K. Jimack. High order discontinuous Galerkin method for EHL line contact problems. *Communications in Numerical Methods in Engineering*, 21:643–650, 2005.

N. Manring. Tipping the Cylinder Block of an Axial-Piston Swash-Plate Type Hydrostatic Machine. *Transactions of the ASME*, 122(March):216–221, 2000.

K. Matsumoto and M. Ikeya. Leakage characteristics between the valve plate and cylinder for low speed conditions in a swashplate-type axial piston motor. *Transactions of the Japan Society of Mechanical Engineers*, 57:3008–3012, 1991a.

K. Matsumoto and M. Ikeya. Friction and leakage characteristics between the valve plate and cylinder for starting and low speed conditions in a swashplate type axial piston motor. *Transactions of the Japan Society of Mechanical Engineers*, 57:2023–2028, 1991b.

J. Murthy. Numerical Methods in Heat, Mass and Momentum Transfer. Technical report, School of Mechanical Engineering, Purdue University., West Lafayette, IN., 2002.

L. Olems. Investigations of the temperature behaviour of the piston cylinder assembly in axial piston pumps. *International Journal of Fluid Power*, 1(1):27–38, 2000.

S. Patankar. *Numerical Heat Transfer and Fluid Flow.* Taylor&Francis, 1980. ISBN 0-89116-522-3.

M. Pelosi. *An Investigation on the Fluid-Structure Interaction of Piston/Cylinder Interface.* Phd thesis, Purdue University, 2012.

M. J. D. Powell. *Numerical Methods for Nonlinear Programming Algebraic Equations.* Gordon and Beach Science, London, p. rabinow edition, 1970.

W. Press, S. Teukolsky, W. Vetterling, and B. Flannery. *Numerical Recipes 3rd Edition: The Art of Scientific Computing*, volume 1. Cambridge University Press, 2007. ISBN 0521880688.

O. Reynolds. On the Theory of Lubrication and its Application to Mr. Beauchamp Tower's Experiment, Including an Experimental determination of the Viscosity of Oilve Oil. *Phil. Trans. Roy. Soc.*, 177:457–234, 1886.

Y. Saad. *Iterative Methods for Sparse Linear Systems, Second Edition*. Society for Industrial and Applied Mathematics, 2003. ISBN 0898715342.

F. Sadeghi and T.A. Dow. Thermal Effects in Rolling/Sliding Contacts: Part 2-Analysis of Thermal Effects in Fluid Film. *ASME Journal of Tribology*, 109:512–518, 1987.

J. S. Sartchenko. Force balance condition of the Valve plate and rotor of an axial piston pump. *BHRA T 750*, 10, 1950.

J. B. Scarborough. *Numerical Mathematical Analysis, 4th edition.* Johns Hopkins Press, Baltimore., 1958.

A. Schenk. *Predicting lubricating performance between the slipper and swash plate in axial piston hydraulic machines*. PhD thesis, Purdue University, 2013.

G. Seeniraj. *Model Based Optimization of Axial Piston Machines Focusing on Noise and Efficiency*. PhD thesis, Purdue University, 2009.

J. R. Shewchuk. An Introduction to the Conjugate Gradient Method Without the Agonizing Pain. *Science*, 49(CS-94-125):64, 1994. ISSN 14708728. doi: 10.1.1.110.418.

N A Shute and D E. Turnbull. The hydrostatic pressure distribution across the lands of a valve plateof an axial piston machine, part I No Heat Loss. Technical report, British Hydromechanics Research Association, 1964.

A. Z. Szeri. *Fluid Film Lubrication*. Cambridge University Press, New York, second edi edition, 2011. ISBN 978-0-521-89823-2.

C. Taylor and J. F. O'Callaghan. A numerical solution of the elastohydrodynamic lubrication problem using finite elements. *Journal of Mechanical Science*, 14:229–237, 1972.

R Taylor and L Lin. The application of tribological principles to the design of the valve plate of an axial piston pump, part I. *The BFPR Journal*, 17(2):257–262, 1984.

B. R. Vatti. A generic solution to polygon clipping. *Communications of the ACM*, 35(7):56–63, 1992.

H. K. Versteeg and W. Malalasekera. *An introduction to computational fluid dynamics: the finite volume method*, volume M. Pearson Education, 2007. ISBN 9780131274983.

C. T. Wang. *Applied elasticity*. McGraw-Hill Book Company, New York, 1953.

U. Wieczorek and M. Ivantysynova. Computer aided optimization of bearing and sealing gaps in hydrostatic machines - The simulation tool CASPAR. *International Journal of Fluid Power*, 3(1):7–20, 2002.

H. Winter, F. Beckwith, W., Y. Sadler, L., E. Gratz, C., D. Lozowski, and F. Savinell, R. *American Institute of Chemical Engineers, Modular Instruction. Series C, vol 7: Calculation and Measurements Techniques for Momentum, Energy and Mass Transfer*. 1980. ISBN 0-8169-0415-4.

A. Yamaguchi. Formation of a Fluid Film between a Valve Plate and a Cylinder Block of Piston Pumps and Motors (1st report, A Valve Plate with Hydrodynamic Pads). *Bullettin of JSME*, 29(251):1494–1498, 1986.

A. Yamaguchi. Formation of a Fluid Film between a Valve plate and a Cylinder block of Piston Pumps and Motors (2nd report, A valve plate with Hydrostatic Pads). *JSME International Journal*, 30(259):87–92, 1987.

A. Yamaguchi, H. Sekine, S. Shimizu, and S. Ishida. Bearing/seal characteristics of the Oil film between a valve plate and a cylinder block of axial pumps.: : Effects of fluid types and theoretical discussion. *The Journal of Fluid Control*, 20(4):7–29, 1990.

M. Zecchi and M. Ivantysynova. Cylinder block/valve plate interface - A novel approach to predict thermal surface loads. In *8th IFK International Conference on Fluid Power*, pages 285–298, Dresden, Germany, 2012.

D. Zhu and S Wen. A Full Solution for the Thermalelastohydrodynamic Problem in Elliptical Contacts. *Journal of Tribology*, 106:246–254, 1984.

VITA

VITA

Marco was born in Guastalla, Italy. He received his B.Sc. and M.Sc. degrees in Mechanical Engineering at the University of Parma, Italy, with specialization in Energy conversion systems. After one year of fellowship at the University of Parma, working on modeling of external gears machines, Marco joined the Maha Fluid Power Research Center in May 2010 as PhD student, under the supervision of Dr. Monika Ivantysynova. Marcos main interests are in the numerical modeling of elasto-hydrodynamic and thermal effects in the main lubricating interfaces of positive displacement machines, with main focus of axial piston units. His research is partially founded by a NSF founded Engineering Research Center, the Center for Compact and Efficient Fluid Power (CCEFP), project 1B.1 and supported by a number of industry projects. Marco shared his research findings in eight international conferences on Fluid Power technology around the world during his almost four years at the Maha Center. Marco successfully defended is Ph.D. on November 21, 2013.